D0-electron correlations in pp collisions at $\sqrt{s} = 7$ TeV

Hege Austrheim Erdal

Dissertation for the degree of philosophiae doctor (PhD)
at the University of Bergen

March 24, 2014

Abstract

The ALICE experiment at the LHC is a dedicated heavy-ion experiment. It aims at improving the current knowledge of the Quark Gluon Plasma, a state of matter which is formed when the temperature and/or density of strongly interacting matter is high enough. The constituents of hadrons, quarks and gluons, are normally confined within the hadrons. In the Quark Gluon Plasma, the hadrons have been "melted down", the quarks and gluons exist in a deconfined state and can roam around more freely.

The partonic energy loss is a major topic in the study of the Quark Gluon Plasma, how the quarks and gluons will interact with the hot medium and as a result lose energy. This thesis focuses on heavy quarks like charm and bottom, and how they interact with the medium. Due to their high mass, these heavy quarks will be produced predominantly in the early stages of the collision and will subsequently experience the full evolution of the plasma.

Several studies exist on charged hadrons, mainly originating from lighter quarks, and the measurements have shown a suppression of these hadrons in collisions where the Quark Gluon Plasma is expected to be formed. The main source of energy loss for lighter quarks is radiative energy loss. If this is also the case for heavier quarks, such as bottom and charm quarks, the heavy quarks are expected to suffer a smaller suppression due to the so-called dead cone effect. However, recent results indicate a suppression of particles containing heavy quarks to be the same as that of charged hadrons, indicating that there are other factors contributing to the energy loss apart from radiative energy loss. Back-to-back correlation measurements of heavy-flavour mesons, or particles decaying from heavy-flavour mesons, can provide a crucial test to the nature of the energy loss. The aim of the measurements is to construct the correlated yield factor I_{AA}, and with this provide essential constraints to theoretical models.

This thesis presents the angular correlation measurements of D^0 mesons with electrons decaying from heavy-flavour mesons in proton-proton collisions. The main components of the analysis is to reconstruct D^0 mesons in ALICE via the hadronic decay channel $D^0 \rightarrow K\pi$, and to separate the electrons decaying from heavy-flavour

mesons from other electrons. The analysis provides a baseline for the analysis of Pb-Pb collisions. In order to provide more detailed information on the energy loss of heavy quarks, the analysis can also be used to separate out the contribution from b and c quarks, thus also giving vital information on the two quarks separately. The current results from the analysis will be presented, together with an estimate of the expected statistics and uncertainties after the upgrade of the ALICE detector, planned in 2018.

Acknowledgments

I am finally at the end of my PhD, nearly 10 years after I started at the University of Bergen as a fresh, and very naive, bachelor-student. Though it has been some wonderful years, I have to admit it has not been an easy ride. At times I thought I would never reach the final destination, but lucky for me, I have met a lot of fantastic people over the years at the University. Their motivation, and especially friendship, have always pushed and encouraged me to continue until I reached my goal.

All good things comes in three, and I have had the fortune of being supervised by no less than three supervisors for my PhD. These are Prof. Håvard Helstrup, Prof. Dieter Röhrich and associate professor Kristin Hetland, and I want to thank all of you for the invaluable help I have received over my PhD-years, both administrative and physics-wise. It has been very comforting to know that for every obstacle I run into, you are always there and willing to help.

In addition to having three supervisors, I have also been lucky enough to have, what I call, three mentors during my PhD. The first of them is Kalliopi Kanaki, thank you so much for introducing me into the wonderful world of nuclear physics and especially the High Level Trigger group. Thanks to Matthias Richter (aka Computer God) who have greatly improved my programming skills, at least I like to think so. Thanks for being so patient with me, both with my work for the HLT group, and also while writing the software for the analysis in my thesis. Thanks to Sedat Altinpinar (aka heavy-flavour God), it has been great having you as an oracle for every silly little physics question I have had over the last two years.

Thanks also to Per-Ivar Lønne, it has been great working with you these years, and also to Boris Wagner for all the help with Grid! Thanks to everyone else who have been connected, at some point or another, to the nuclear physics group while I have been a part of it, both in Bergen and in Oslo. You are too many to be mentioned by name, however I would especially like to thank Camilla Stokkevåg and Kristian Ytre-Hauge. Your friendship have meant the world to me throughout the last years! Thanks also to everyone I have worked with at the Bergen University College, especially Piotr Kaźmierczak (I hope I spelled that right), who I got to know

and adore while tutoring a course on Grid, and Petter Seip who I had the pleasure of working with while teaching a course in Labview. Thanks to the conveners of the heavy-flavour correlation working group at CERN, Elena Bruna and Andrea Rossi, who are always there to help and answer questions. Thanks also to the rest of the heavy-flavour correlation group, and also everyone I have worked together with in the HLT team. When I have had so many fantastic colleagues, it makes the struggling life of a PhD so much more easy!

I would also like to thank my physics girls Sabrina Eder, Sigrid Meyer and Beate Humberset, and especially my best friend Jenny Luneng! Our evenings with knitting (sorry Sabrina), and whatever else fun we can think off, have been fantastic to take my mind of work!

My family deserves also a huge thank you! I know that you sometime worry that I stress too much, travel too much and are visiting too little, but I am so grateful for all the support you have given me over the years!

Last, but definitely not least, I want to thank my overbearing, loving boyfriend Jan Christian Liby. Thank you for listening to all my frustrations about work. I know I can be a bit stressed from time to time, so thank you for always being and making me laugh when I am stressed.

Preface

This PhD-thesis is the result of a collaboration between the University of Bergen, Bergen University College and CERN. The work I have performed during my PhD-period, are divided into two separate parts. The first part, lasting roughly 2.5 years, was work performed for the High Level Trigger (HLT) group in ALICE. The HLT is a part of the ALICE trigger-scheme, and the main aim of the HLT is to reduce the data stream from the detectors, estimated to be 25 GB/s for central Pb-Pb collisions, down to the Data Acquisition storage bandwidth of 4 GB/s. This is realized through real-time event reconstruction of p-p and Pb-Pb collisions, and subsequently issuing a trigger decision based on the physics content of each event. More information on the HLT system can be found in chapter 3 of this thesis.

My work in the HLT group has focused on monitoring the data quality from the on-line event reconstruction. I entered the group in autumn/winter of 2009, right after the LHC started colliding protons. The work naturally progressed from first comparing the reconstruction performed on-line and off-line, where the latter is the reconstruction used for physics analysis and is performed with access to the full calibration, to only investigating the stability of the on-line tracking over time when the on-line tracking had been fully commissioned and transferred to stable production mode. Later, the quality assessment was also transferred to an on-line mode, meaning that information from the reconstructed events is displayed in real-time, including both histograms displaying key event distributions, like the distributions of the reconstructed vertex and TPC cluster points per track, and also an event display.

The second part of my PhD-period was connected to work performed with the Heavy-Flavour Correlation and Jets (HFCJ) working group in ALICE, and I was involved with this work for the last 2 years of my PhD. There was a little overlap of roughly half a year with my work for HLT. The work I performed in this working group forms the foundation of my PhD thesis, and has been focused on the azimuthal angular correlation of D^0 mesons with heavy-flavour electrons. The main part of my work has involved writing the software for the analysis, and the selection of heavy-flavour electrons, mainly for p-p collisions. The software for the selection of

D^0 mesons and heavy-flavour electrons was already in place in our software package AliRoot, and as a result this did not have to be written specifically for our analysis. Thus, the main work for the setup of the analysis software was to implement it in our code, and to do necessary modifications to the selection of heavy-flavour electrons. For the selection of the D^0 mesons, the software has been written by the Dmeson to Hadron Working Group (PWG-D2H), while for the selection of heavy-flavour electrons, we have implemented parts of the software written by the Heavy-Flavour Electron working group (PWG-HFE). I have not been working alone on the analysis, I have had the pleasure of working with Matthias Richter, Sedat Altinpinar and Per-Ivar Lønne.

Contents

List of Tables

List of Figures

Chapter 1

Introduction

The Big Bang theory is the prevailing theory of how the Universe started and subsequently evolved. The theory states that around 13.8 M years ago, all matter in the Universe was constricted to a singular point. In the following evolution of the Universe, a few μs after the Big Bang, there is also strong indication that the Universe was in the form of a Quark Gluon Plasma (QGP). This is a state of matter where the temperature is high enough so its constituents are quarks and gluons.

Today, high-speed accelerators are utilized to recreate the conditions similar to those very early in the Universe by colliding heavy ions. In these collisions, the hundreds of protons and neutrons inside the ions are smashed into each other at high energies. This collision produces dense, hot fireballs, where everything "melts" into a QGP. The fireball instantly cools down, and the individual quarks and gluons recombine into a blizzard of hadrons that is sent out in all directions. By investigating the outgoing particles, their distributions and energies, one can learn more about the properties of the plasma itself. The Large Hadron Collider (LHC) at CERN is an example of such an accelerator. At temperatures of 5.5 trillion degrees Celsius, the QGP created in heavy-ion collisions at the LHC is the hottest thing ever created on Earth [1], and it is 100.000 times hotter than the center of the Sun.

1.1 Quark Gluon Plasma

The deeper one goes into the structures of matter, the smaller the constituents become. Atoms consists of a nucleus and one or more surrounding electrons, and the nucleus contains nucleons, or hadrons. The hadrons are further built up by quarks and gluons, and these quarks and gluons behave very differently from the heavier hadrons. Under ordinary conditions the quarks and gluons are confined inside hadrons, see section 1.1.2, and this makes it difficult to study their behavior.

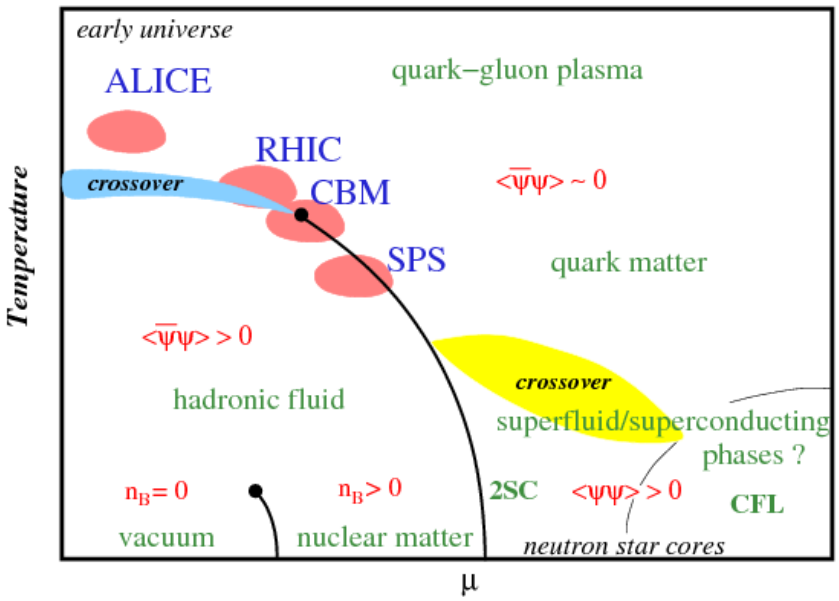

Figure 1.1: Phase diagram of nuclear matter. It shows the chemical potential, μ, versus temperature, and also illustrates different experiments and their exploration regions [3]. By increasing the temperature and/or baryo-chemical potential, the Quark Gluon Plasma is formed.

However, it has been predicted for a long time that if the temperature and/or density of matter becomes high enough, the strongly interacting quarks and gluons become free of their hadron host, and a deconfined phase of matter is created, namely the QGP [2].

Strongly interacting matter is expected to exist in different states, and the behavior can change for different conditions of temperature T and baryonic chemical potential μ. The baryo-chemical potential is defined as the energy E needed to increase the total number of baryons and anti-baryons, such as a proton or an anti-proton, with one unit. Figure 1.1 shows an illustration of the different states nuclear matter could exist in. Ordinary matter exists at relatively low temperatures and for $\mu \simeq m_p \simeq 940$ MeV. By increasing the baryo-chemical potential or the temperature a little, one can produce a hadron gas in which the nucleons interact and form pions and excited states of various hadrons. By further increasing μ or T, the deconfined QGP phase is created. The density of partons inside the hadrons becomes so high that the confinement of the quarks vanish. The figure also illustrates the exploration regions in the phase diagram of various experiments.

The first signs of a phase transition to the QGP became apparent using the Super Proton Synchrotron (SPS) in the 1990s. Later, the first evidence of this new state of matter came to light using the Relativistic Heavy Ion Collider (RHIC). The

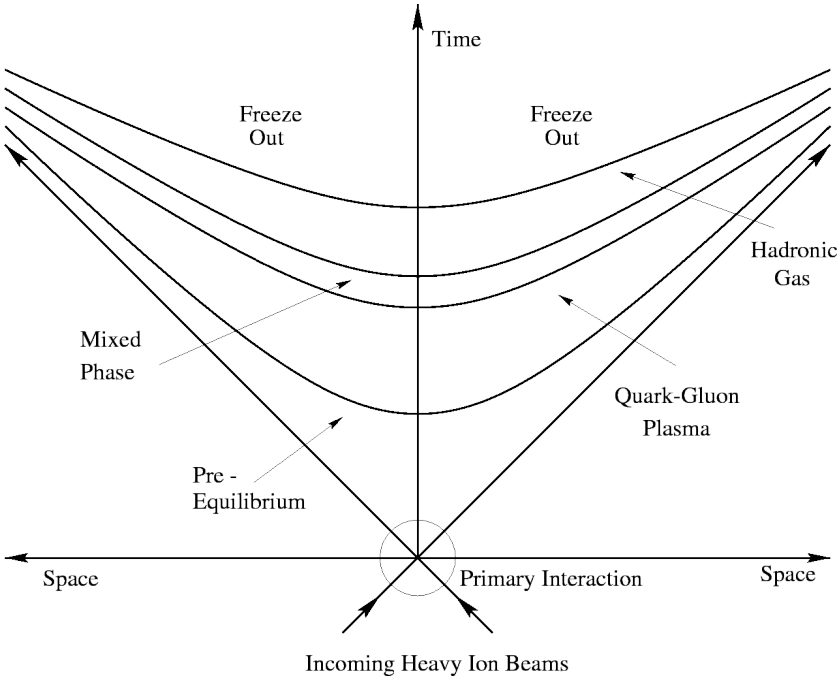

Figure 1.2: The space-time evolution of a heavy-ion collision [8].

first results from the LHC are consistent with the findings at both RHIC and SPS. One of the surprising discoveries achieved by RHIC of the new, hot medium is that it is a nearly friction-less liquid, not the gas one was expecting [4–7].

1.1.1 Evolution of the QGP

As mentioned previously, the QGP can be created in the laboratory by accelerating heavy ions up to very high energies and subsequently colliding them. At RHIC, gold ions with a center-of-mass energy, $\sqrt{s_{NN}}$, of 200 GeV are collided, while the LHC currently accelerates lead ions with $\sqrt{s_{NN}} = 2.76$ TeV, with a prospect of reaching 5.4 TeV after upgrading the accelerator[1]. The LHC energies allow for a longer-lived and hotter plasma, thus giving the possibility of studying the new state of matter in greater detail.

Figure 1.2 shows the space-time evolution of a heavy-ion collision, as described by the Bjorken Model [9]. The y-axis represent the time direction, with negative and positive values represent time before and after the collision, respectively. The x-axis represent the spatial direction. The colliding nuclei are Lorentz contracted and appear initially as two thin disks, and will collide at (0,0). During the pre-

[1] At the time of writing, the accelerator have been shut down for an upgrade, and should be in operation again in spring 2015.

equilibrium time, lasting around 1 fm/c, both hard processes on the parton level and soft interactions between the nucleons in the nuclei take place. A large amount of energy will be deposited in a small region of space and for a short duration of time, leading to a large enough energy density to form a fireball, the Quark Gluon Plasma. The created fireball will soon start to expand and cool down, the lifetime of the QGP are expected to be > 10 fm/c for LHC energies. Once the temperature reaches the critical temperature of the phase transition, the quarks will hadronize and form a hadron gas. The still interacting system keeps expanding until the temperature is low enough to reach the "freeze-out". The interactions terminate, and the surviving particles can be detected.

1.1.2 Quantum ChromoDynamics

Quantum ChromoDynamics (QCD) is the underlying theory of the strong force. QCD is a part of the Standard Model theory, which is a gauge theory describing sub-atomic interactions and processes. In addition to describing the strong force, the Standard Model also deals with the Electromagnetic and the Weak interaction.

The fundamental degrees of freedom in QCD are the gluon and the quark, where the gluon is the force carrier of the strong force. The name of the theory refers to the color charge characterizing the fundamental particles of the strong interaction. With six quark flavors and three colors, one can build all known hadrons, where mesons consists of one quark and one anti-quark, and baryons contain three quarks. While quarks (and gluons) carry color, the composition of the quarks make the hadrons color neutral.

The coupling constant characterizes the strength of the interaction. In the theory of the electromagnetic interaction, Quantum Electro Dynamics (QED), the coupling constant is small, $\alpha = e^2/\hbar c$. The coupling constant in QCD, on the other hand, is not constant, and can be in the order of one. The reason for this is one of the key features in QCD, namely the self-coupling of gluons. They arise because the gluons themselves have a non-zero color charge, and this is in contrast to QED where the photons, the force carrier of the electromagnetic interaction, have no electric charge and do not self-interact. As a consequence of the self-interacting gluon, the coupling constant increases with decreasing momentum transfer Q^2 [10, 11]:

$$\alpha_S(Q^2) \propto \frac{1}{ln(\frac{Q^2}{\Lambda^2})}, \tag{1.1}$$

where Λ is a constant defining the scale. The evolution of the QCD coupling constant as a function of Q^2 can also be seen in figure 1.3, which is a summary of different measurements of the coupling constant [12].

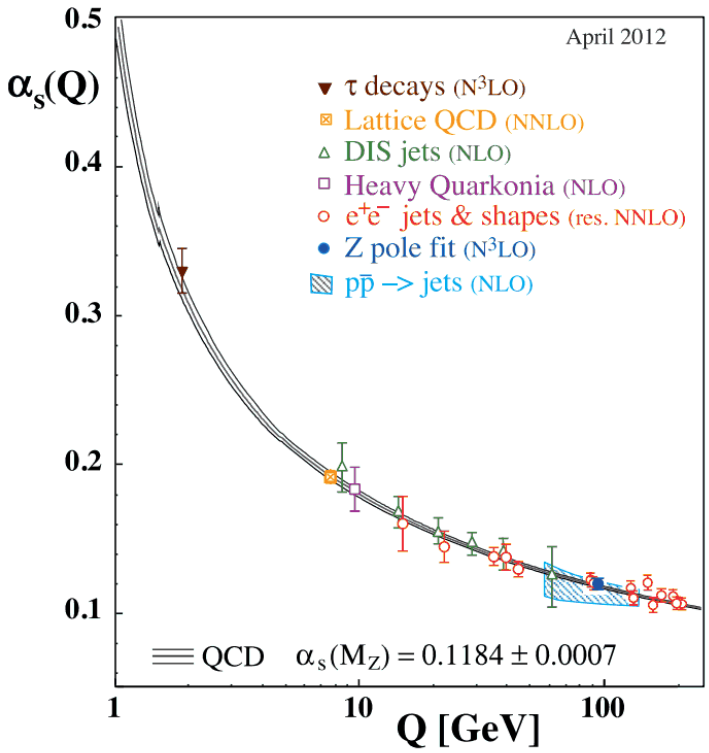

Figure 1.3: Summary of measurements of the QCD coupling constant. The respective degree of QCD perturbation theory in the extraction of α_S is indicated in brackets [12].

The difference of the coupling constant in QCD and QED makes it more challenging to perform dynamical calculations in QCD than for QED. Small momentum transfers give a coupling constant in the order of one, which makes it difficult to describe a collision in terms of Feynman diagrams, all contributions scale to one. In this regime, non-perturbative corrections become important, and it is necessary to use a different approach. Lattice QCD gives a way to solve the theory exactly from first principle using numerical calculations. It is a formulation of QCD where the quark fields are defined on lattice sites, while gluon fields are defined on the links between the lattice sites. This allows for numerical solutions of QCD, and have among other been used to predict a temperature for the transition into a QGP state of around 170 MeV, corresponding to an energy density of 1 GeV/fm^3 [13].

For high values of Q^2 the coupling constant is sufficiently small, $\alpha_S(Q^2 \to \infty) \to 0$, to enter the perturbative region, described through perturbative QCD.

Two important aspects of the QCD theory are *confinement* and *asymptotic freedom*. They can be understood by looking at the QCD potential between quarks

and anti-quarks:

$$V(r) = -\frac{\alpha}{r} + \sigma r. \tag{1.2}$$

With increasing mutual distance, r, between quark and anti-quark, the attractive force increases, the coupling between the two quarks become larger. As a consequence, if the quarks in a given hadron are pulled away from each other, at some point it becomes energetically favorable to create a new quark-antiquark pair from the vacuum, which combines with other quark/anti-quarks and forms new hadrons. This is referred to as confinement, the quarks can not be observed outside hadrons unless it is in a form of a QGP.

On the other hand, the strong interaction weakens with decreasing distances between quarks, also known as asymptotic freedom. It was argued, even before QCD was accepted as the fundamental theory of the strong interaction, that there should be a limit to hadronic matter above which there is a new phase of strongly interacting matter, the QGP. The transition to the QGP happens if the densities and/or temperature of hadronic matter become high enough, and here the quarks and gluons will interact as individual particles. This prediction of QCD was first formulated in the early 1970s by David Gross, Frank Wilczek and David Politzer [11, 14], which also awarded them a Nobel Prize in 2004.

1.2 Signatures of QGP and experimental results from the LHC

This section will focus on the first results from the LHC and compare these results to similar measurements performed at RHIC.

1.2.1 Elliptic flow

A topic which has received a lot of attention in heavy-ion collisions, is the measurement of anisotropic flow. The main interest in this topic stems from the fact that the anisotropic flow is sensitive to the medium properties at an early stage in its evolution. A heavy ion collision is characterized by its centrality, and one distinguishes between central and non-central collisions. The centrality is linked to the impact parameter of the collision, defined as the distance between the centers of the two colliding nuclei. In central collisions the colliding nuclei more or less overlaps, thus the impact parameter is close to zero. Non-central collisions have a smaller overlap region between the two nuclei and these collisions have larger impact parameter. An example of a non-central collision is illustrated in figure 1.4, where it

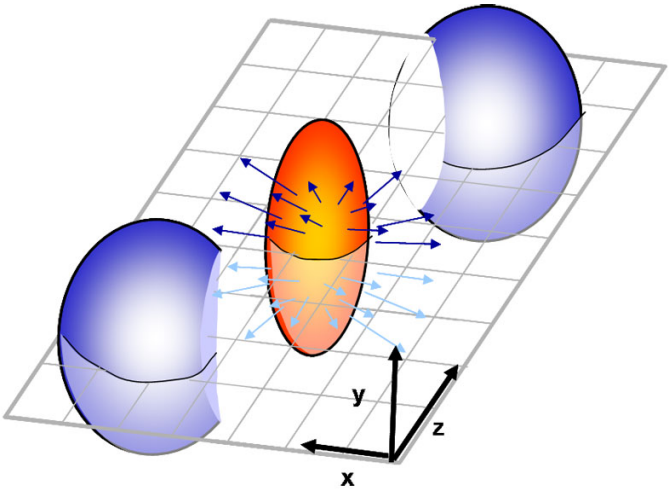

Figure 1.4: Schematic view of the interaction region between two incoming nuclei in a non-central collision. The interaction volume is seen to be almond-shaped in these collisions, and the reaction plane, defined as the plane spanned by x and z direction, is also included here. The coordinate system of the event has the x axis oriented in the direction of the impact parameter and the z axis along the beam direction, while the y axis is pointing out of the reaction plane [15].

can be seen that the overlap region between the two nuclei will be almond-shaped. The picture also shows the reaction plane, defined by the beam direction and the direction of the impact parameter.

The spatial asymmetry of the interaction region in non-central collisions is converted via multiple collisions into an anisotropic momentum distribution of the observed particles. As the spatial asymmetries rapidly decrease with time, anisotropic flow can develop only in the first fm/c [17]. The formation time of the plasma is in the order of 1 fm/c, and as a result, the flow will be sensitive to the properties of the created plasma. The anisotropic momentum distribution of particles can be expanded into a Fourier series:

$$E\frac{d^3N}{d^3\mathrm{p}} = \frac{1}{2\pi}\frac{d^2N}{\mathrm{p}_T d\mathrm{p}_T dy}\left(1 + \sum_{n=1}^{\infty} 2\mathrm{v}_n cos[n(\phi - \Psi_R)]\right). \tag{1.3}$$

N is the number of particles, E is the energy of the particle, p is the momentum, p_T is the transverse momentum, ϕ the azimuthal angle, y the rapidity and Ψ_R the reaction plane angle. The second order harmonics, v_2, is referred to as *elliptic flow*, and is the dominant factor to the anisotropic flow.

Experiments at RHIC were the first to report on large elliptic flow in heavy-ion collisions and lead to the picture of a strongly coupled quark-gluon plasma, sQGP

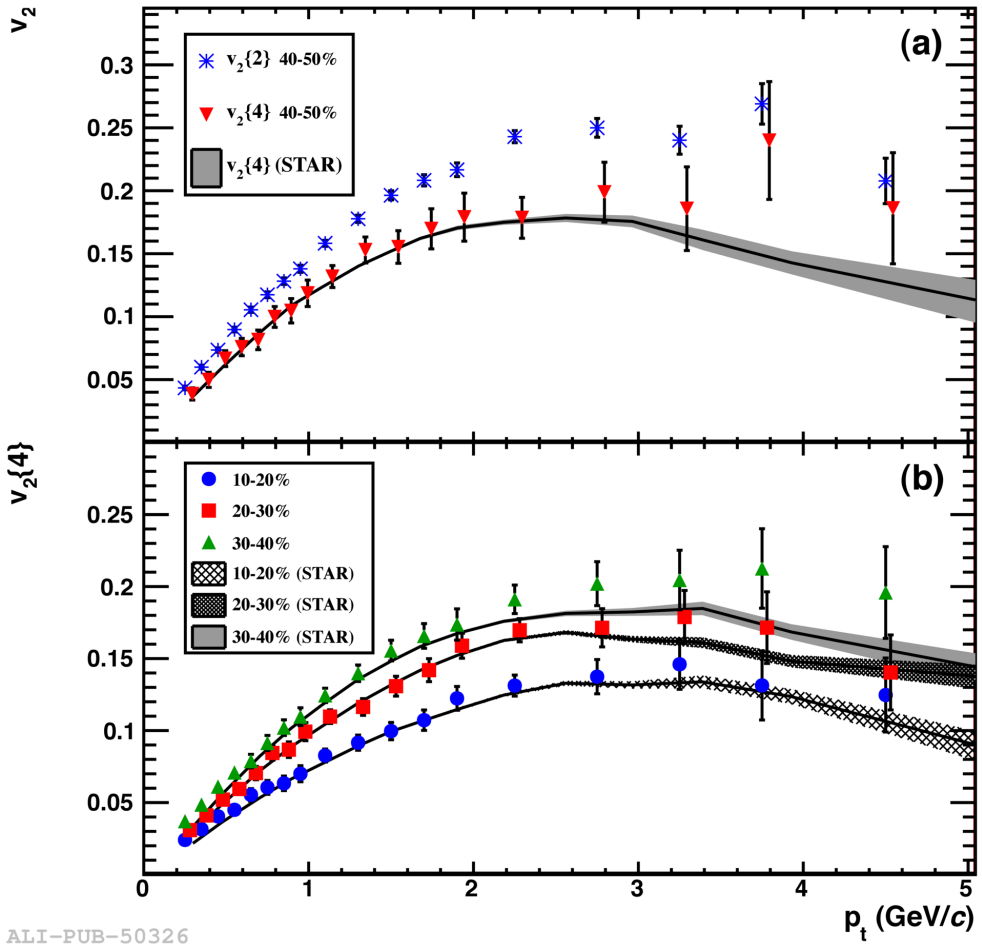

Figure 1.5: (a) Elliptic flow v_2 (p_T) for the centrality bin 40-50% for the 2- and 4-particle cumulant methods of measurements from ALICE (points) compared to the measurements from STAR at $\sqrt{s_{NN}}$ = 200 GeV (bands). (b) v_2 {4}(p_T) for different centralities compared to similar measurements from STAR [16].

[4–7]. The observed collective flow of the particles shows that the QGP behaves like a near-perfect liquid.

The elliptic flow has also been measured in Pb-Pb collisions at the LHC, and confirms the presence of a strong collective motion and a hydrodynamic behavior of the system [16]. Figure 1.5 shows the comparison of elliptic flow for different centralities as measured by ALICE and STAR at RHIC. The figure also compares various analysis techniques, the 2- and 4-particle cumulant method, denoted v_2 {2} and v_2 {4}. These techniques have different sensitivity to flow fluctuations and non-flow effects, which are uncorrelated to the initial geometry. It is observed that the p_T differential elliptic flow at low p_T is similar for the two experiments, consistent with predictions of hydro-dynamical models. The comparison of the integrated elliptic flow versus centrality and beam energy as measured by ALICE and STAR is shown in figure 1.6, and it is seen that there is a 30% increase when going from RHIC to LHC energies. The increase at the LHC is attributed to an increase in mean p_T of the particles.

The elliptic flow values measured by the experiments at RHIC and the LHC can be described by two main mechanisms. The constituents of the medium will interact with each other, causing a build-up of a collective expansion, first and foremost at low ($p_T < 3$ GeV/c) and intermediate (3-6 GeV/c) p_T. The second mechanism is dominant at large p_T, over 8 GeV/c, where the fragmentation of high-energy partons is expected to come into play. Partons traversing the dense medium will interact and lose energy, and this is strongly dependent on the distance the parton have to travel in the medium. It can be seen from figure 1.4 that partons traveling in the reaction plane will have a shorter path in the medium than partons traveling out of this plane, or along the y axis. Thus, the parton energy loss will depend on the emission angle of the parton, and as a result, there will be an azimuthal anisotropy in the particle production at high p_T [18]. For more details on partonic energy loss, see section 2.1.

1.2.2 The nuclear modification factor R_{AA}

Partons, or quarks and gluons, propagating through the produced, hot medium will interact with it and lose energy. In order to quantify this nuclear medium effect, the nuclear modification factor, R_{AA}, is extracted. It is defined as the ratio of the charged particle yield in heavy-ion collisions to the charged particle yield in proton-proton collisions, where the charged particle yield in proton-proton collisions is scaled by the number of binary collisions:

$$R_{AA}(p_T) = \frac{(1/N_{evt}^{AA})d^2N_{ch}^{AA}/d\eta dp_T}{< N_{coll} > (1/N_{evt}^{pp})d^2N_{ch}^{pp}/d\eta dp_T}, \tag{1.4}$$

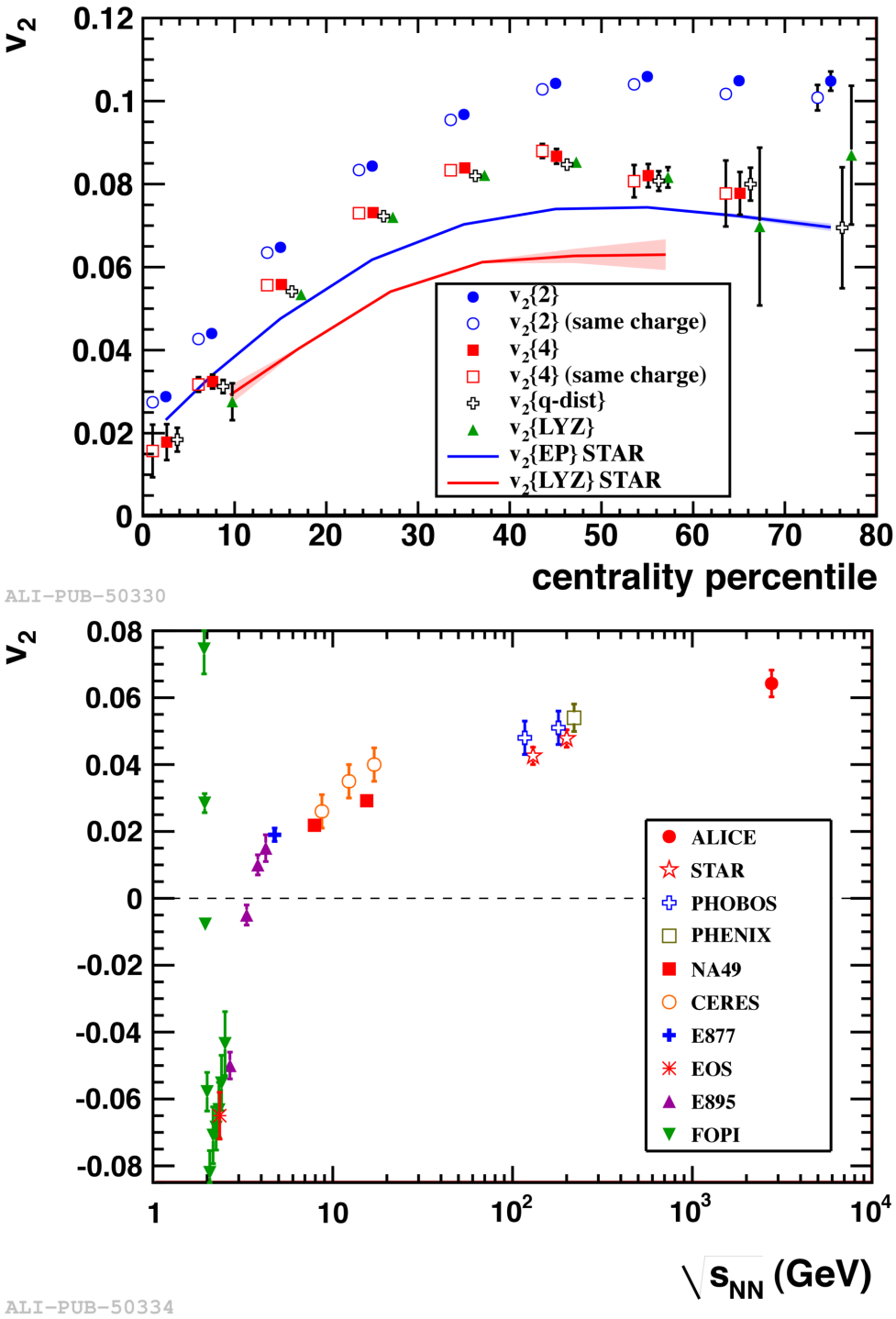

Figure 1.6: Top: Integrated elliptic flow versus centrality, for all charged particles (full markers) and same charge particles (open markers). The results from both the 2- and 4-particle cumulant method is shown, together with the results from RHIC for the event plane $v_2\{EP\}$ and Lee-Yang zeros represented by the solid curves. Bottom: Integrated elliptic flow versus beam energy for the 0-20% centrality class. The increase in integrated elliptic flow going from RHIC to LHC energies is attributed to the increase in mean p_T of the charged particle spectra [16].

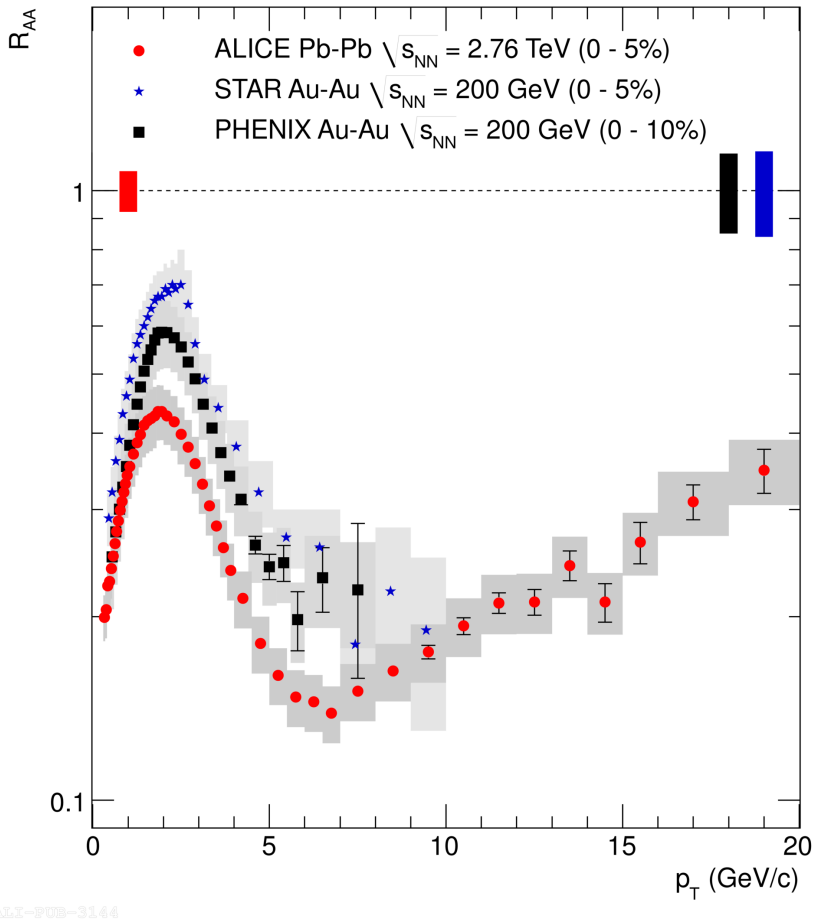

Figure 1.7: Comparison of the nuclear modification factor for charged particles as measured by the ALICE detector at the LHC and by the STAR and PHENIX detectors at RHIC. All measurements show a clear suppression of charged particles in heavy-ion collisions [19].

where η is the pseudo-rapidity, and $< N_{coll} >$ is given by the product of the inelastic NN cross section and the nuclear overlap function based on the Glauber Model [20]. The nuclear modification factor is equal to unity if the heavy-ion collisions were only a superposition of nucleon-nucleon collisions. If R_{AA} is smaller than one, this indicates suppression in the medium, whereas $R_{AA} > 1$ indicates enhancement.

Both the experiments at RHIC [4–7] and ALICE [19] have measured the charged particle R_{AA}, and figure 1.7 shows the nuclear modification factor for charged particles measured by ALICE compared to the one measured by STAR and PHENIX at RHIC. The measurements show clear signs of suppression, indicating that these two colliders produce a very dense medium when colliding heavy ions. The suppression is generally attributed to energy loss of the partons while traversing the produced Quark Gluon Plasma. It is observed that the position of the maximum at $p_T = 2$ GeV/c and the trend of a decreasing R_{AA} for higher p_T is similar for the different experiments. The R_{AA} reaches a minimum for hadrons with $p_T \sim$ 6-7 GeV/c, and it is also observed that this minimum is lower for LHC energies than for RHIC energies. This indicates a larger suppression, and an enhanced energy loss at LHC energies and thus a denser medium. For the measurements from ALICE, it is also observed that the R_{AA} is increasing again for $p_T > 7$ GeV/c. In order to get a more quantitative determination of energy loss and medium density, further investigations of gluon shadowing and saturation (and detailed modeling) is needed.

Figure 1.8 shows a comparison of the R_{AA} for central event (0-5% centrality) and more peripheral events (70-80% centrality), where the overlap region of the colliding heavy ions is much smaller. The R_{AA} is observed to be higher for peripheral events, and independent of p_T for $p_T > 2$ GeV/c. The measurements in these collisions resembles more what is observed in proton-proton collisions, indicating a smaller influence by the medium.

The R_{AA} of electro-weak particles, which do not interact strongly, has also been investigated at the LHC. Since these particles are not interacting strongly, thus not interacting with the QCD medium, the expectation is that there is no suppression of these particles, and this is also consistent with the measurements. Figure 1.9 shows the R_{AA} for electro-weak bosons (photons, Z and W particles) measured by the CMS[2] experiment at the LHC [22–24]. As a reference, the R_{AA} for charged particles and b-quarks are also included. The R_{AA} for the electro-weak probes are seen to be consistent with unity within the statistical uncertainties.

[2]Compact Muon Solenoid

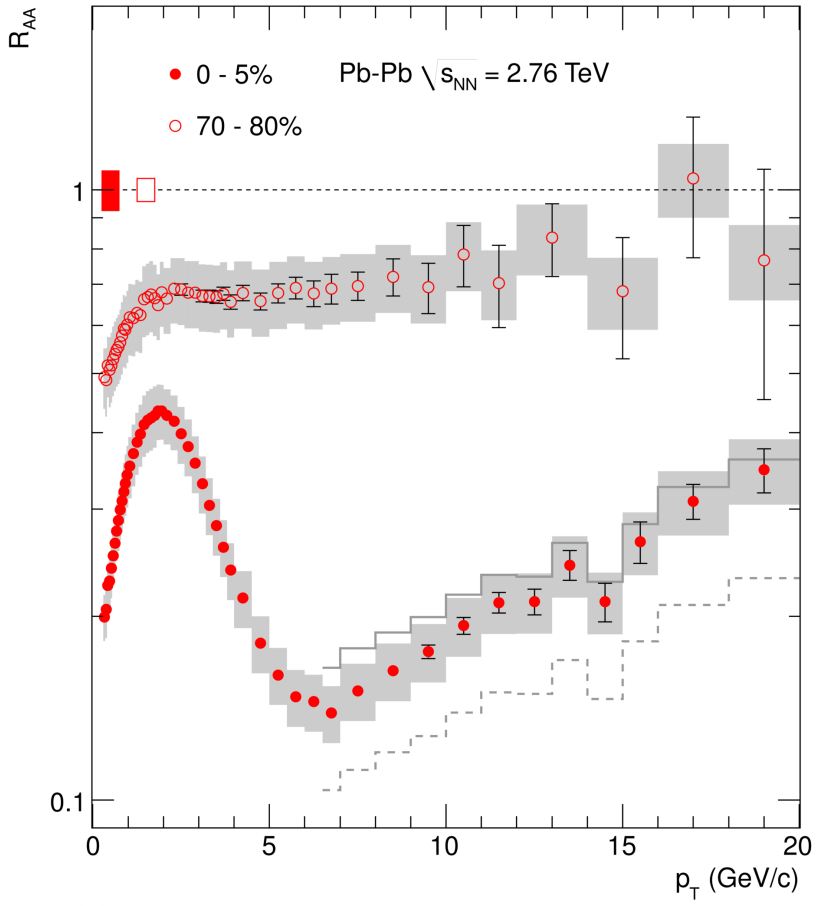

Figure 1.8: Nuclear modification factor for charged particles in ALICE. Central collisions (0-5% centrality) show a clear suppression, which is also much stronger than the suppression in peripheral collisions (70-80% centrality). For central collisions only, at $p_T > 6.5$ GeV/c, results for the R_{AA} are also shown by the use of an alternative p-p reference obtained by $p\bar{p}$ measurements at $\sqrt{s_{NN}}$= 1.96 TeV [21] in the interpolation procedure (solid line) and by applying Next-to-Leading-Order pQCD scaling to the p-p data at 0.9 TeV (dashed line) [19].

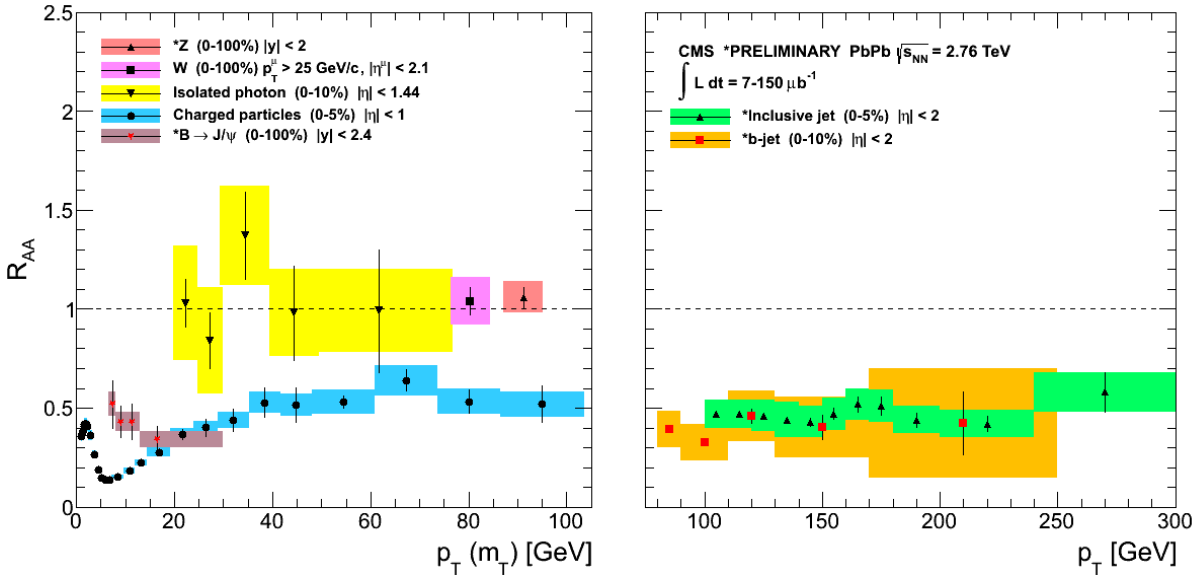

Figure 1.9: R_{AA} of the electro-weak bosons photons, Z and W as measured by CMS. The nuclear modification factor is close to 1, indicating that the electro-weak bosons traversing the produced, hot QCD medium will not interact with it, and thus experience no energy loss [22–25]. The R_{AA} for charged particles and b-quarks are shown for reference.

1.2.3 Jet modification and di-hadron correlation

Hard scattering processes (large momentum transfer Q^2) of the constituent partons of the colliding nucleons occur early in the collision. The outgoing partons will experience the full evolution of the created medium and because of this fact, they serve as good probes for the QGP. The partons will propagate through the medium and later fragment into hadrons, creating collimated showers of particles, or jets of particles, with high transverse momentum. Di-jets are one of the most common results of such a hard partonic scattering, emerging as two showers of hadrons emitted back-to-back in the azimuthal plane. As a result of the interaction of the partons with the QGP medium, it is expected that the fragmentation of particles is modified in central heavy-ion collisions compared to proton-proton collisions. Figure 1.10 shows an illustration of a back-to-back jet, where the recoiling parton are traversing the medium and interacting with it, effectively quenching the jet.

The modification of the fragmentation of high-p_T particles are studied through the reconstruction of jets, where particles are grouped inside a cone with a given angular radius. The experiments CMS and ATLAS at the LHC reconstruct di-jets on an event-by-event basis for leading jet transverse momentum above 100 GeV/c. They have reported on a strong di-jet asymmetry for the most central heavy-ion

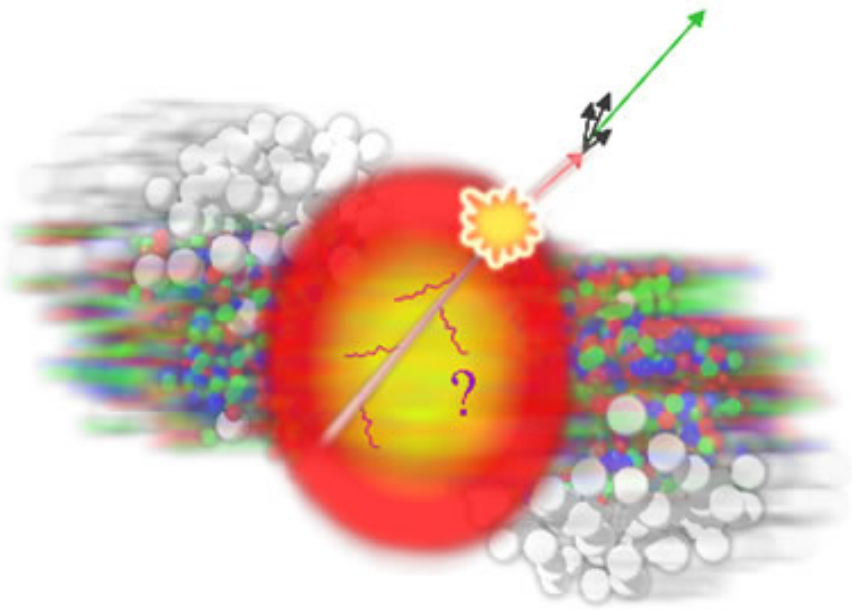

Figure 1.10: When quarks are produced back-to-back, one of them might be unable to escape the hot and dense Quark Gluon Plasma due to interactions with the QCD medium and subsequently loss of energy [26].

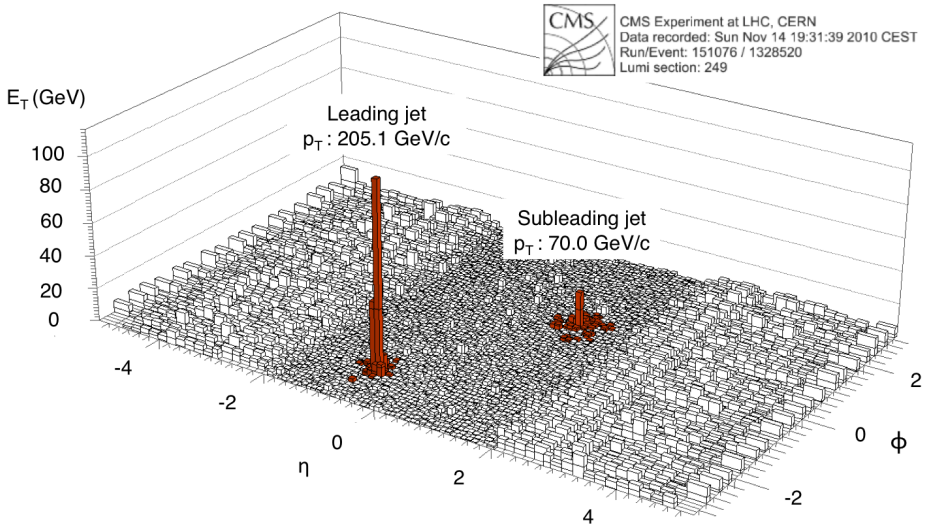

Figure 1.11: The quenching of jets as observed by the CMS experiment is clearly visible by inspecting an event which have been found to have a strong di-jet asymmetry. The leading jet is clearly visible, while the sub-leading jet is quenched [27].

collisions, and also that a large fraction of the quenched energy reappears as low- to intermediate-p_T particles at large radial distance from the jet [27, 28]. This is consistent with a high degree of jet quenching in the hot and dense QGP medium. Figure 1.11 shows an event with a strong di-jet asymmetry. It is clearly seen by investigating the event that the recoiling jet have been quenched.

Jets with a transverse momentum of less than 10-20 GeV/c are difficult to reconstruct as the background fluctuations due to the underlying event starts to dominate. As an alternative probe, one looks at the two-particle angular correlation. Angular correlations are typically studied using the two-dimensional $\Delta\phi$-$\Delta\eta$ correlation function, where $\Delta\phi$ is the difference in the azimuthal angle ϕ between the two particles, and $\Delta\eta$ is the difference in pseudorapidity η. The correlation function is plotted against the associated per trigger yield:

$$\frac{d^2N}{d\Delta\phi d\Delta\eta}(\Delta\phi, \Delta\eta) = \frac{1}{N_{trig}} \frac{d^N_{assoc}}{d\Delta\phi d\Delta\eta}. \tag{1.5}$$

It is common to project out the $\Delta\phi$ distribution from the correlation function above. This $\Delta\phi$ distribution have a characteristic near-side, $\Delta\phi$ =0, and an away-side, $\Delta\phi$ = π, as can be seen in figure 1.12. The figure compares the results of the per-trigger pair yield from ALICE as a function of $\Delta\phi$ for central Pb-Pb collisions (0-5% centrality, black line), peripheral Pb-Pb collisions (60-80% centrality, red points) and proton-proton collisions (blue points) [29]. It can be qualitatively observed that the central collisions exhibit a higher near-side peak, and that the away-side peak is suppressed in central Pb-Pb collisions compared to the peripheral collisions and proton-proton collisions.

To quantify both the enhancement of the near-side and suppression of the away-side, the I_{AA} and I_{CP} is computed. These are the ratio of the yields in heavy-ion collisions to proton-proton collisions and central to peripheral collisions, respectively. The I_{AA} gives information on both the energy loss, which is complementary to the measurement of R_{AA}, and it also probes the parton production spectrum. The near-side I_{AA} provides information on the fragmenting jet leaving the medium, while the away-side I_{AA} give information on the modification of the recoiling jet. The combined information of both I_{AA} and R_{AA}, and their sensitivity to different properties of the medium, will be particularly effective in constraining jet quenching models. The extracted I_{AA} and I_{CP} are shown in figure 1.13. The I_{AA} of the near- and away-side is computed both for central and peripheral Pb-Pb collisions, and while the I_{AA} for the central Pb-Pb collisions shows both the mentioned enhancement of the near-side and suppression of the away-side, the I_{AA} of the peripheral Pb-Pb collisions are closer to 1. The measurements of I_{CP} shows the same trend as that for the I_{AA} for central Pb-Pb collisions, illustrating that the peripheral col-

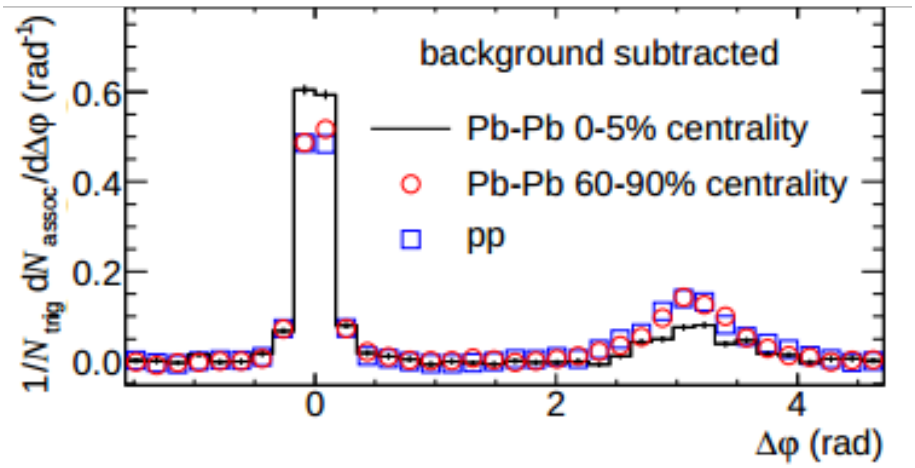

Figure 1.12: The per-trigger pair yield of di-hadron correlation for central Pb-Pb collisions (black curve), peripheral Pb-Pb collisions (red points) and proton-proton collisions (blue points) as measured by the ALICE experiment [29].

lisions behave more similar to proton-proton collisions. The enhancement of the near-side I_{AA} for central Pb-Pb collisions suggests that also the near-side parton is subject to medium modifications.

The STAR experiment at RHIC also reported on a suppression of the away-side I_{AA}, indicative of energy loss of the parton traversing the medium [30]. However, STAR did not observe the enhancement on the near-side.

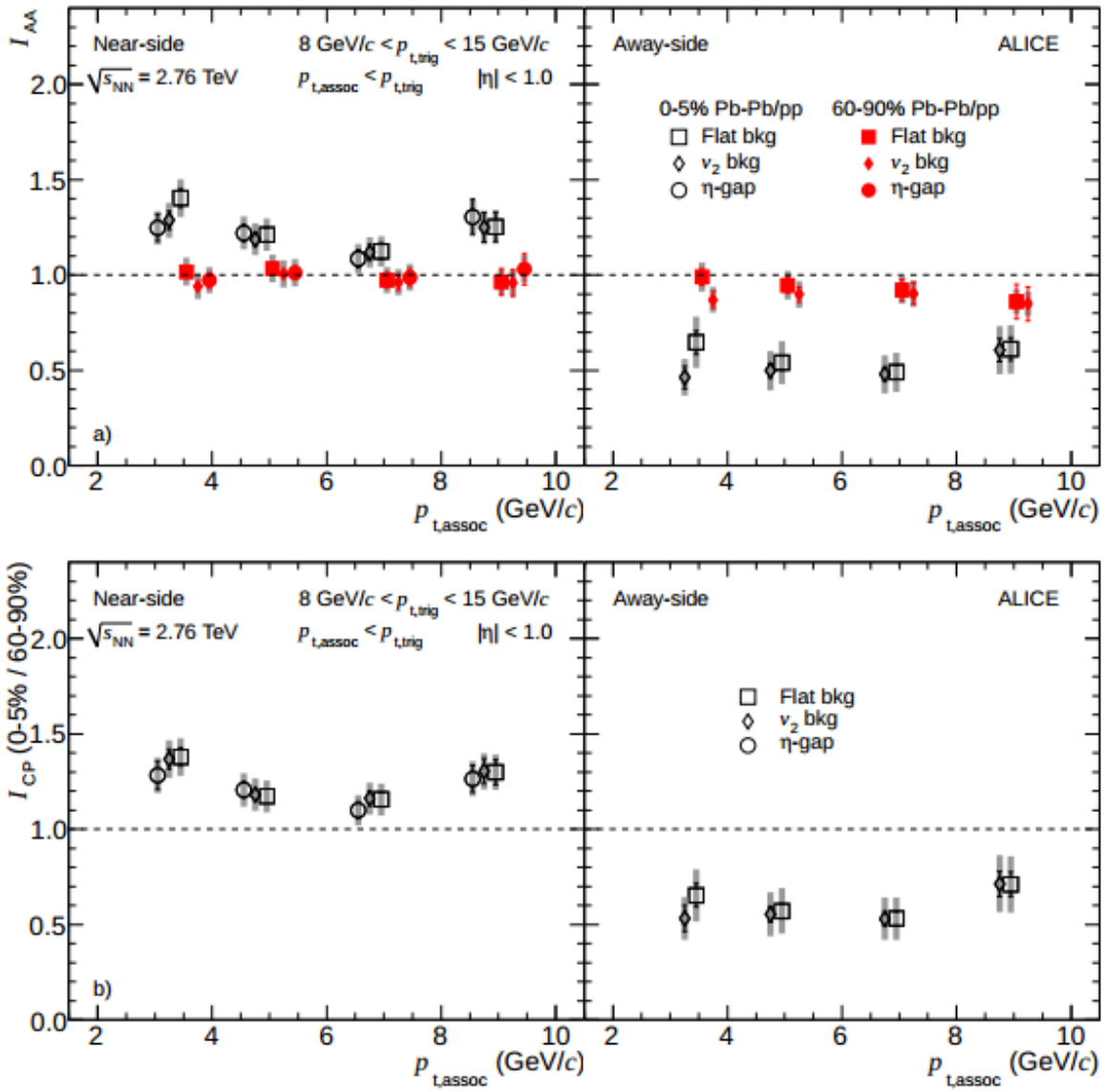

Figure 1.13: The I_{AA} for central (0-5% Pb-Pb/pp) and peripheral (60-90% Pb-Pb/pp) collision and I_{CP} for the near- and away-side of di-hadron correlation measurements as measured by the ALICE experiment. An enhancement of the near-side I_{AA} and I_{CP} is observed, while a suppression is observed in the away-side [29].

Chapter 2

Heavy-flavour quarks and correlations

Heavy-flavour quarks are quarks with a mass larger than the Λ_{QCD}-scale ($\approx$ 200 MeV), namely charm, bottom and top quarks[1]. Due to the relatively high mass of these quarks, they are primarily produced through hard scattering processes very early in the collision, $\tau \approx 1/(2m_Q) \lesssim 0.1$ fm/c (for charm). As the expected lifetime of the QGP at LHC energies is more than 10 fm/c, the heavy-flavour quarks will thus experience the full evolution of the medium. This makes the heavy quarks ideal probes for studying the strongly coupled QGP. Also, the high mass allows for a reliable calculation of the production cross section with perturbative QCD.

Heavy-flavour quarks are of special interest at the LHC experiments as the energies provided at the LHC, in comparison to earlier accelerators like RHIC, allows for a more detailed analysis. This will help increasing the knowledge of the production of heavy quark pairs and their interaction with the QGP. The expected charm and bottom production cross sections are about 10 and 100 times larger, respectively, at the top LHC energy compared to the top RHIC energy, based on next-to-leading order pQCD calculations [31]. This will extend the kinematic range to a much higher transverse momenta where charm and bottom production can be measured. An interesting topic is the comparison of the interaction of light and heavier quarks with the medium, which has been extensively studied both at RHIC and LHC. Some of the results from these measurements for both heavy-ion and nucleon-nucleon collisions are presented in this chapter. The measurements are also compared to theoretical predictions.

[1]When mentioning heavy-flavour quarks from now on, it refers to charm and bottom, as they are the main focus of this thesis.

2.1 Partonic energy loss

Partons traversing a QGP medium will lose energy, and in the most general case the total energy loss will be the sum of **collisional** and **radiative** energy loss. The energy loss will depend on the medium density, path length, the color charge and mass of the parton. The concepts of the different partonic energy loss types will be explained in the following section.

Radiative energy loss

Partons lose energy by radiating off gluons when experiencing inelastic scatterings while traversing the QGP medium. This form of energy loss is referred to as *radiative energy loss*, and it is predicted to be the main source of energy loss of a fast parton in a QCD environment. For a thick medium, i.e L >> λ, where L is the path length in the medium and λ the mean free path in the medium, the radiative energy loss can be approximated using the Landau-Pomeranchuk-Migdal (LPM) approximation [32]. In this approximation one differentiates between soft and hard gluon emission with respect to the characteristic gluonstrahlung energy $\omega_c = \frac{1}{2}\hat{q}L^2$. The radiated gluon spectrum, $\omega\frac{dI_{rad}}{d\omega}$, and corresponding average energy loss, ΔE_{rad}, is given by [33, 34]:

$$(\omega < \omega_c) \;\; \omega\frac{dI_{rad}}{d\omega} \approx \alpha_S\sqrt{\hat{q}L^2/\omega} \rightarrow \Delta E_{rad} \approx \alpha_S\hat{q}L^2, \tag{2.1}$$

$$(\omega > \omega_c) \;\; \omega\frac{dI_{rad}}{d\omega} \approx \alpha_S\hat{q}L^2/\omega \rightarrow \Delta E_{rad} \approx \alpha_S\hat{q}L^2 ln(E/(\hat{q}L^2)), \tag{2.2}$$

where ω is the energy of the radiated gluon, I is the intensity, α_S is the strong coupling constant and $\hat{q}$ is the transport coefficient of the medium. As seen in the equations, the QCD radiative energy loss shows a L^2 path length dependence.

Heavy quarks have a lower relativistic velocity β compared to light quarks, and thus heavy quark radiative energy loss has to be treated differently. As a consequence of low β, the radiation will be suppressed at angles inside a cone smaller than the ratio M/E, where M is the quark mass and E is the energy. This is also referred to as the dead cone effect [35, 36]. This leads to the modification [35]:

$$|\omega\frac{dI_{rad,Q}}{d\omega}|_Q = [1 + (\frac{M}{E})\sqrt{\frac{\omega^3}{\hat{q}}}]^{-2}\frac{2\alpha_S C_R}{\pi}\sqrt{\frac{\hat{q}L^2}{4\omega}} \tag{2.3}$$

C_R is the Casimir coupling factor = 4/3 (3) being the quark (gluon) color charge. As seen here, the mass of the heavier quarks are important for radiative energy loss,

and as a consequence, heavy quarks are expected to radiate off less gluons than the light ones, and thus lose less energy.

Collisional energy loss

Collisional energy loss happens through elastic scatterings with the constituents of the medium [37]. This form of energy loss has been considered to be less important for light quarks, but the recent results on heavy-flavour quenching have renewed the interest in this topic.

Color charge dependence

In addition to losing more energy due to the radiative energy loss, light-flavour hadrons are also expected to suffer a higher suppression than heavy-flavoured hadrons due to the *color charge dependence*. The probability for a gluon (quark) to radiate a gluon is proportional to the Casimir coupling factor = 3 (4/3), thus gluons will suffer a higher modification while traversing the medium than quarks [38]. The light-flavoured hadrons are more susceptible to be formed from gluon jets, and as a result they will be more suppressed than heavy-flavoured hadrons.

Energy loss for heavy versus light quarks

It has already been shown that charged hadrons coming primarily from lighter quarks have an R_{AA} much lower than 1, see section 1.2.2. This indicates that the partons traversing the produced QGP will interact with the medium and lose energy. For these lighter quarks, radiative energy loss is predicted to be the dominant source of energy loss. While comparing theoretical predictions with the measured R_{AA} as a function of the angle ϕ with respect to the reaction plane, and also using back-to-back di-hadron correlation measurements, the relative fraction of collisional energy loss to the overall energy loss for light quarks have been found to be approximately 10% [39, 40]. As a result of having the dominant contribution of energy loss from radiative energy loss, together with the color charge dependence, the light quarks are predicted to lose more energy than the heavy quarks, and gluons more than light quarks ($\Delta E_g > \Delta E_{light\,q} > \Delta E_{heavy\,q}$). However, results from RHIC, and now also LHC, shows a clear suppression comparable to the light hadrons also for heavy quark mesons and electrons decaying from heavy-flavour mesons as will be presented later in this chapter. Due to this reason, it is also important to distinguish the charm and bottom quarks to look at the effect individually, thus also getting a more hierarchical mass dependence of the heavy quarks.

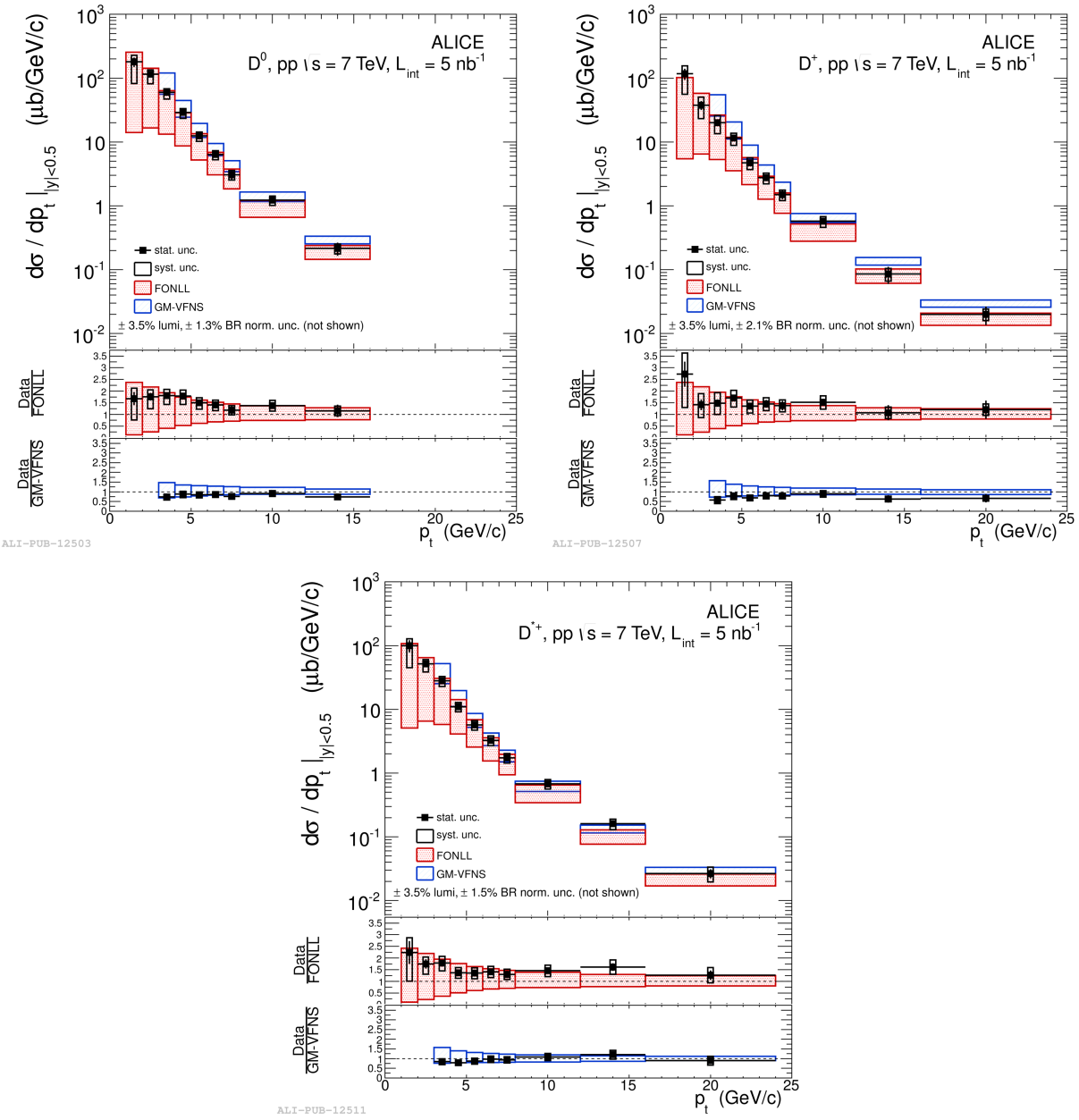

Figure 2.1: D meson production cross sections for D^0 (top left), D^+ (top right) and D^{*+} (bottom) as measured by the ALICE detector in proton-proton collisions at 7 TeV. The cross sections are compared to pQCD calculations, FONLL [41, 42] and GM-VFNS [43, 44], and they are in agreement within statistical and systematic uncertainties [45].

2.2 Results on heavy-flavour measurements at RHIC and LHC

2.2.1 Results from proton-proton collisions

Heavy-flavour measurements in ALICE are not only centered around heavy-ion collisions, but also proton-proton collisions. Results on the heavy-flavour production in proton-proton collisions will allow for a precise test for perturbative QCD in a previously unreached energy domain, since the high scale set by the quark mass should ensure that perturbative calculations are reliable. These measurements will also serve as a reference for measuring the modifications to heavy quark momentum distributions induced by interactions with the medium formed in heavy-ion collisions.

Heavy-flavour production has been studied, amongst other, at central rapidity via the reconstruction of D mesons through the hadronic decay channels. More details on the reconstruction of D^0 mesons can be found in section 4.1, for details on the reconstruction of the other D mesons, see [45]. The measured differential production cross section of D mesons is shown in figure 2.1. The cross sections are compared to Next-to-Leading Order (NLO) pQCD calculations, where FONLL (Fixed-Order-Next-to-Leading Log) [41, 42] describes reasonably well the differential cross section and GM-VFNS (General-Mass-Variable-Flavour-Number Scheme) [43, 44] describes prompt D meson measurements in the p_T range where the model is valid, namely $p_T > 3$ GeV/c.

The heavy-flavour production has also been studied by measuring electrons from semileptonic decays of charm and bottom hadrons, referred to in this thesis as heavy-flavour electrons (HFE). The heavy-flavour production cross section of heavy-flavour electrons as measured by the ALICE detector are compared to results from the ATLAS experiment [46, 47], see figure 2.2. The results illustrate the unique capability of ALICE to probe the production cross section down to very low electron p_T, and also shows the complementarity of ALICE and ATLAS at low and high p_T, respectively. The measurements are also compared to FONLL calculations and the measured cross sections are in agreement with the theoretical predictions within statistical uncertainties.

Using the impact parameter of the electron tracks, the HFE analysis can also be used to separate out the electrons mainly originating from bottom quarks [50]. B mesons, containing bottom quarks, have a longer mean lifetime than D mesons, thus the impact parameter of electrons originating from bottom quarks will be larger. Figure 2.3 shows the impact parameter distribution of electrons from different sources, where the mentioned feature is clearly seen. The electrons have been

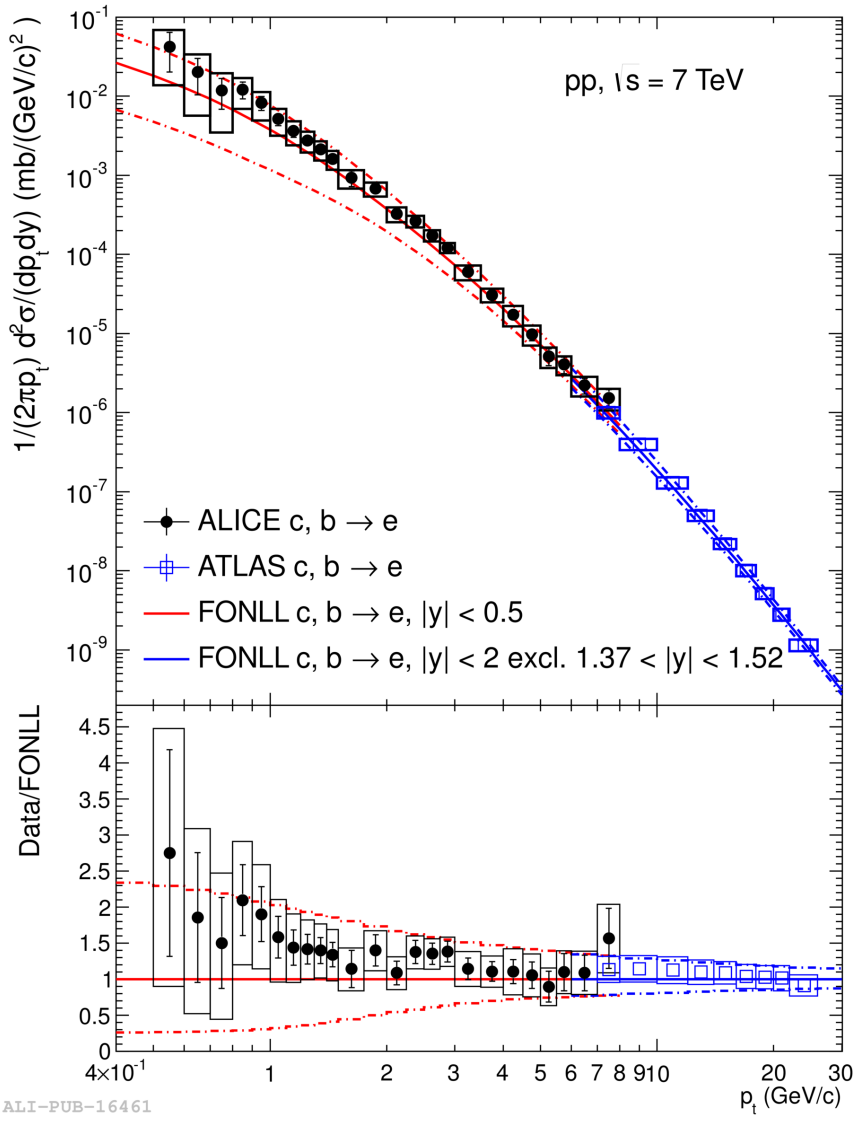

Figure 2.2: Comparison of the heavy flavour electron production cross section as measured by the ALICE detector [46] and the ATLAS detector [47] at higher electron p_T. The results are very complementary to each other and also show the ALICE detector's unique position to probe the production cross section down to low electron p_T.

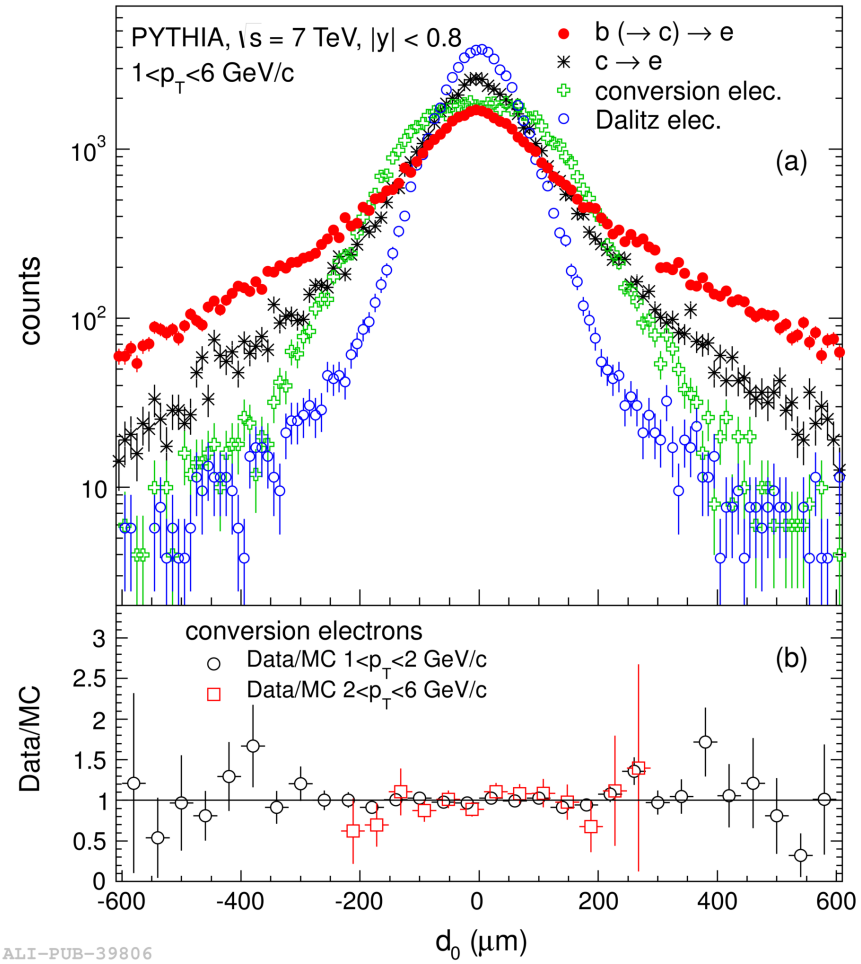

Figure 2.3: Impact parameter distributions of electrons from different sources, like charm and bottom hadrons, as well as light hadrons, like π^0, and electrons from conversion. The distribution is obtained from simulation of p-p collisions using the PYTHIA event generator [48], where the detector response is simulated with GEANT3 [49] in the electron p_T range $1 < p_T < 6$ GeV/c [50].

simulated in p-p collisions using the PYTHIA event generator[2], and then GEANT3 [49] is utilized to simulate the detector response.

Once the production cross section for electrons from bottom quarks has been calculated, it can be used to also extract the production cross section for electrons from charm quarks from the combined cross section. The extracted production cross section for both the charm and bottom contribution is shown in figure 2.4. By investigating the measured production cross sections for charm and bottom quarks, it can be observed that they are equal for transverse momenta around 3-4 GeV/c. The cross section is dominant for charm and bottom quarks for smaller and larger p_T, respectively. The production cross sections are again compared to pQCD calculations, FONLL, which are found to be in agreement within statistical and theoretical uncertainties.

2.2.2 R_{AA} of heavy-flavour mesons

The nuclear modification factor has been measured also for the heavy-flavour sector (see section 1.2.2 for more details on the charged hadron R_{AA}). Experimental results from both STAR and PHENIX at RHIC of the nuclear modification factor of non-photonic electrons, i.e electrons mainly decaying from heavy-flavour quarks, showed a suppression similar to that of charged hadrons [53, 54]. The observed suppression in these measurements was found to be larger than most expectations based on radiative energy loss. This suggested that radiative energy loss might not be enough to describe the observed attenuation.

ALICE has measured the suppression of D mesons coming from charmed hadrons. Figure 2.5 shows the measured D meson R_{AA} compared for different p_T ranges and centralities, and it can be seen that the D^0, D^+ and D^{*+} meson R_{AA} are compatible within uncertainties. The weighted average of the three D mesons R_{AA} in the centrality class 0-7.5% have been compared to the R_{AA} measured for pions and charged hadrons. The comparison can be seen in figure 2.6, indicating that the suppression of the various sources are compatible within uncertainties. There is however a hint of a difference in the lowest p_T region, below 5 GeV/c, and also for the mid-p_T region around 6-8 GeV/c, but more statistics is needed to extract the flavour dependence on the energy loss. The figure also shows the nuclear modification factor of non-prompt J/Ψ, which has decayed from B mesons, as measured by the CMS

[2]PYTHIA [48] is an event generator which is only exact at leading order, when only pair production processes are included. Higher order contributions are included in this generator in the parton shower approach [51]. It is not exact to next-to-leading order, but reproduces some aspects of the multi-parton-emission phenomenon. The simulations in this thesis uses the PYTHIA 6.4.21 event generator with the Perugia 0-parameter tuning [52]

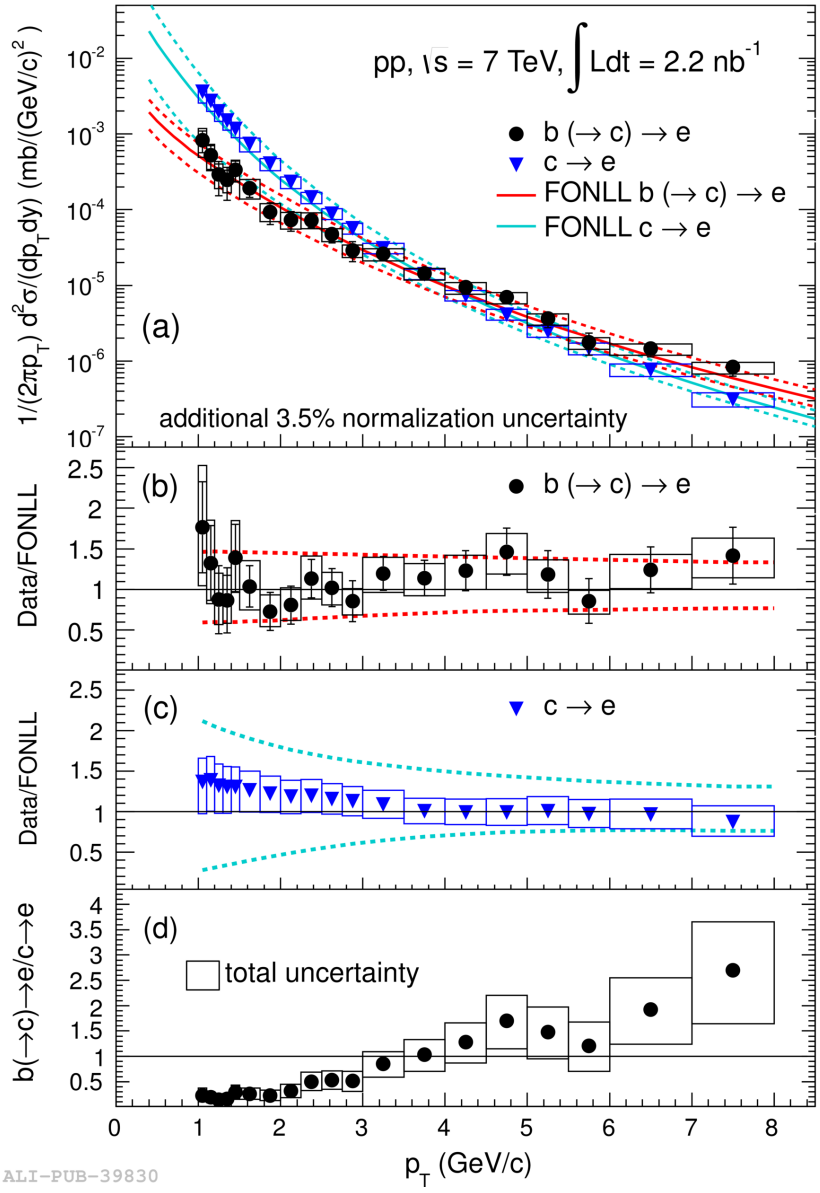

Figure 2.4: Differential cross section for electrons coming from charm (blue points) and bottom (black point) [50]. The cross sections are compared to pQCD calculations and they are in agreement within statistical uncertainties.

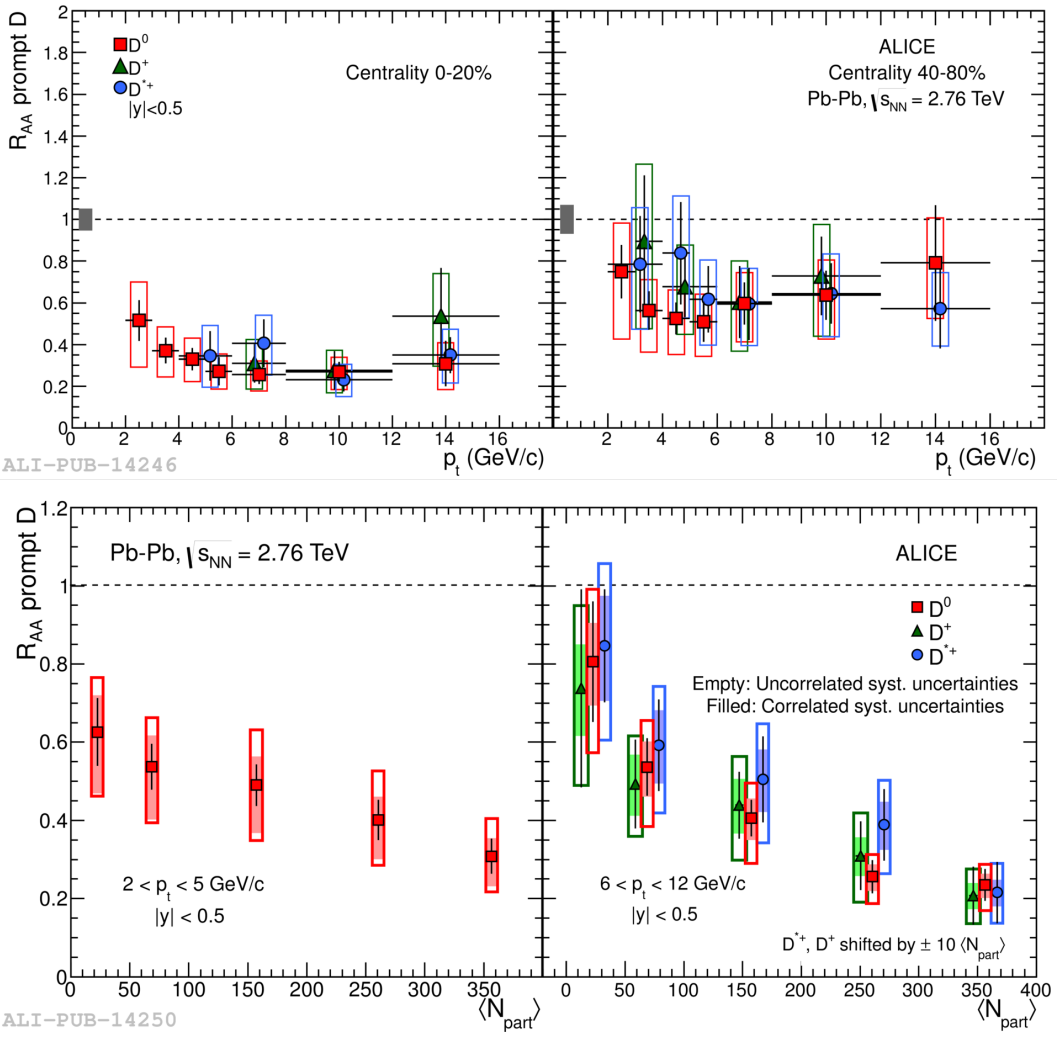

Figure 2.5: The nuclear modification factor, R_{AA}, of D-mesons as measured by the ALICE collaboration. Top plots: Comparison of different D meson R_{AA} versus p_T for central (left) and non-central (right) collisions. Bottom plots: Comparison of different D meson R_{AA} versus centrality for low D meson p_T (left) and higher D meson p_T (right) [55]. For the lowest p_T region, 2-5 GeV/c, only results for the D^0 meson are presented.

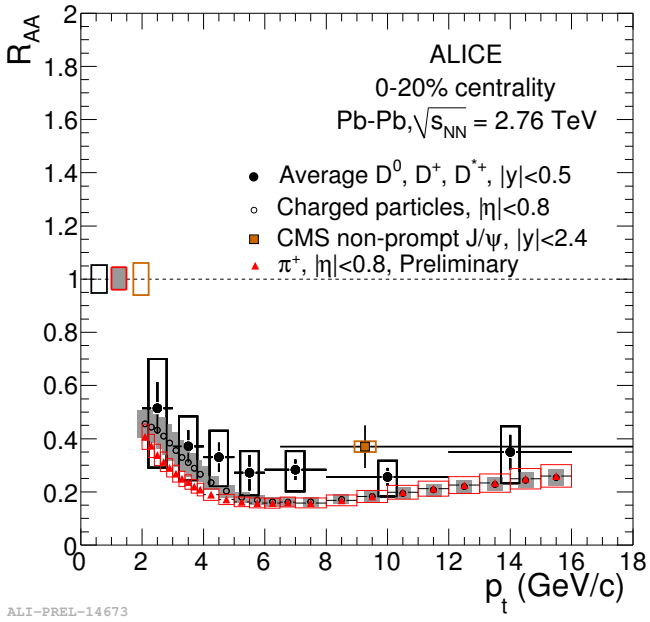

Figure 2.6: Comparison of the average nuclear modification factor of D mesons (D^0, D^+ and D^{*+}) in the 0-7.5% centrality class (black points), pions (red triangles) and charged hadrons (open black circles) in the 0-10% centrality class as measured by the ALICE experiment. These measurements are compared to the measurement of non-prompt J/Ψ R_{AA} as measured by the CMS experiment. It can be seen that there is a similar suppression of D mesons as for light hadrons. In addition, the R_{AA} for non-prompt J/Ψ can be seen to be comparable to that of D mesons, though it should be stressed that the kinematical regions for the analyses is different. More statistics is at this point needed to extract flavour dependence of energy loss [55, 56].

experiment at the LHC with $p_T > 6.5$ GeV/c [56]. The suppression is observed to be weaker than that of charged particles, while the comparison to the R_{AA} of D mesons is not conclusive and would require more precise measurements of the transverse momentum distributions.

There are several theoretical models, based on parton energy loss, which predict the charm nuclear modification factor. Figure 2.7 left compares different theoretical models to the average D meson R_{AA}. For reference, the charged particle R_{AA} are compared to the theoretical models that compute this observable, see figure 2.7 right. While comparing models that compute both observables, it is observed that radiative energy loss supplemented with in-medium D meson dissociation (I) [57, 58] and radiative plus collisional energy loss in the WHDG (II) [59] and CUJET1.0 (VII) [60] implementations describe reasonably well both the charm and light-flavour R_{AA}.

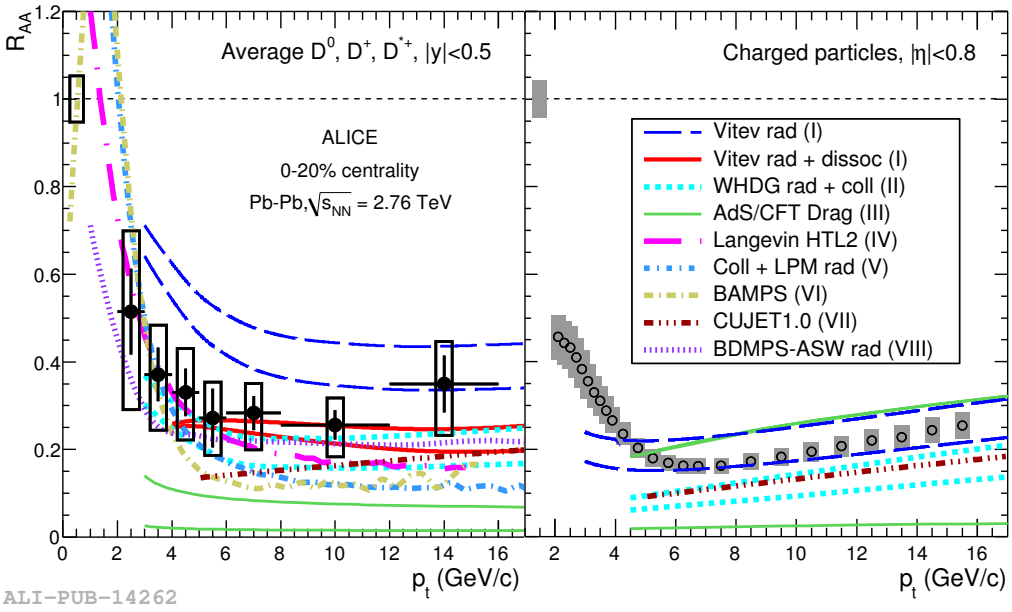

Figure 2.7: The average R_{AA} of D-mesons (left) and R_{AA} of charged hadrons (right), as measured by the ALICE collaboration, compared to various theoretical models [55]. Comparing models that compute both observables, radiative energy loss supplemented with in-medium D meson dissociation (I) [57, 58] and radiative plus collisional energy loss in the WHDG (II) [59] and CUJET1.0 (VII) [60] implementations describe reasonably well both the charm and light-flavour R_{AA}.

For higher p_T, the suppression is measured for jets associated to b-quarks in the p_T range 80 - 250 GeV/c. Compared to the measurement of J/Ψ, b-jets provide a more direct connection to the b-quark energy loss, though usually in a different p_T range. The measurements show a significant suppression of the yields in Pb-Pb collisions with respect to p-p collisions. The R_{AA} shows no strong trend versus p_T and in addition it shows a smooth decrease with increasing centrality. The b-jet suppression is further found to be qualitatively consistent with that of inclusive jets, and the absence of a strong dependence of the jet suppression on the mass of the fragmenting parton would favor a perturbative model in which the mass effects are expected to be small for large p_T [61].

2.2.3 Elliptic flow of heavy-flavour mesons

The measurement of elliptic flow of heavy-flavour mesons provide further insight into the transport properties of the medium. As heavy quarks are predominantly

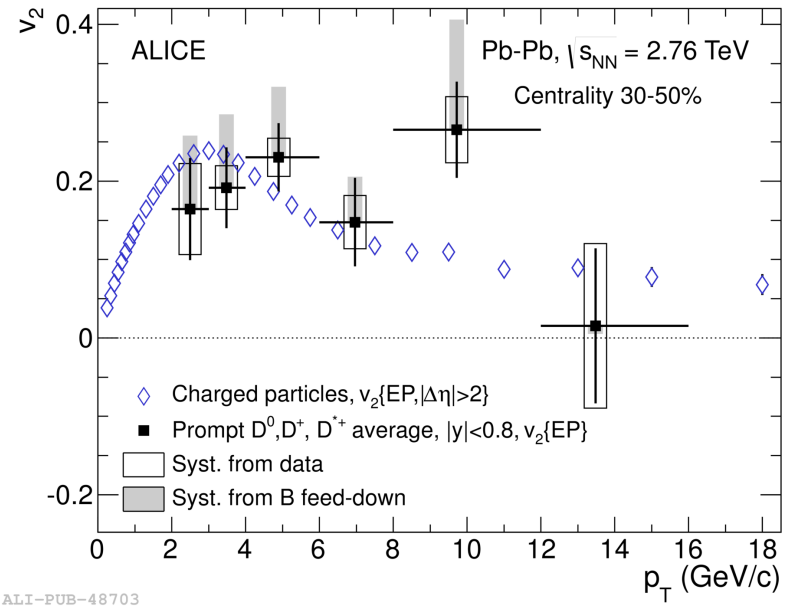

Figure 2.8: Comparison of D meson and charged particle elliptic flow, v_2, as measured by the ALICE experiment with the event plane (EP) method. The elliptic flow at low p_T is observed to be similar [62].

produced in the early stages of the collision, if not exclusively, the final state heavy-flavour hadrons at all transverse momenta will consist of heavy quarks that have experienced the full evolution of the medium. The study of the elliptic flow of heavy-flavour mesons at low p_T provides a crucial test if also quarks with large mass participate in the collective expansion dynamics, and possibly also the thermalization of the medium. The v_2 measurements at higher p_T can help constrain the path length dependence of the parton energy loss, which also complements the measurements of the nuclear modification factor of heavy-flavour particles [62].

In ALICE, the elliptic flow of heavy-flavour D mesons has been studied in the 30-50% centrality range [62]. The average v_2 of D^0, D^+ and D^{*+} mesons in the transverse momentum range 2-16 GeV/c are presented in figure 2.8. At low p_T, $2 < p_T < 6$ GeV/c, the average elliptic flow is larger than zero with 5.7 sigma significance. The figure also shows a comparison of D meson and charged hadron elliptic flow, and they are observed to be similar. The result suggests that also low momenta charm quarks take part in the collective motion of the system. There is also a hint of a positive v_2 at larger p_T, above 6 GeV/c, where the v_2 most likely originates from the path length dependence of the parton energy loss.

As a way of investigating the path length dependence of the heavy quark energy loss more closely, one has been studying the suppression of D^0 mesons in the two

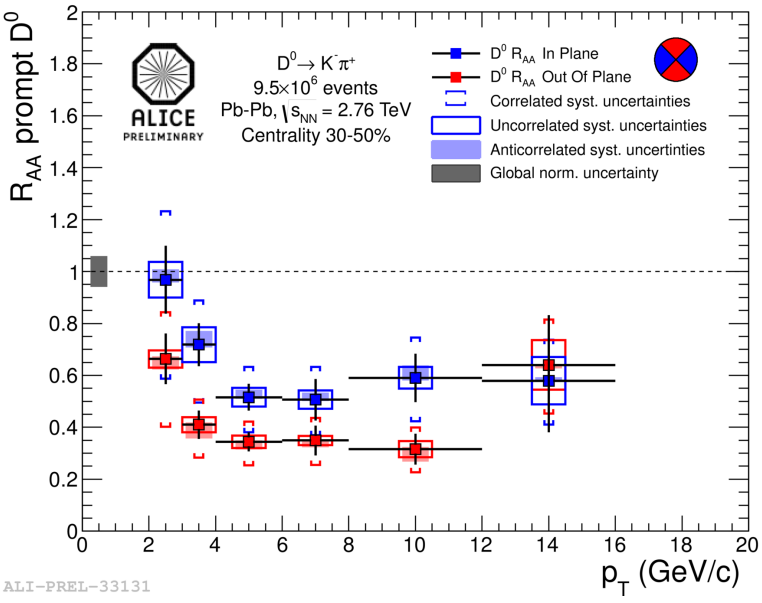

Figure 2.9: The nuclear modification factor, R_{AA}, of D^0 mesons measured by the ALICE collaboration in-plane versus out-of plane. The D^0 mesons are more suppressed out-of plane than in-plane, hinting of a collective motion and/or path length dependent energy loss [63].

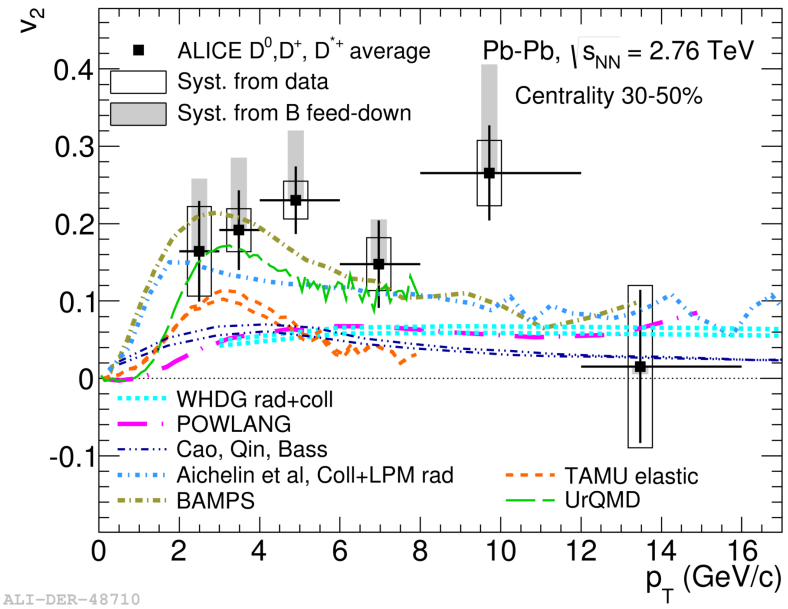

Figure 2.10: The average D meson elliptic flow, v_2, as measured by the ALICE collaboration compared to various theoretical models [62].

azimuthal regions, in-plane and out-of-plane, in the 30 - 50% centrality range [63]. Recall from section 1.2.1 that for non-central events the overlap region is almond shaped, and the out-of-plane path length will be larger than the in-plane path length. Thus, the D^0 mesons measured in the out-of-plane will have a longer path through the medium than those in-plane. The results of the measurements are shown in figure 2.9, and they indicate a larger suppression in the out-of-plane azimuthal region in comparsion to the in-plane region. The results suggests a path length dependence of the heavy-quark energy loss.

The measured elliptic flow of D mesons is compared to theoretical models, see figure 2.10. Models like POWLANG [64], which include collisional energy loss using the Langevin equation, and WHDG [59], which are considering radiative and collisional energy loss in an anisotropic medium, underestimate the elliptic flow. However, heavy-quark transport based models, like BAMPS [65] and TAMU elastic [66], seems to over/underestimate heavy-flavour suppression. Comparing the results from D meson R_{AA} and v_2, it is clear that theoretical predictions are challenged to simultaneously describe these observables.

2.3 Correlation of heavy-flavour particles

The inclusive observables R_{AA}, v_2 and differential production cross section of heavy-flavour particles measured in p-p and Pb-Pb collisions give information on the production of the heavy quarks and how they are modified in a QCD medium. However, these measurements do not give any information on the production processes of the heavy quarks and the interplay between them. Azimuthal angular correlations of heavy-flavour particles can be used for this purpose. Quarks are created in pairs, and due to momentum conservation, the heavy-quark pairs are correlated in relative azimuth in the plane perpendicular to the colliding beams. As mentioned in section 1.2.3, the quarks will later fragment into hadrons and produce sprays of particles. When measuring the relative angle between the particles inside the sprays, the signal will appear as two Gaussian-like peaks in the azimuth direction, one around $\Delta\phi = 0$ (near-side) and the other around $\Delta\phi = \pi$ (away-side).

Examples of pQCD quark production mechanisms can be the leading order process pair production (FCR), and higher order processes like gluon splitting (GS) and flavour excitation (FEX). The processes are illustrated in figure 2.11.

Figure 2.12 shows the relative importance of the different pQCD processes, as a function of $\Delta\phi^{(b\bar{b})}$ for $b\bar{b}$ pairs [68]. The predictions are made with HERWIG [69] for Tevatron Run II ($p\bar{p}$ at $\sqrt{s} = 2$ TeV). Flavour creation is important for $\Delta\phi^{(b\bar{b})} \approx \pi$, while the contributions from flavour excitation and gluon splitting can

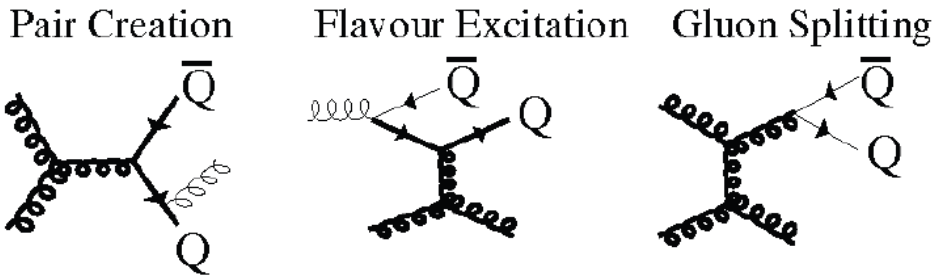

Figure 2.11: pQCD production processes in PYTHIA defined as pair creation, flavour excitation and gluon splitting. The thick lines correspond to hard processes, the thin ones to the initial- and final-state parton shower [67].

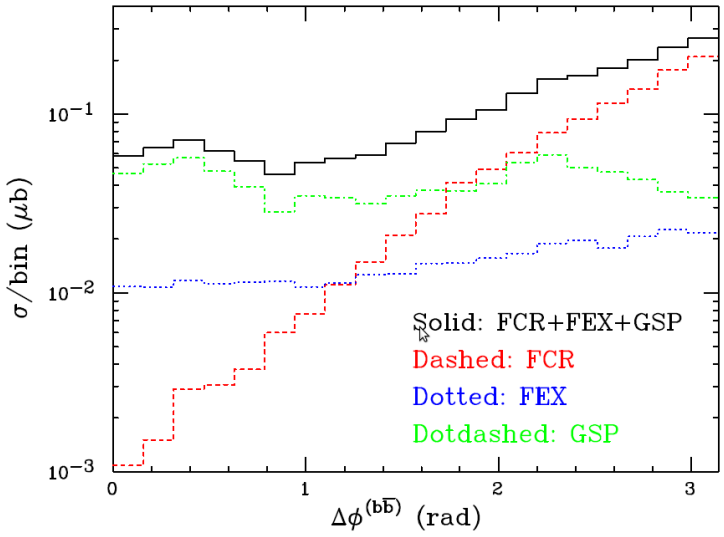

Figure 2.12: Different cross sections of pQCD production processes: Pair production (FCR), flavour excitation (FEX) and gluon splitting (GS) as a function of $\Delta\phi$ for $b\bar{b}$ pairs as predicted by HERWIG. The simulation is performed for Tevatron Run II ($p\bar{p}$ at $\sqrt{s} = 2$ TeV) [68].

not be neglected elsewhere. Although the relative importance of the processes are predicted in pQCD calculations, this is not known experimentally. By fitting the spectra obtained in correlation studies in p-p collisions one can learn more on the interplay between the processes, and in this way help constraining pQCD models.

In addition, the correlation measurements can lead to further insight into the energy loss of heavy quarks in the QGP created in heavy-ion collisions. It has been argued [70, 71] that the correlation of D mesons can provide crucial constraints on the nature of the energy loss, whether it mainly stems from radiative or collisional energy loss. As briefly mentioned in section 2.1, this has already been utilized for the light flavour sector. By comparing theoretical predictions to back-to-back di-hadron correlation measurements, and to the measured R_{AA} as a function of the angle ϕ with respect to the reaction plane, the relative fraction of collisional energy loss to the overall energy loss for light quarks has been found to be around 10% [39, 40] Similar constraints for heavy quarks will be of vital importance for the theoretical models trying to explain both the v_2 and R_{AA}. As the charm fragmentation function is rather hard, the D meson is likely to carry a large fraction of the original quark momenta. Requiring a D meson both as trigger and associated particle would give a good look at the heavy-quark energy loss in a QCD medium. However, on the experimental side, the combinatorial background of D mesons is not negligible, the reconstruction efficiency is low and the D-D correlation measurement is only possible after upgrading the ALICE detector, which is planned in 2018. As such, there are several other analyses focusing on the azimuthal angular correlation of heavy-flavour particles:

- **D-e correlation**: This analysis is the focus of this thesis, where a D-meson is required as trigger, while the away-side particle is selected to be an electron decaying from a heavy-flavour meson. This ensures that the heavy-quark partonic structure has been present, but compared to the D-D correlation, the information on the away-side is blurred out by the decay kinematics. As a fraction of the D mesons and electrons comes from the decay of bottom quarks, this analysis also has the potential of being used for separating out the contributions from c and b quarks. The main challenges for the analysis is to get a high purity sample of heavy-flavour electrons, and even with the relaxed conditions of the associated particle being an electron, the statistics available is limited.

- **D-h correlation**: Requiring a D meson as trigger, but the associated particle is only required to be a hadron. This will increase the statistics. The main aim of this analysis in p-p collisions is to get the relation of pQCD to the underlying event.

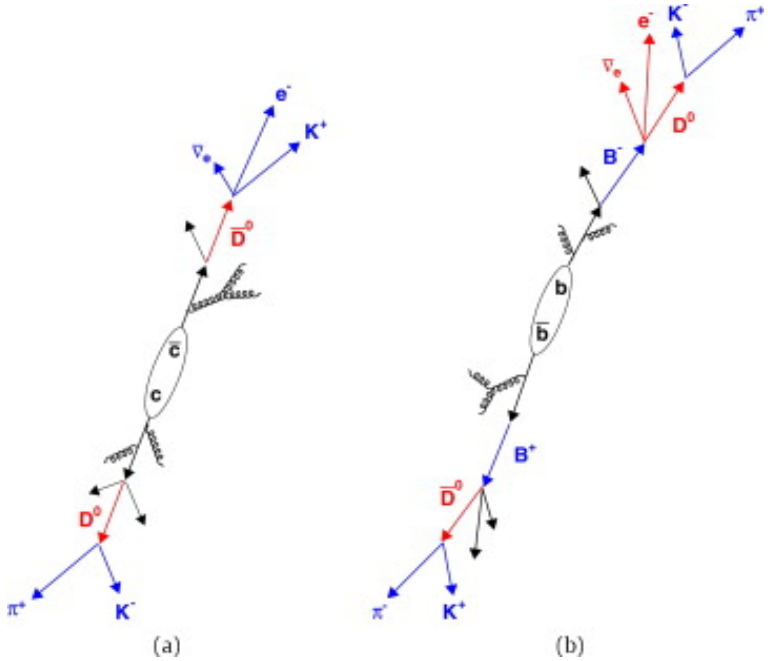

Figure 2.13: Schematic view of the fragmentation of a $c\bar{c}$ (left) and a $b\bar{b}$ (right) pair [72].

- **e-h correlation**: The trigger particle is required to be an electron from a semileptonic decay of a heavy-flavour meson, while the associated particle is selected as a charged hadron. The main aim of this analysis is to use the features of the near-side to compute the b/b+c ratio, see the next section.

Separation of the charm and bottom contributions

The selected D^0 mesons and HFEs will originate from both charm and bottom quarks. The charm quark will predominantly fragment directly to a D^0 meson (c$\rightarrow D^0$ + X, BR = 56.5 $\pm$ 3.2%), while the bottom quark produces D^0 mesons via B meson decay (b $\rightarrow B^-/\bar{B}^0/\bar{B}^0_S \rightarrow D^0$ + X, BR = 59.8 $\pm$ 2.9%). The branching ratio of charmed and bottom mesons decaying to electrons is 9.6% and 10.86%, respectively [12, 72]. The heavy-flavour pair could thus be tagged using D^0 mesons and heavy-flavour electrons; figure 2.13 shows an example of how a fragmentation of the charm and bottom quark could look like. As illustrated in this chapter, it is necessary to investigate the separate contribution of charm and bottom quarks to understand the energy loss of them separately. The azimuthal angular correlation of D mesons with heavy-flavour electrons are suited for this purpose.

The shape fitting method is the most established method used to separate the bottom and charm contribution. The method focus on the shape of the near-side

peak in the correlation distribution. The B and D hadrons, containing bottom and charm quarks respectively, have different energy releases. Electrons decaying from B mesons with high p_T does not have to decay from a B meson with large transverse momentum, as the electron can get the momentum from the b-quark mass. This is in contrast to electrons from D meson, where the D meson needs to have large p_T in order to boost the electron to a high p_T. Thus, the decay daughters of the B mesons have a larger mean transverse momentum relative to the flight direction of the mother particle [73], and the near-side peak in the correlation distribution will be broader for bottom quarks than for charm quark pairs. In addition, the B mesons have a longer decay chain, which will further broaden the width of the angular distributions. As a result, one can use the near-side peak of the correlation distribution to separate out the contribution from bottom quarks, and thus also extracting the charm contribution from the total distribution.

The shape fitting method has already been employed for the azimuthal angular correlation of HFEs with charged hadrons at both the STAR and ALICE experiments [74, 75]. The separation is performed using a PYTHIA based Monte Carlo template, where azimuthal angular correlation distributions between electrons and charged hadrons have been computed for bottom and charm quarks. The relative bottom contribution is extracted by fitting the $\Delta\phi$ correlation distribution obtained from data with the $\Delta\phi$ correlation templates for D and B mesons on the near-side:

$$\Delta\phi^{HF}_{e-h} = const + r_B \Delta\phi^{B}_{e-h} + (1 - r_B)\Delta\phi^{D}_{e-h} \tag{2.4}$$

r_B is the relative ratio of electron yield from B meson decays to that of the HFE yield and *const* gives the uncorrelated background. $\Delta\phi^{D}_{e-h}$ ($\Delta\phi^{B}_{e-h}$) is the azimuthal angular correlation between electrons from D(B) meson decay and charged hadrons from Monte Carlo simulations.

An example of a $\Delta\phi$ distribution for the p_T region 2.5 - 3.5 GeV/c of the trigger electron as measured by ALICE, is shown in figure 2.14, including also the template for electrons from D and B mesons. The computed ratio, with a comparison to FONLL, is shown in figure 2.15, and they are found to be in agreement within the statistical uncertainties.

There are also other techniques available for the azimuthal angular correlation of D^0 mesons and heavy-flavour electrons, one of these techniques is based on the charge parity of the correlated D^0 meson, or rather the charge of the detected kaon, and the electron [72, 76, 77]. By using a PYTHIA Monte Carlo simulation it is argued that the main contribution in the near-side peak for like-signed values of the electron and kaon pair is from bottom pairs, while the away-side has a 75% contribution from charm and $\sim$ 25% contribution from bottom. For unlike-sign pairs the

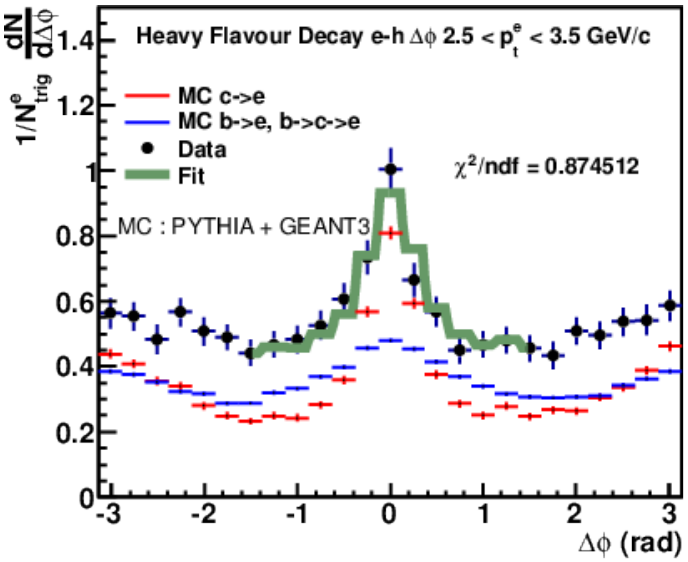

Figure 2.14: $\Delta\phi$ distributions of electron-hadron correlations in different p_T bins as measured by the ALICE experiment [75].

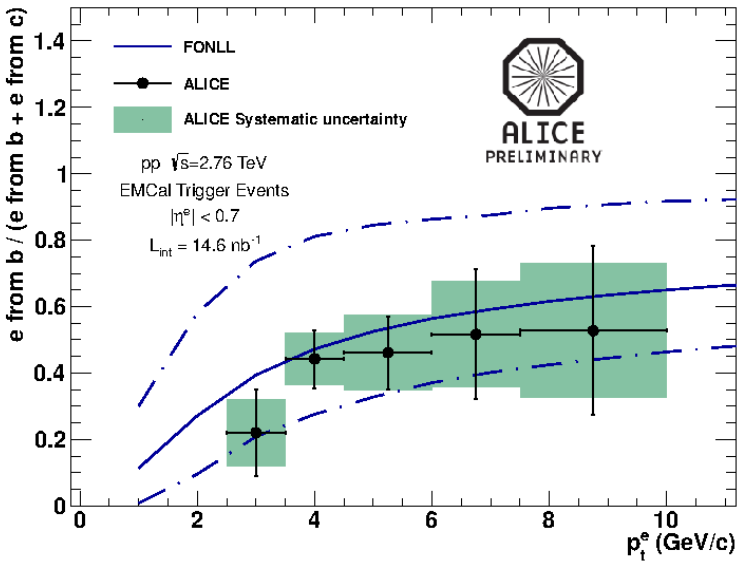

Figure 2.15: The calculated ratio of electron from bottom over electrons from heavy flavour decays as measured by the ALICE experiment. The ratio is also compared to pQCD calculations (FONLL) and they are in agreement within uncertainty [75].

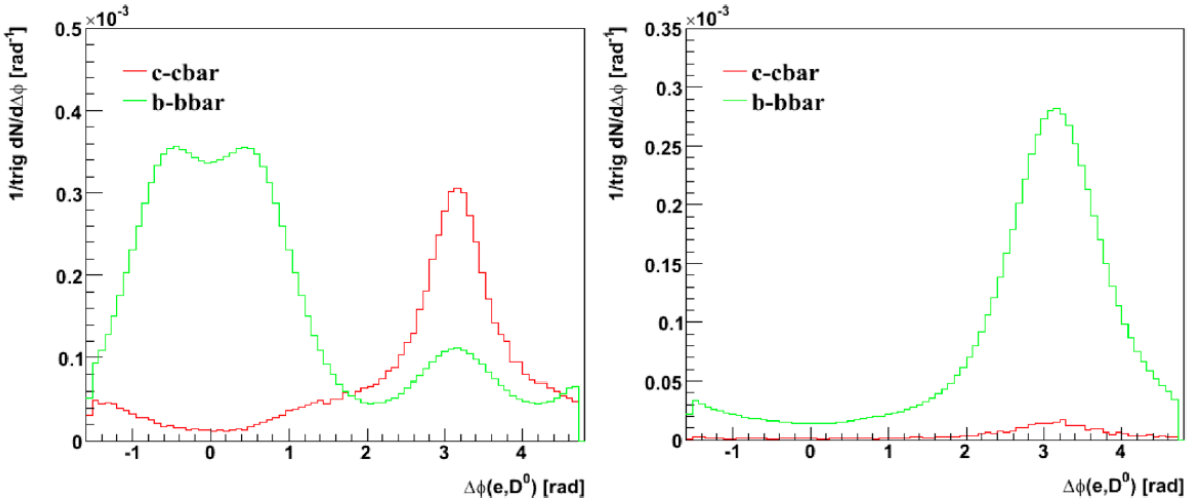

Figure 2.16: Azimuthal angular correlation distribution from PYTHIA Monte Carlo simulations for charm and bottom pairs, using the charge of the detected kaon and electron. Right: Like-signed pairs, the biggest contribution comes from bottom pairs, while the away-side have a larger contribution from charm pairs. Left: Unlike-signed pairs, the main contribution in the away-side peak stems from bottom pairs [76].

main contribution on the away-side is from bottom, see figure 2.16. Thus, by requiring like and unlike sign electron-kaon pairs, one can get a relatively pure sample of charm and bottom pairs in the near- and away-side. This method has already been employed by STAR at RHIC [74, 78], and the ratio of the bottom contribution to the overall heavy-flavour contribution is shown in figure 2.17. The figure shows two data points from the e-D^0 correlation analysis, the data has been fitted using the two different Monte Carlo simulations, PYTHIA and Next-to-Leading-Order (NLO) Monte Carlo. The rest of the data points come from the electron-hadron correlation analysis in STAR. It can be seen that the two analysis methods are in agreement with each other and also to the FONLL pQCD prediction, within statistical uncertainties.

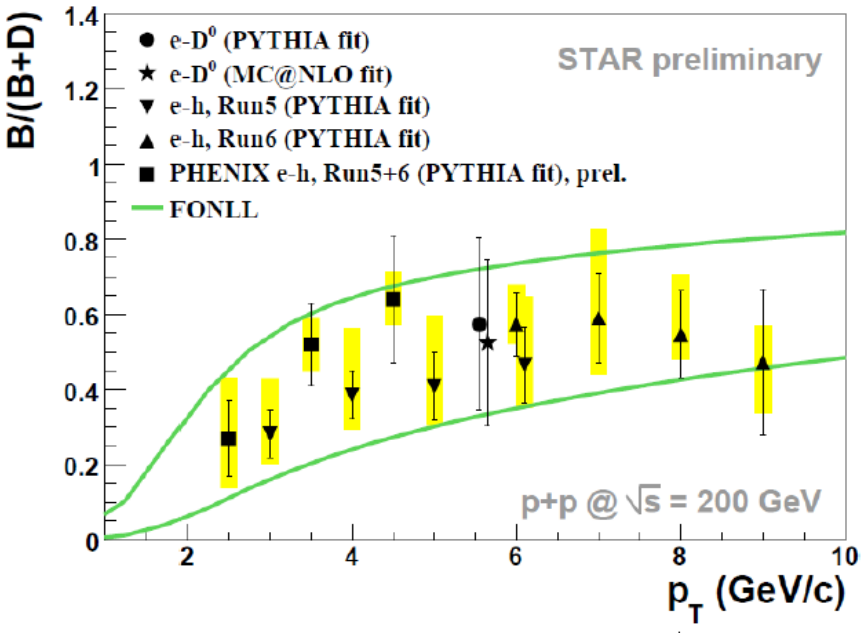

Figure 2.17: Ratio of contribution from B mesons to the overall contribution from heavy-flavour mesons, as extracted from the azimuthal angular correlation of HFEs with hadrons. There is also contribution from the azimuthal angular correlation measurements of HFE with D^0 mesons, which have been fitted with a PYTHIA and Next-to-Leading-Order (NL0) Monte Carlo simulations. The measurements are in agreement with each other within statistical uncertainties. The measurements are also compared to FONLL calculations, and are also consistent with them [74, 78].

Chapter 3

Experimental setup

This chapter will focus on the experimental setup, the ALICE detector at the LHC with special focus on the sub-detectors which are important for performing the analysis in this thesis.

3.1 Large Hadron Collider (LHC)

The Large Hadron Collider (LHC) is situated at the CERN[1] laboratory on the Swiss/French border right outside Geneva. It is a circular accelerator 100 metres underground with a circumference of 27 km. It has been designed to accelerate and smash protons with a center-of-mass energy $\sqrt{s} = 14$ TeV, and also to collide heavy-ions like Pb-ions with a center-of-mass energy $\sqrt{s_{NN}} = 5.5$ TeV. The first recorded proton-proton collision took place in November 2009[2] with the first recorded colliding Pb-ions a year later, and in September 2012 the first collisions of protons with Pb-ions took place. By the end of the first running period of LHC, the experiments connected to the accelerator had discovered two previously unobserved particles (the Higgs Particle and the χ_B (3P) bottomonium state) and created the Quark-Gluon-Plasma, to name a few key discoveries.

There are four main experiments at the LHC, CMS[3], ATLAS[4], LHCb[5] and ALICE and figure 3.1 shows the experiments and their location along the LHC. The ATLAS and CMS experiments are large, multipurpose detectors, LHCb is mainly focusing on bottom quark physics, while the ALICE experiment was mainly built to

[1]The European Organization for Nuclear Research

[2]The first collision actually took place September 2008, but 9 days after the start-up, a faulty electrical connection caused the accelerator to postpone its further data-taking by another year

[3]Compact Muon Solenoid

[4]A Toroidal LHC Apparatus

[5]Large Hadron Collider beauty

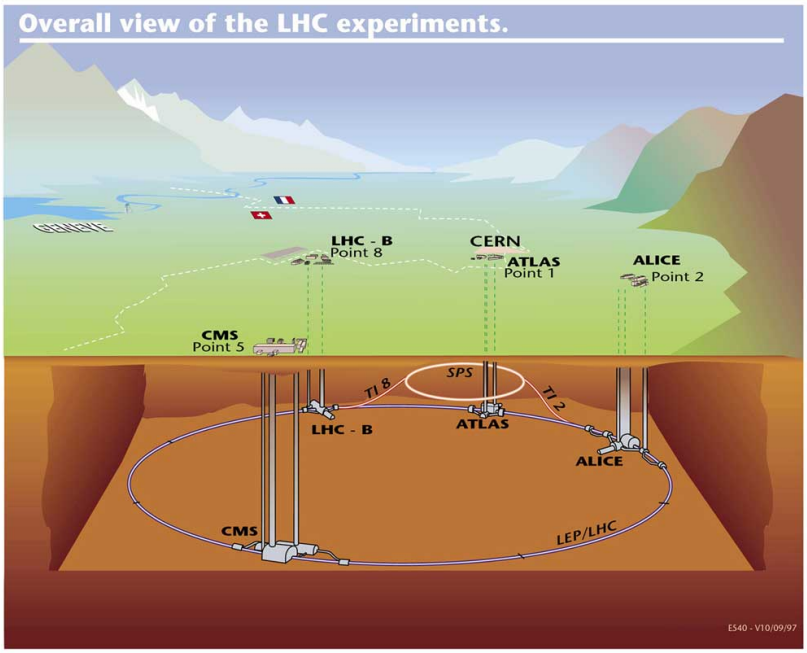

Figure 3.1: Picture showing the LHC and the four main experiments along the collider and where they are situated [79].

study heavy-ion collisions. The four experiments operate at different luminosities tuned to each detector individually.

3.2 A Large Ion Collider Experiment (ALICE)

ALICE (A Large Ion Collider Experiment) is the only dedicated heavy-ion experiment at the LHC. Compared to the other LHC experiments, ALICE has a unique low p_T coverage and also a unique capability to identify particles.

The detector includes a central barrel system with several detector systems, and a muon spectrometer placed at forward rapidity. The most important detectors for the analysis described in this thesis is the Time Projection Chamber (TPC), Inner Tracking System (ITS), Time-Of-Flight (TOF), the Transition Radiation Detector (TRD) and the ElectroMagnetic CALorimeter (EMCAL). Some of the discussed detectors are already included in the analysis in this thesis, others are to be included in the future. A schematic overview of the detector with all its sub-detectors is shown in figure 3.2. The cross section of the central barrel is shown in figure 3.3 to more easily see where the sub-detectors are placed.

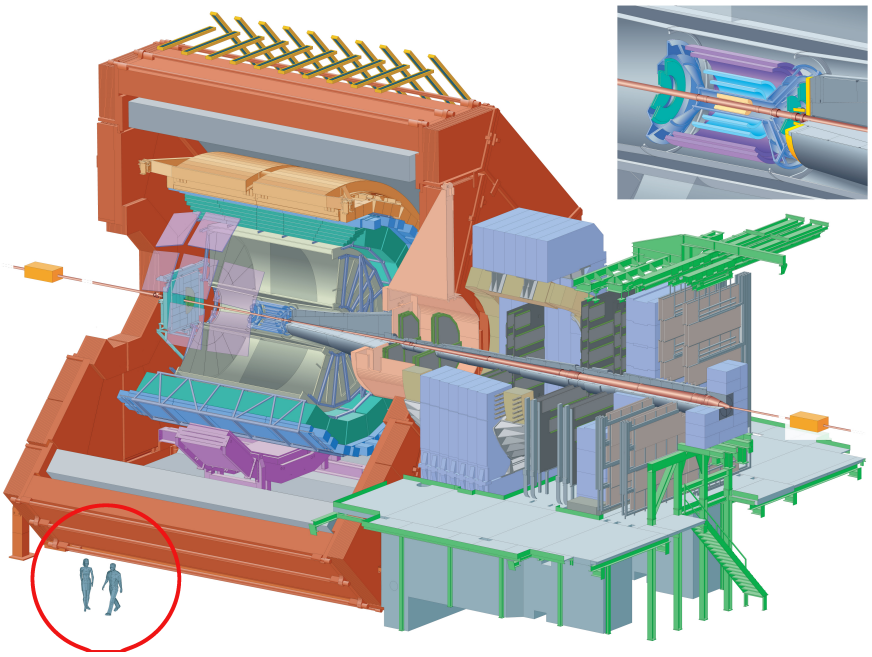

Figure 3.2: Schematic picture of the ALICE experiment showing the central barrel detectors and the forward muon spectrometer [80].

3.2.1 Inner Tracking System

The Inner Tracking System (ITS) is the detector closest to the beam-pipe, see figure 3.4. The main tasks for the ITS is to reconstruct a primary vertex with a spatial resolution better than 100 μm, to reconstruct secondary vertices from decays of hyperons and D and B mesons, to track and identify particles below 200 MeV/c, to improve the momentum and angle resolution for particles reconstructed by the TPC detector and to reconstruct particles traversing dead regions of the TPC. The relative momentum resolution achievable by the ITS detector is better than 2% for pions with transverse momentum between 100 MeV/c and 3 GeV/c. The ITS has a pseudorapidity-range of $|\eta| < 0.9$ with an extended coverage in the first layer, $|\eta| < 1.98$, to provide, together with Forward Multiplicity Detector (FMD), continuous coverage for the measurement of charged-particle multiplicity.

The ITS combines three different silicon detector techniques, and has in total six layers which extend a radius between 4 and 43 cm. The granularity of the detectors was designed to cope with the upper limits of theoretical predictions of the expected particle density, and thus the four innermost layers are made of silicon pixel and drift detectors. The four outermost layers have analog readout and can be used for dE/dx measurements in the non-relativistic region. As a result, ITS has the capability of performing stand-alone as a low-p_T particle spectrometer.

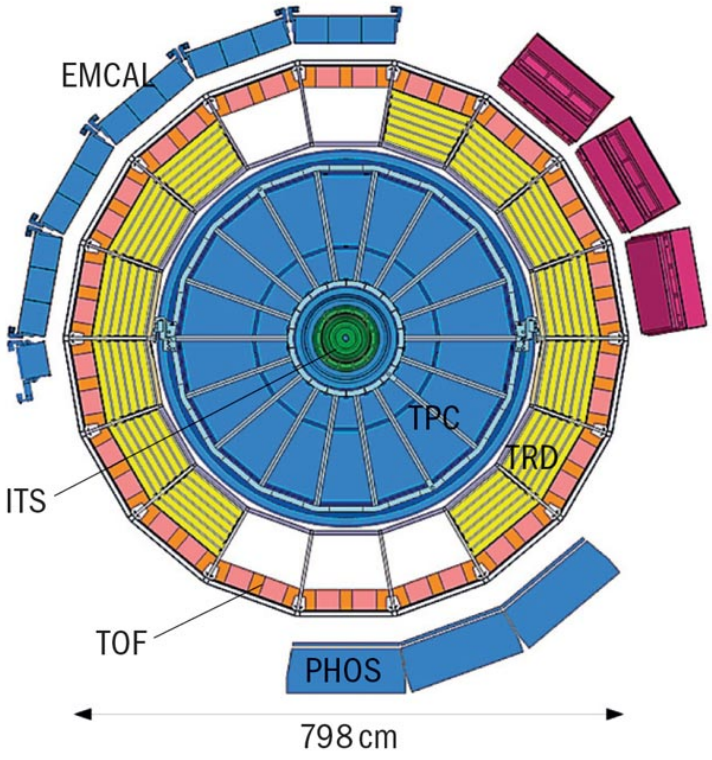

Figure 3.3: Cross section of the ALICE detector illustrating where the different sub-detectors in the central barrel system are located.

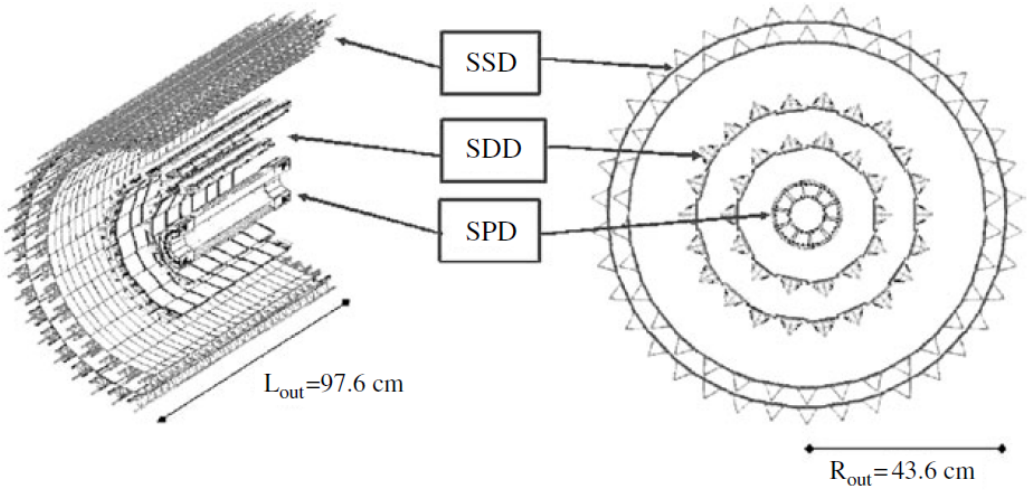

Figure 3.4: A schematic overview of the ITS detector. It consists of six cylindrical layers using three different detector technologies [81].

The two innermost layers of the detector consist of silicon pixel detectors (SPD) at radius 3.9 and 7.6 cm. They provide a spatial resolution of 12 μm in the plane perpendicular to the beam axis and 100 μm along the beam axis. The detector is based on hybrid silicon pixels, and each pixel chip provides a Fast-OR digital pulse when one or more of the pixels in the matrix are hit. The detector has a total of 9.8 million pixels read out by 1200 chips, and the signals from these chips are combined in a programmable logic unit and are used for the minimum bias trigger (see section 3.2.6).

The next two layers are made of silicon drift detectors (SDD) at radii 15 and 23.9 cm. These layers allow to measure a hit along the z direction with a resolution better than 30 μm from the centroid of the signals collected on the anodes, and to determine the ϕ coordinate from the drift time with a resolution depending on the level of calibration. The two outermost layers are Silicon Strip Detectors (SSD), which are double-sided silicon strip sensor modules with an intrinsic spatial resolution of 20 ($r\phi$) x 830 (z) μm^2.

It is very important to know the exact material budget of the detectors, especially the innermost detectors. This is because photons will convert to electron pairs in the material (conversion electrons), and they are an important source of background. The total material budget is 7.7% of X_0 for tracks crossing the ITS perpendicular to the detector surfaces (η=0). This allows for measurements of the track impact parameter (DCA) in the bending plane ($r\phi$) with a resolution better than 75 μm for transverse momenta bigger than 1 GeV/c.

3.2.2 Time Projection Chamber

The Time Projection Chamber (TPC) surrounds the ITS and is the main tracking detector in ALICE as it provides a reliable performance even within the upper limit of particles estimated by theoretical predictions for Pb-Pb collisions. The TPC is a large, cylindrical gaseous detector used for both particle tracking and particle identification, with a radius from 85-247 cm and spanning the beam direction from -250 cm to 250 cm. The inner radius is determined by the maximum acceptable hit density, while the outer radius is determined by the length required for achieving a dE/dx resolution better than 5-7%. Figure 3.5 shows the schematics for the TPC layout.

The gas inside the detector is a mixture of Ne (85.5%), CO_2 (9.5%) and N_2 (4.8%). A central electrode of 100kV divides the gaseous volume into two parts. The central electrode provides an electrical drift field of 400 V/m, which results in a maximum drift time of 94 μs. The end caps are equipped with MultiWire Proportional Chambers (MWPCs), and a particle traversing the detector can be

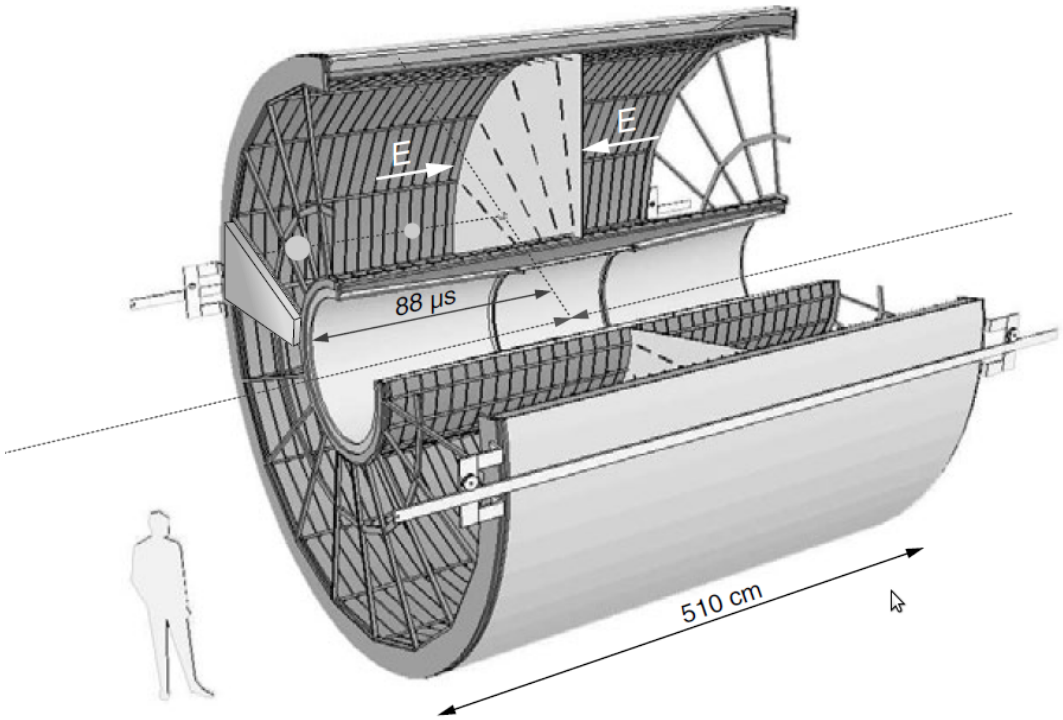

Figure 3.5: Schematics of the TPC detector layout [81].

recorded with up to 159 three-dimensional space-points, also referred to as clusters. These can be used to reconstruct the particle trajectories in the gaseous chamber, in addition to calculating the specific energy loss of the particle, which is used for particle identification. With a magnetic field of 0.5 T, the transverse momentum resolution of charged tracks in the ITS/TPC ranges from 1% at $p_T < 1$ GeV/c to about 3% at 10 GeV/c.

When the information from the TPC is combined with information from the ITS, the impact parameter resolution can be better than 65 μm for $p_T > 1$ GeV/c in the bending plane in Pb-Pb collisions, which allows for reconstruction of secondary vertices.

3.2.3 Transition Radiation Detector

The Transition Radiation Detector (TRD) is located outside the TPC at 2.9 m radial distance from the beam-pipe. It is designed to perform particle tracking and particle identification, more specifically to separate electrons from pions for transverse momenta above 1 GeV/c. It is also designed to study production rates of quarkonia and heavy quarks near mid-rapidity. The TRD is segmented in azimuth direction into 18 super-modules. Each super-module is segmented into 5 units along

the beam direction, each consisting of six layers in the radial direction. The detector elements are made up of a fiber sandwich radiator (48 mm), a drift section (30 mm) and a MultiWire Proportional Chamber section (7 mm) with pad readout. The drift section consists of a gas with a mixture of Xe (85%) and CO_2 (15%). The separation of electrons from pions is accomplished by measuring the transition radiation photons which are produced more abundantly for electrons than for hadrons. The TRD also provides a fast trigger with PID information in order to discriminate electrons from hadrons, however, this trigger was not employed for the data sample used in this analysis.

3.2.4 Time-Of-Flight detector

The Time-Of-Flight (TOF) detector is located further out, at radius 3.7 metres. It is designed for particle identification in the intermediate momentum range, below 2.5 GeV/c for pions and kaons and up to 4 GeV/c for protons, with the capability of separating pions from kaons and kaons from protons better than 3σ [80]. The detector is based on Multigap Resistive Plate Chambers (MRPCs) and it covers the full azimuth. The complete TOF detector system consists of 90 modules, which is segmented into 18 sectors in azimuth and 5 segments along the beam direction. It should be mentioned that three of the central modules in front of PHOS have not been installed in order to reduce the material in front of this calorimeter.

The particle identification strategy in the TOF detector is based on the difference between the arrival time, measured by the TOF detector, and the event time, which is estimated event-by-event. As such, the time resolution is a crucial aspect to the TOF detector, and the global time resolution have been measured to be around 80 ps [82]. The event time, or start time, is measured by the T0 detector, dedicated for this purpose. The T0 detectors consists of Cherenkov counters placed along the beam axis at +350 cm and -70 cm. If a T0 signal is not present, which can happen in a fraction of the events due to the detector acceptance, especially for p-p collisions, an estimate based on the particle arrival times at the TOF detector is computed. In case of neither, an average start time is used.

3.2.5 Electromagnetic Calorimeter

The ElectroMagnetic CALorimeter (EMCAL) is a large Pb-scintillator sampling calorimeter located at a radial distance 4.5 metres away from the beam line [80]. The fully commissioned detector covers pseudorapidity range $|\eta| < 0.7$ and azimuthal coverage $\Delta\phi = 107^o$. However, as only parts of the detector were installed for the 2010 running period, the azimuthal coverage was limited to only 40^o. The detector

is positioned approximately on the opposite side of another calorimeter in ALICE, namely the PHOton Spectrometer (PHOS). EMCAL is built of alternating lead and scintillator tiles, together with longitudinal wave-length shifting fibers. The energy resolution has been determined to be $1.7 \oplus 11.1 / \sqrt{E(GeV)} \oplus 5.1$ /E(GeV)%.

The EMCAL detector provides a fast and efficient trigger for hard jets, photons and electrons, which allows ALICE to exploit the full luminosity of LHC.

3.2.6 VZERO

The VZERO detector is both used for measuring event centrality and it is also used as a trigger. It consists of two separate detectors, VZEROA and VZEROC, which is placed on both sides of the central barrel detectors, at +3.3 m and -0.9 m. They cover a pseudorapidity range $2.8 < \eta < 5.1$ and $-3.7 < \eta < -1.7$ and record the amplitude and arrival time of signals produced by charged particles. The VZERO time resolution is better than 1 ns. The sum of the amplitudes of the signal is used for measuring the event centrality, and the trigger is issued if at least one particle hit was detected. This signal is utilized, among other things, in the minimum bias trigger. The minimum bias trigger uses a combination of the trigger from VZEROA, VZEROC and SPD, where at least two out of three of the following are required:

- At least two pixel chips hit in the outer layer of SPD
- a signal in VZEROA
- a signal in VZEROC

3.3 Particle Identification in ALICE

The ALICE detector has excellent Particle IDentification (PID) capabilities, which have been central in the design phase of the entire detector and covers a large part of the phase space and many particle species. Several of the subsystems are used for PID, like TPC, TRD, TOF and EMCAL.

Figure 3.6 shows the energy loss of electrons, pions, kaons, protons and deuterons in the TPC. The theoretical calculation of the energy loss for each particle species is indicated as black lines in the plot, and the PID selection is based on the difference between measured and expected value, performed for each particle species. Notice that all lines approaches the same value at high transverse momentum, thus PID using energy loss is no longer applicable.

PID using the TOF detector has already been described in section 3.2.4, and figure 3.7 shows the measured particle velocity, β, as measured by the TOF detector

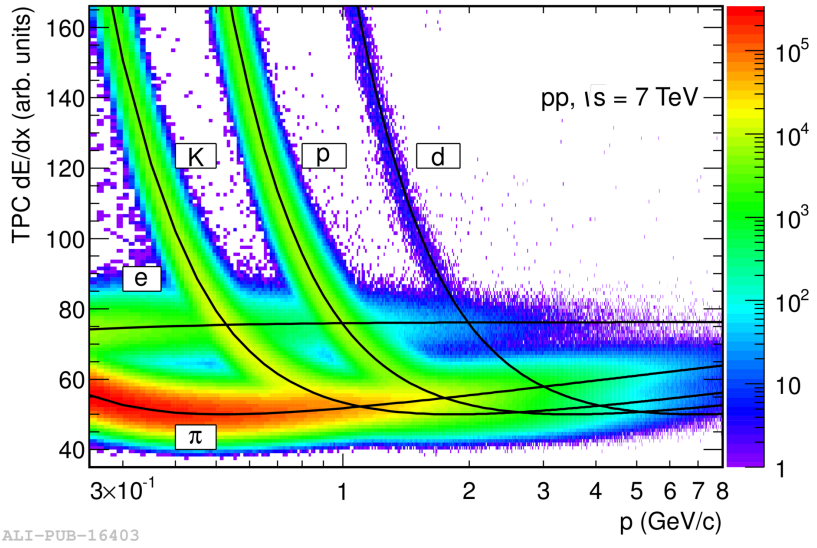

Figure 3.6: The specific energy loss in the TPC, dE/dx, versus momentum [46].

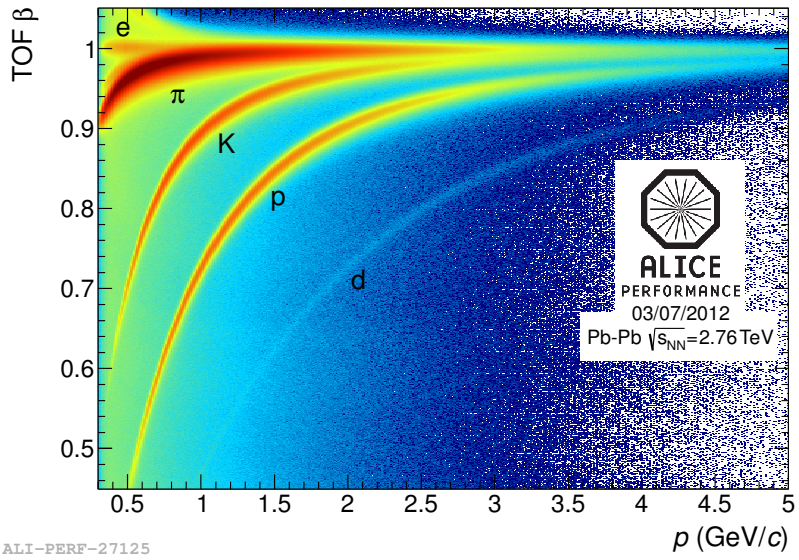

Figure 3.7: Correlation of particle velocity β =v/c versus the particle momentum as measured by the TOF detector for Pb-Pb collisions. The bands for electrons, kaons, pions and deutrons can clearly be seen.

versus the particle momenta p. Pions, kaons and protons are clearly separated in the intermediate momentum range. Information from the TOF detector combined with information from the TPC detector is used in the analysis presented in this thesis both to identify the daughters of D^0 mesons and to enhance the electrons in the sample after track cuts. In addition, the TRD detector can be used for the identification of electrons in higher p_T regions, and the EMCAL detector can also be used for electron identification.

3.4 High-Level Trigger

The High Level Trigger (HLT) is a part of the ALICE trigger scheme, which also includes three hardware triggers L0, L1 and L2. It is implemented on a computer farm and aims at selecting events based on their physics content. The HLT is designed to be operated with an input data rate of 25 GB/s, and the main objective is to reduce the data stream down to the permanent storage bandwidth, namely at 4 GB/s.

Events triggered at L0 level and accepted at L1 and L2 levels are subsequently fed into the HLT system where they are processed and reconstructed in real-time. The reconstructed tracks and vertices are stored in Event Summary Data (ESD) blocks, which are of identical format to those used by the off-line analysis. A more detailed description of the tracking and reconstruction scheme in HLT can be found for instance in [83]. The HLT issues trigger decisions based on the physics content of the event, and both the reconstructed event and the trigger decision, as part of the HLTOUT data, are passed on to the Data Aquisition (DAQ). DAQ will subsequently either reject the event or partially or fully store the HLTOUT data together with the raw data from the detectors to permanent storage.

In addition to performing selection of events based on the physics properties, HLT is also used to reduce the data volume from the TPC detector. This is especially important for Pb-Pb collisions. Rather than storing the raw data from the TPC detector, the clusters in the TPC detector calculated by HLT are stored in a compressed data format. These compressed clusters will later be used in the off-line reconstruction. An average compression factor of 4.4 has been achieved for Pb-Pb collisions [84], and it has been verified that the compression does not significantly reduce the physics performance.

Since the trigger decision is based on real-time reconstructed events, it is important to monitor the quality of the reconstruction, where the main focus is to look at the quality of the track and event reconstruction. After the compression of the TPC clusters was introduced before the Pb-Pb collision data taking in 2011, it has

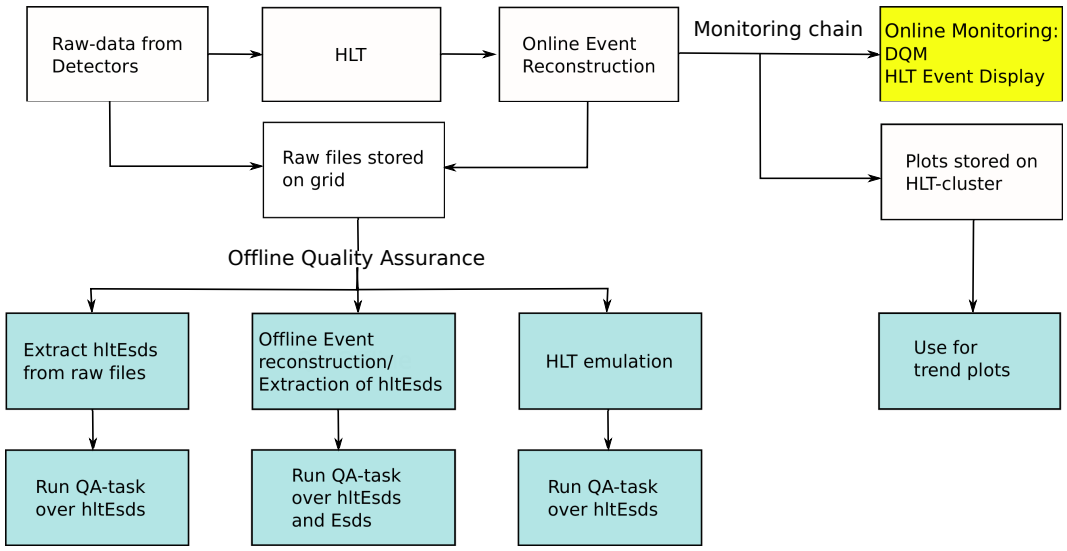

Figure 3.8: Data flow for the HLT monitoring. The yellow box indicates the on-line monitoring while the blue boxes indicate the off-line monitoring [85].

also been necessary to monitor the quality of the compression. HLT provides this monitoring, giving also the opportunity to inspect the collisions in real-time using histograms and an event-display [85].

The monitoring of the HLT TPC and ITS tracking and compression of TPC data is performed in two stages, during data-taking and after data has been transferred to permanent storage. This is referred to as on-line monitoring and HLT off-line Quality Assurance (QA), respectively. An overview of the monitoring scheme is shown in figure 3.8.

The on-line monitoring (yellow) involves the creation of monitoring histograms. These histograms are stored in the HLT computing cluster and they are also displayed in the Data Quality Monitoring (DQM). DQM is part of the DAQ system in ALICE and provides an on-line feedback on the quality of the recorded data. It involves on-line gathering of data, detector specific analysis algorithms and visualization of monitored data [86][87]. DQM forms a very important backbone in the on-line monitoring as there is always people monitoring the histograms during data taking and they will immediately issue notifications if an error or warning occurs.

The histograms are further used to create trend plots. These plots show the mean value of monitored quantities versus the run number. The recording of data by the ALICE detector is performed in bulks, referred to as runs. When the ALICE stops recording data for a little while, either because of problems reported by the LHC control room or due to an internal problem in ALICE, a new run will start. These runs are marked with a run number. An example of a trend plot is shown

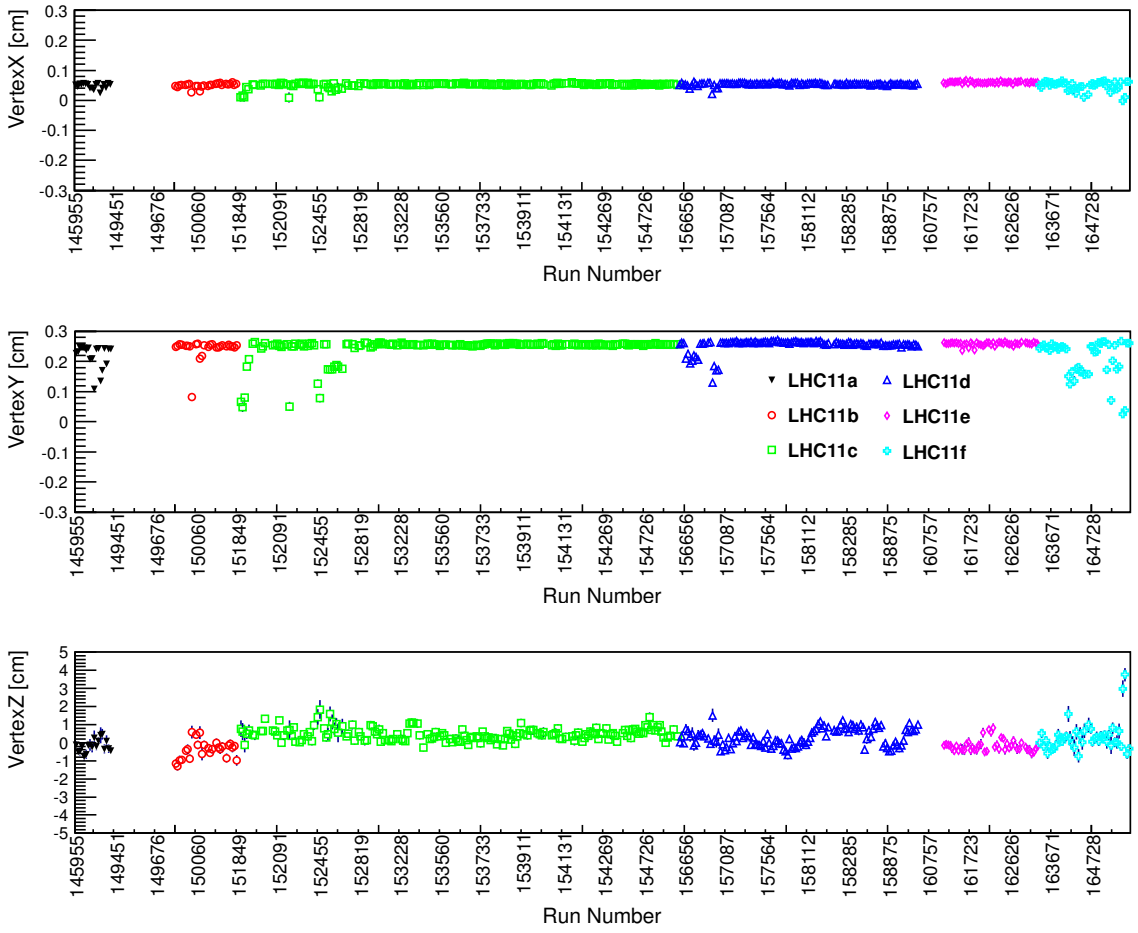

Figure 3.9: 2011 p-p data trends - the average value of SPD vertex X, Y and Z coordinates per run [85].

in figure 3.9, where the trend of the X, Y and Z coordinate of the reconstructed collision vertex in p-p collisions recorded in 2011 is shown. The trend is illustrated for different running periods. The trend for the SPD vertex shows that the vertex distributions are generally quite stable, with some outliers. After a careful examination it was noticed that the outliers have a higher background and this could explain the lower mean value. Some of the runs are also marked by the off-line group as "bad" runs and will not be part of the recorded data used for physics analysis. Thus, this is not a performance issue related to the on-line reconstruction but rather illustrates changes in the data recording conditions.

Another part of the on-line monitoring is the on-line event display. It provides a visual display of a fraction of the reconstructed events. Figure 3.10 shows a Pb-Pb collision recorded in 2011, produced from the HLT reconstructed data.

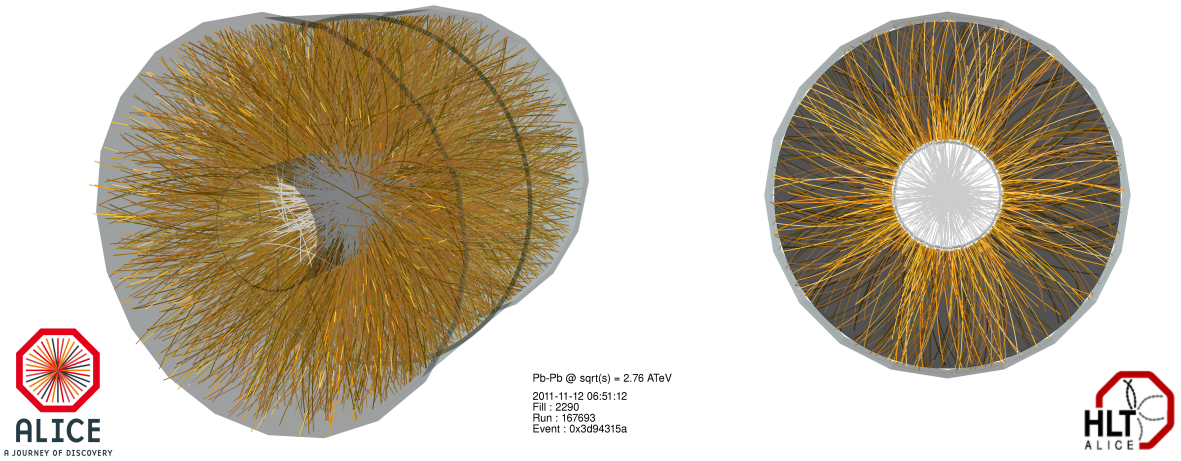

Figure 3.10: Pb-Pb collision recorded during Pb-Pb data taking period in 2011. The HLT reconstruction was used to produce the plot.

HLT off-line Quality Assurance (blue) involves inspection of the on-line reconstruction output and comparison with the off-line reconstruction. It also involves rerunning the reconstruction in an HLT emulation. During off-line reconstruction, the on-line HLT ESD data blocks in the HLTOUT data are extracted from the raw data and stored in parallel to the off-line ESD data. As the formats of the two are identical, subsequent analysis can be applied to either the ESD or HLT ESD, or both.

Because no further event reconstruction is required, data from HLTOUT can be very quickly extracted from raw data files immediately after the data has been registered on permanent storage. This allows for a fast feedback on the quality of the on-line reconstruction and calibration, independently of the central reconstruction cycle.

In addition, there is a HLT emulation in place which makes it possible to run the HLT reconstruction off-line. At this stage one has access to the calibration used in the off-line reconstruction, which makes it possible to run the HLT reconstruction algorithms with improved calibration. The HLT emulation is thus a good tool to assess the quality of the calibration used in the on-line reconstruction and also very valuable when assessing an update in the reconstruction algorithm.

As mentioned, the HLT reconstructed clusters replaced the TPC raw data during the Pb-Pb collision data taking in 2011. The trend of the HLT TPC data reduction is shown in figure 3.11, and illustrates a very stable performance of the data compression over the entire Pb-Pb running period in 2011. The missing points are

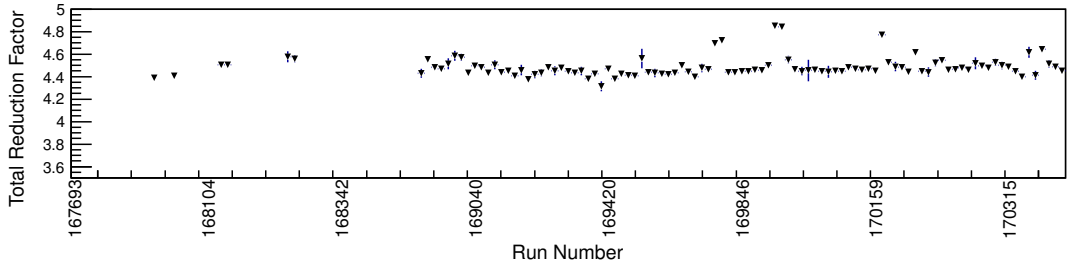

Figure 3.11: Trend of the total reduction factor when using HLT TPC clusters compared to TPC raw data in Pb-Pb 2011. The missing points are runs where the monitoring histograms were not available [85].

runs where the monitoring histograms were not available due to technical problems in the beginning of the Pb-Pb run period. Due to the good performance of the HLT data compression scheme, it was decided to also use it in the 2012 running period.

Chapter 4

Reconstruction of D^0 mesons and selection of HF electrons

This chapter will focus on the reconstruction of D^0 mesons and the selection of electrons decaying from heavy-flavour mesons. The main part of the analysis in this thesis has been performed on the p-p collision data taken in 2010. The collisions have been selected based on the minimum bias trigger, see section 3.2.6. It has been estimated that this trigger configuration is sensitive to about 87% of the p-p inelastic cross section [88]. The analysis presented in the following is based on 3.2x10^8 minimum bias events.

4.1 Reconstruction of the D^0 meson

D^0 mesons have a mean proper decay length of 123 μm [12]. As a result, the majority decays before the particles reach the first layer of the ITS and the particles have to be reconstructed via their decay products. This thesis has focused on the reconstruction of the D^0 meson and its antiparticle, in the central rapidity region of ALICE, via the hadronic decay channel $D^0 \rightarrow K^-\pi^+$, which has a branching ratio, BR, of 3.87 $\pm$ 0.05%. The reconstruction strategy which has been employed for the extraction of the D^0 meson signal is the same as the strategy used to compute the differential production cross section for D^0 mesons [45]; see section 2.2.1 for the results. The main features of the reconstruction strategy are presented in the following.

If all possible pairs of kaons and pions are considered as candidates for D^0 mesons, the result is a very low signal over background, S/B $\sim 10^{-6}$ [89]. Hence, in order to increase signal over combinatorial background it is of vital importance to add constraints on the reconstructed tracks and candidates based on typical topo-

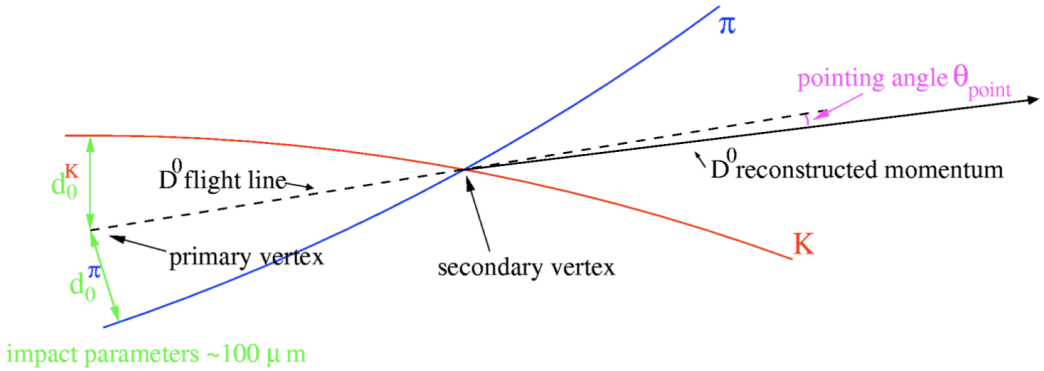

Figure 4.1: Decay topology of $D^0 \to K\pi$. The secondary vertex is separated from the primary vertex [89].

logical and geometrical properties characterizing signal tracks and reconstructed vertices. The ITS detector provides a resolution in the xy plane in the order of a few tens of μm on the track position at the collision vertex, also referred to as the primary vertex. This makes it possible to resolve the vertex of the D^0 meson decay, or secondary vertex, from the primary vertex. Thus, D^0 meson candidates are selected based on displaced vertices and topological cuts on tracks corresponding to daughter particles. The combinatorial background is further suppressed using particle identification (PID) for the daughters. The raw signal yield can then be extracted from the invariant mass of the decay daughters.

4.1.1 Secondary vertex reconstruction and topological cuts

The cut values have been tuned to optimize the statistical significance of the signal:

$$\mathcal{S} = \frac{S}{\sqrt{S+B}} \tag{4.1}$$

where $\mathcal{S}$ is the significance, S the signal and B the combinatorial background. The signal and background are extracted from the invariant mass distribution.

Figure 4.1 shows an illustration of a $D^0 \to K\pi$ decay topology. The D^0 meson is produced at the primary vertex and will travel for a certain length before decaying at the secondary vertex. Secondary vertices of D^0 meson candidates are reconstructed using tracks that pass a set of track cuts. All tracks are required to have a pseudorapidity smaller than 0.8 ($|\eta| < 0.8$), transverse momentum over 0.3 GeV/c, have at least 70 associated space points in the TPC detector, with $\chi^2/ndf < 4$, and at least one hit in either of the two first layers of the ITS detector. The fitting algorithm of the track is required to have TPC and ITS included in the refitting

p_T (GeV/c)/variable	[2,3]	[3,4]	[4,6]	[6,8]	[8,12]	[12,16]
$\|\cos(\theta^*)\|$ <	0.8	0.8	0.8	0.8	0.9	1.0
p_T (K,π) > [GeV/c]	0.7	0.7	0.7	0.7	0.7	0.7
$d_0^{K,\pi}$ < [cm]	0.1	0.1	0.1	0.1	0.1	0.1
$d_0^K \mathrm{x} d_0^\pi$ < [cm^2]	-0.15	-0.08	-0.08	-0.08/-0.07	-0.05	0
$\cos(\theta_{point})$ >	0.85	0.85	0.85	0.85	0.85	0.85
DCA < [cm]	0.03	0.03	0.03	0.03	0.03	0.03

Table 4.1: The various topological cuts used for the selection of D^0 meson candidates, and the values of the cuts in different p_T intervals. The cut value for $d_0^K \mathrm{x} d_0^\pi$ is different for p_T range 6-7 GeV/c (-0.08 cm^2) and 7-8 GeV/c (-0.07 cm^2).

procedure. The reconstructed secondary vertex are required to have a minimum displacement 100 μm from the primary vertex and a maximum Distance of Closest Approach (DCA) between the two tracks of 300 μm.

The two decay candidate tracks are further selected requiring $p_T > 0.7$ GeV/c. The figure also indicates the impact parameter of the daughter tracks, d_0^K and d_0^π, and the pointing angle, $\theta_{pointing}$, defined as the angle between the momentum of the D^0 meson reconstructed from the daughter particles, and the flight line. The flight line is defined by the primary and secondary vertices. The product of the impact parameters of the daughter tracks, $d_0^K \mathrm{x} d_0^\pi$, together with the cosine of the pointing angle are the most powerful cut variables for the signal extraction. A well-displaced $D^0 \to K\pi$ topology is characterized by large and opposite-signed values of the impact parameter of the decay tracks, and also small values of the pointing angle. Other cut variables include $|cos\theta^*|$, where θ^* is the angle between the kaon momentum in the D^0 rest frame and the boost direction. The background candidates will typically have large values of $cos\theta^*$, and this cut will reduce the contamination of background candidates that do not represent two-body decays.

Table 4.1 contains a list of all the cut variables that are used for the selection of D^0 meson candidates in this thesis. The cut variables are p_T dependent, and the variables are listed for all p_T intervals used in this thesis.

4.1.2 Particle identification of decay daughters

Particle identification of kaons and pions are used to enhance the signal over combinatorial background. Kaons and pions are identified via the specific energy loss in the TPC and via time-of-flight measured by the TOF detector, see section 3.3. For both detectors, a cut is applied to tracks in terms of units of the resolution of the difference between the measured and expected signals (nσ cut).

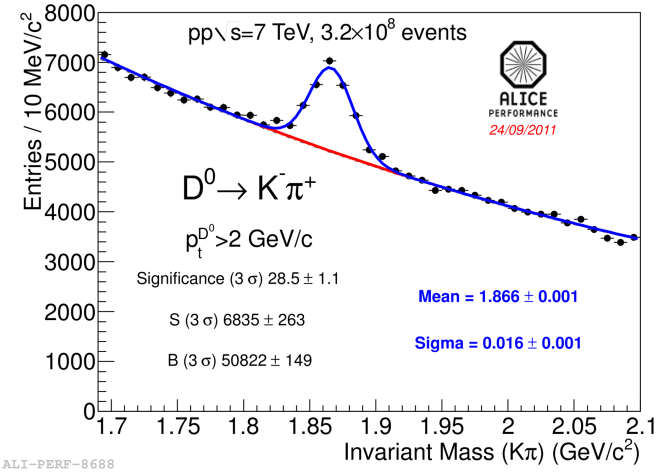

Figure 4.2: Invariant mass plot of the D^0 daughter candidates. This plot is for the momentum range of D^0 candidate above 2 GeV/c.

More specifically, in the TPC detector, a 2σ cut was applied to identify both kaons and pions. In addition, tracks with 2-3σ are kept as non-identified and both the kaon and pion mass hypothesis are assigned to the track. The pion and kaon expectation for the energy loss in the TPC becomes closer for the momentum range 0.6-0.8 GeV/c, and in this region the cut is reduced to 1σ. For the whole momentum range, the track is discarded as kaon and pion if the energy loss is greater than 3σ. When the TOF signal is present, a 3σ cut is applied to select kaons.

It has been shown that the PID strategy preserves close to 100% of the D^0 meson signal while reducing the combinatorial background by a factor of 2-3 in the low-p_T regions [45].

4.1.3 Signal extraction using the invariant mass analysis

An invariant mass plot is calculated using information from the reconstructed daughters of the D^0 meson. A typical invariant mass spectrum can be seen in figure 4.2 for the momentum of the D^0 meson above 2 GeV/c. The raw signal yields are extracted in different p_T intervals by a fit to the invariant mass distribution. The fitting function consists of a Gaussian term, describing the signal region, and an exponential term for the background. Table 4.2 shows the extracted number of D^0 mesons for each p_T range used in this thesis, together with the extracted mean, sigma and significance of the signal peak. These will be used later for the correlation analysis.

p_T interval [GeV/c]	Signal	Significance	μ	σ
2-5	4774 ± 310	16.7 ± 1.1	1.867 ±0.001	0.013 ± 0.001
5-8	1792 ± 93	21.4 ± 1.0	1.866 ± 0.001	0.018 ± 0.001
8-16	682 ± 60	14.3 ±1.1	1.869 ±0.002	0.026 ± 0.002

Table 4.2: Number of extracted D^0 mesons found in the p_T ranges used in this thesis, together with the mean (μ), sigma (σ) and significance of the signal peak.

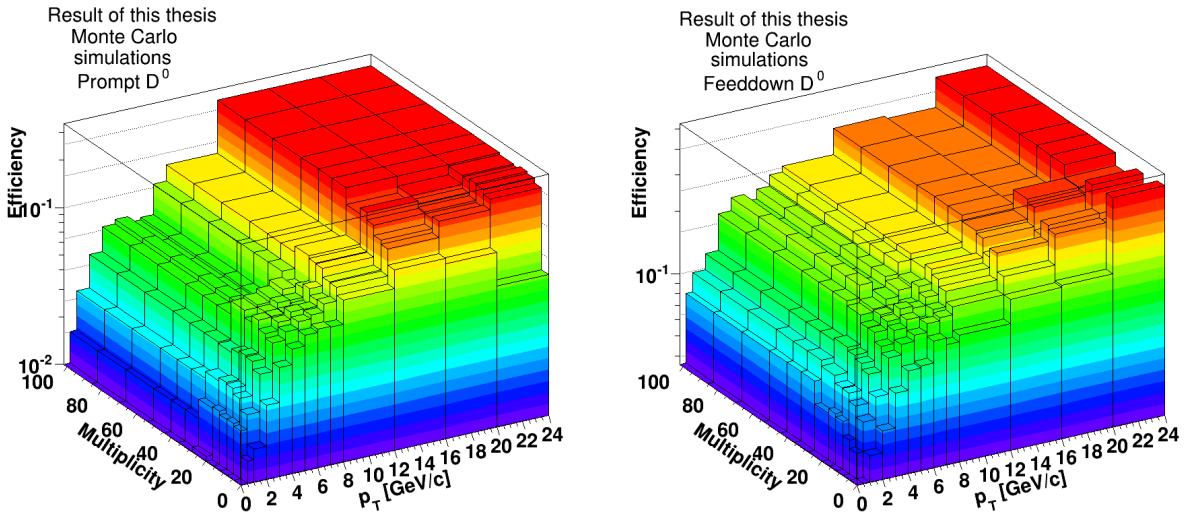

Figure 4.3: Reconstruction efficiency versus p_T and multiplicity for prompt D^0 mesons (left) and feed-down D^0 mesons (right) for p-p collisions.

4.1.4 Efficiency of D^0 mesons

The reconstruction efficiency has been evaluated separately for D^0 mesons from charm (prompt D^0 mesons) and D^0 mesons from bottom (feed-down D^0 mesons). A bottom and charm enhanced Monte Carlo sample has been used to compute the reconstruction efficiency, and then corrected for detector inhomogeneities and acceptance using a minimum bias Monte Carlo sample. The efficiency has been evaluated as a function of both p_T and multiplicity, see figure 4.3. Figure 4.4 shows the efficiency versus p_T, where the efficiency for prompt D^0 mesons is shown both with and without PID applied to the daughter tracks. This illustrates that the PID selection do not reduce the efficiency of the signal. The efficiency for feed-down D^0 mesons are shown for comparison, showing higher efficiencies for D^0 mesons decaying from B mesons. At LHC energies a substantial fraction of D^0 mesons comes from the decay of B mesons, between 10-20%, depending on the p_T interval [45]. B mesons have a decay length of $c\tau \sim$ 460-490 μm, and reconstructed feed-

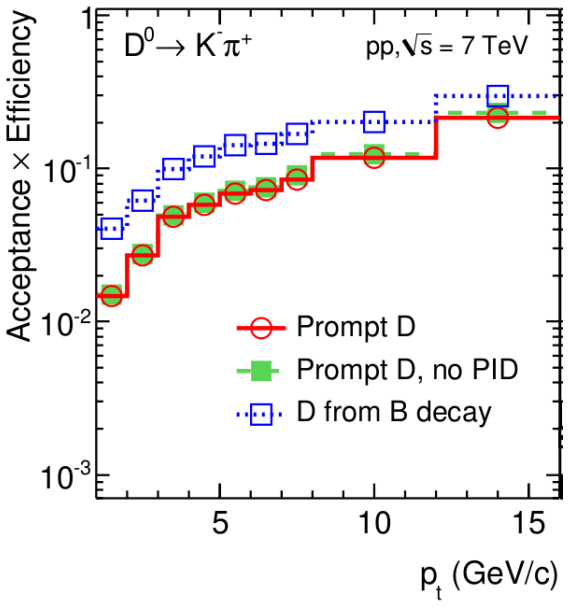

Figure 4.4: Reconstruction efficiency for prompt D^0 mesons (open, red markers), prompt D^0 mesons with no PID (green markers) and feed-down D^0 mesons (open, blue markers) for p-p collisions. This illustrates that the PID selection preserves the D^0 signal [45].

down D^0 mesons are on average well displaced from the primary vertex. Thus, the selection enhances the contribution of D^0 mesons decaying from B mesons with up to 15% to the raw yield.

4.2 Electron selection

The selection strategy of electrons in this thesis is based on the same strategy as employed for the measurement of electrons from semi-leptonic heavy-flavour hadron decays with the ALICE experiment [46], see section 2.2.1. The selection strategy ensures a very high purity of electrons, but with a compromise of efficiency. There are three main parts of the electron selection, and these will be explained in the following:

- Quality cuts on track level
- Particle identification (PID) to further reduce contamination of hadrons
- Suppression of background electrons not coming from heavy-flavour decays by using a cut on the invariant mass of electron pairs.

Cut	Cut-values
TPC clusters	120
TPC clusters for PID	80
ITS clusters	3,4
SPD requirement	hit in first layer (kFirst), hit in any of the two layers (kAny)
$\|\eta\|$	0.8
p_T	0.3-10 GeV/c
DCAr	1
DCAz	2
TOF-matching	Yes ($p_T < 2$ GeV/c)
TPC refit	Yes
ITS refit	Yes

Table 4.3: List of quality track cuts.

4.2.1 Track selection

The first part of the electron selection are the quality cuts on track level. This includes a cut on the number of ITS clusters per track, together with a cut on the number of TPC clusters per track. The cut on the number of TPC clusters per track is a relatively strict cut, 120 clusters per track out of 159 possible, but it has been verified that the electrons have in general more clusters per track than other particles. As a consequence, by requiring a high number of TPC clusters the fraction of electrons over hadrons will increase. In addition there is a cut on the number of TPC clusters used to calculate the specific energy loss in the TPC. The requirement of hits in the layers of the SPD detector will reduce the contamination of conversion electrons, where the requirement of a hit in the first layer (kFirst) is more effective than a hit in either of the two first layers (kAny). A cut on the DCA (Distance of Closest Approach) in the xy plane (DCAr) and z direction (DCAz) will enhance the selection of particles produced in the collision. As the TOF detector is later used for PID, the quality cuts also include a requirement that the track has a hit in TOF (TOF matching) in order to exclude the TOF matching from the PID efficiency. In addition, the fitting algorithm of the track is required to have TPC and ITS included in the refitting procedure. A full list of the quality track cuts can be found in table 4.3.

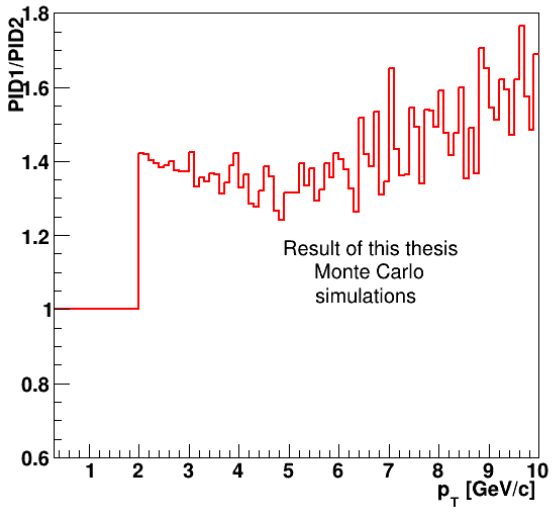

Figure 4.5: Ratio of p_T distributions for two different PID strategies, one using TPC and TOF PID for the entire p_T range (PID2) and the other using TOF only for $p_T < 2$ GeV/c (PID1). As the PID strategy is the same for $p_T < 2$ GeV/c, the ratio is 1 in this region. Above this limit, where only the TPC PID is employed, an increase in statistics $\sim 40\%$ is observed.

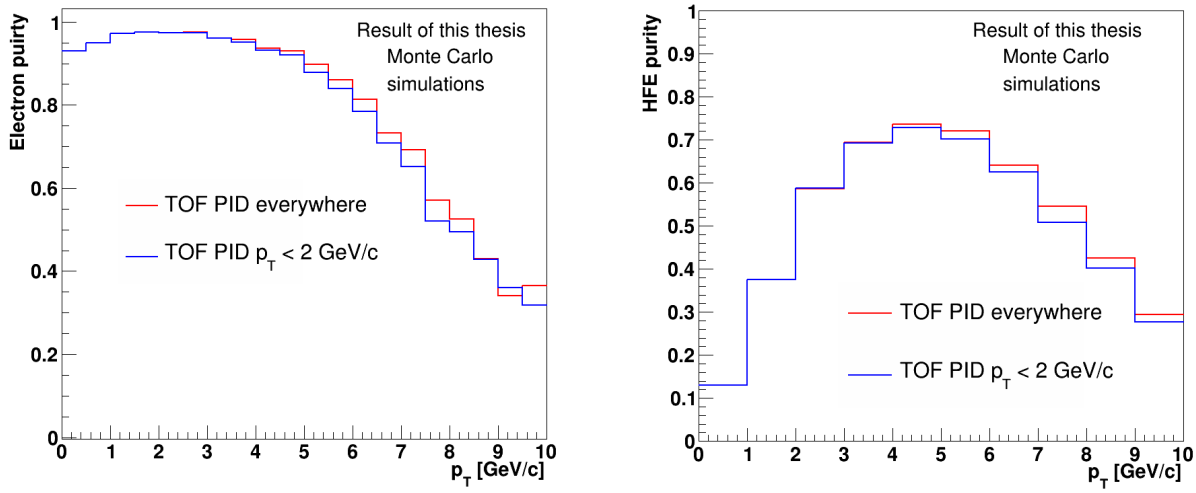

Figure 4.6: Electron (left) and HFE (right) purities for different PID strategies. This illustrates that although one gets $\sim 40\%$ increase in statistics by excluding TOF for $p_T > 2$ GeV/c, the electron and HFE purity is preserved. TPC PID is employed for the entire p_T region for all distributions.

4.2.2 Particle identification of electrons

As for the PID of the D^0 meson daughters, the PID strategy for the electrons relies on a combination of information from the TPC and TOF detectors. The track is selected if the measured particle velocity using the TOF detector is within 3σ of the expected electron time-of-flight hypothesis. This will reject charged kaons up to a transverse momentum of ~ 1.5 GeV/c, and protons up to a transverse momentum of ~ 3 GeV/c. The TPC detector is employed to further enhance the electron purity, where the candidates are required to be within -1 to 3 standard deviations of the expected electron energy loss. The lower value is set to -1 as the pion band is very close to the electron band in this region, see section 3.3.

Two different PID strategies have been considered. The first strategy is to use the combined TPC and TOF PID for the entire p_T-region. The second is to use the combination of the two detectors for PID up to transverse momentum of 2 GeV/c, and further use only TPC PID above 2 GeV/c. Figure 4.5 shows the ratio of the p_T distributions obtained with the two PID strategies. It illustrates that for p_T below 2 GeV/c, the statistics is the same, while above 2 GeV/c, the statistics increase by $\sim 40\%$. Also, while increasing the statistics, the electron signal is still preserved as can be seen while comparing the electron and HFE purity; see figure 4.6. The electron purity is defined as the ratio of the number of true electrons in the sample of selected candidates over all selected candidates, while the HFE purity is defined as the number of true HFE over all selected candidates.

4.2.3 Removal of non heavy-flavour electrons

After track cuts and the PID selection, there is a significant contribution from background electrons, also referred to as non heavy-flavour electrons (non-HFE). As the goal is to get a high purity HFE sample, the next step is to remove as many non-HFE as possible. The most important sources of background are:

- gamma conversion in the detector material
- Dalitz decay of π^0 and η mesons and other light neutral mesons
- di-electron decays from heavy quarkonia (especially J/Ψ)
- electrons from weak decays of kaons and di-electron decays of light vector mesons
- electrons originating from partonic hard scattering processes (Drell-Yan processes and prompt photon production).

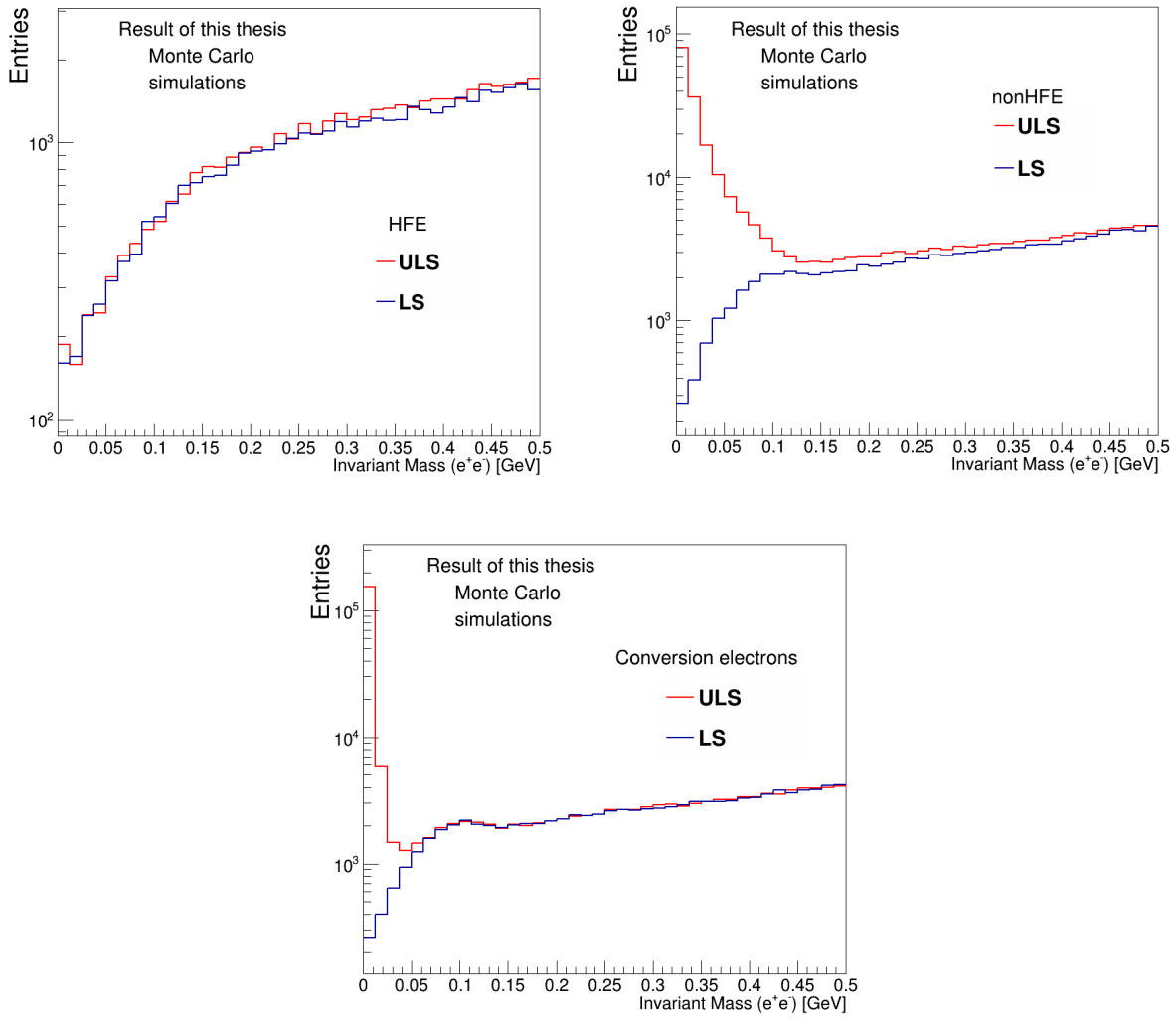

Figure 4.7: The invariant mass of electron pairs for unlike-sign and like-sign pairs for different electron sources. Top left: HFE, top right: non-HFE (excluding conversion electrons) and bottom: electrons from gamma conversion.

Cut	Cut-values
TPC clusters	80
TPC refit	Yes
$\|\eta\|$	0.9
p_T	0.3-999 GeV/c
σ TPC PID	$\pm$ 3

Table 4.4: List of quality cuts for the partner electron used to reconstruct non-HFEs from Dalitz decay of neutral mesons and gamma conversion.

The most dominant background sources are the first two mentioned, the rest are negligible in comparison. The electrons decaying from Dalitz decay and gamma conversion have opposite charge, and the invariant mass of electron pairs from these background sources is very small. No such correlation exist for the HFE, and as a result, one way of removing these sources is to compute the invariant mass of electron pairs for like-signed and unlike-signed pairs. The unlike-sign pairs contain true non-HFEs as well as combinatorial background where the HFEs have been misidentified as non-HFEs. Figure 4.7 shows the invariant mass distributions for unlike-signed and like-signed pairs for identified HFE, non-HFE (excluding electrons from conversion) and conversion electrons. It can be seen that the unlike-signed distribution for non-HFE and conversions electrons show a peak for small invariant mass values of electron pairs, and it is also seen that no such peak can be observed in the invariant mass distributions from identified HFEs.

The invariant mass spectrum is computed as follows: Every electron candidate which is found with the mentioned quality track cuts and PID, is paired with partner electron candidates in the same event. The partner candidate is selected using less strict quality cuts, which are listed in table 4.4. If such a pair of electrons is found, then their invariant mass is computed. Figure 4.8 shows the invariant mass for unlike-sign and like-sign candidates, as computed on the full data-set from 2010. The effect of various invariant mass cuts has been studied for different sources of the selected electron candidates using a minimum bias Monte Carlo sample. Figure 4.9 illustrates the effect invariant mass cuts of 50, 100, and 150 MeV/c have on all electrons, non-HFE, HFE and hadrons, which have been misidentified as electrons. It is clearly shown that the non-HFEs are most heavily affected and that the cut removes around 40-60% of them, depending on the p_T region. The most effective one is the cut of 150 MeV/c. The invariant mass cut also removes some of the hadrons, especially at low p_T. The HFEs, on the other hand, are seen to be little affected by the cut, and over 90% of the HFEs survive the invariant mass cut, over 95% for p_T $>$ 1 GeV/c. As the different invariant mass cuts show little difference in terms of

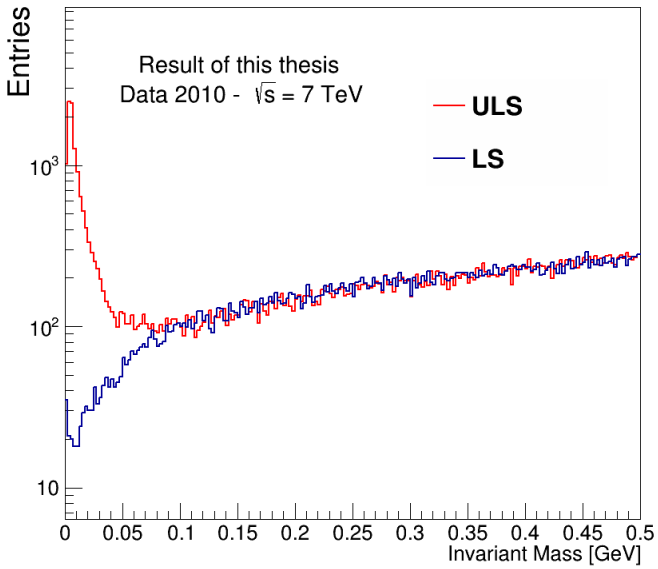

Figure 4.8: The invariant mass distribution of unlike-sign and like-sign electron pairs as computed on the full 2010 p-p data-set. The unlike-sign pairs contains mostly electrons coming from conversion of gamma and Dalitz decay of neutral mesons.

the impact of both the HFEs and non-HFEs, a cut of 150 MeV/c is chosen on the unlike-signed invariant mass distribution in order to cut away as many non-HFEs as possible. Figure 4.10 shows the comparison of the electron and HFE purity with and without applying the cut of 150 MeV/c on the invariant mass of electron pairs, and it is seen that the cut increases the HFE purity.

With the cut on the invariant mass of electron pairs one goes from what is referred to as an inclusive sample of electrons to a semi-inclusive one:

$$N_e^{semi-incl} = N_e^{incl} - N_e^{ULS}. \tag{4.2}$$

4.2.4 Efficiency of the electron selection

Figure 4.11 and 4.12 show the azimuthal angle, ϕ, and the pseudorapidity, η, distributions for the final selected electron candidates, and it can be seen that the distributions are not uniform, as would be expected if a perfect detector was present. The η distribution shows a clear structure, which is mainly present for transverse momentum lower than 2 GeV/c, and this is a result of the geometrical structures in the TOF detector. Looking at the distribution for electron candidates with $p_T > 2$ GeV/c, where the TOF detector is no longer applied for the PID selection and there

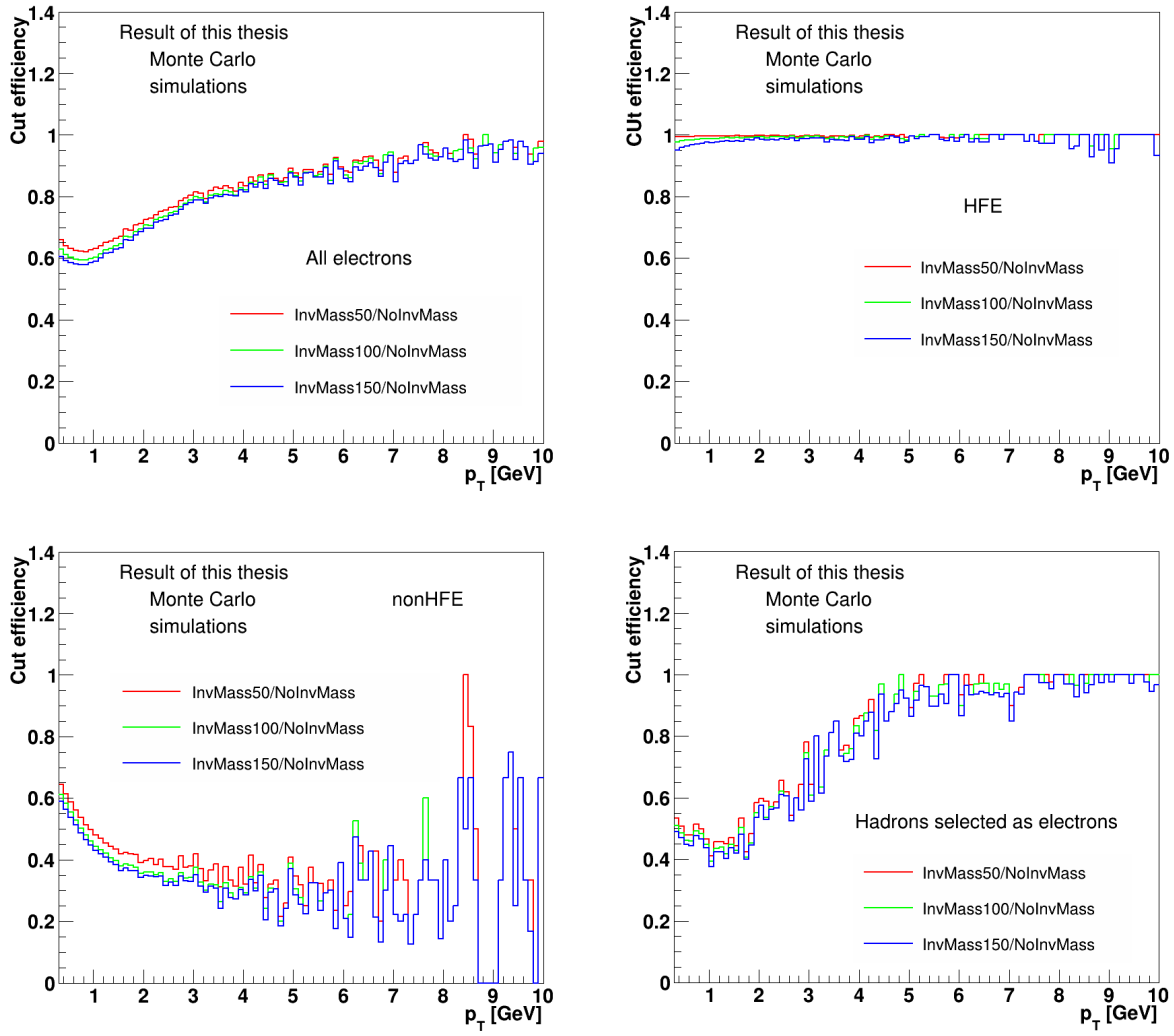

Figure 4.9: The ratio of the p_T distributions before and after various invariant mass cuts (50, 100 and 150 MeV/c), illustrating the effect the invariant mass cut has on different electron candidate sources, all electrons (top left), HFEs (top right) and non-HFEs (bottom left). The invariant mass of hadrons, which have been misidentified as electrons, has also been computed (bottom right). The invariant mass cuts preserves more than 90-95% of the HFE signal, while removing 40-60% of the non-HFEs.

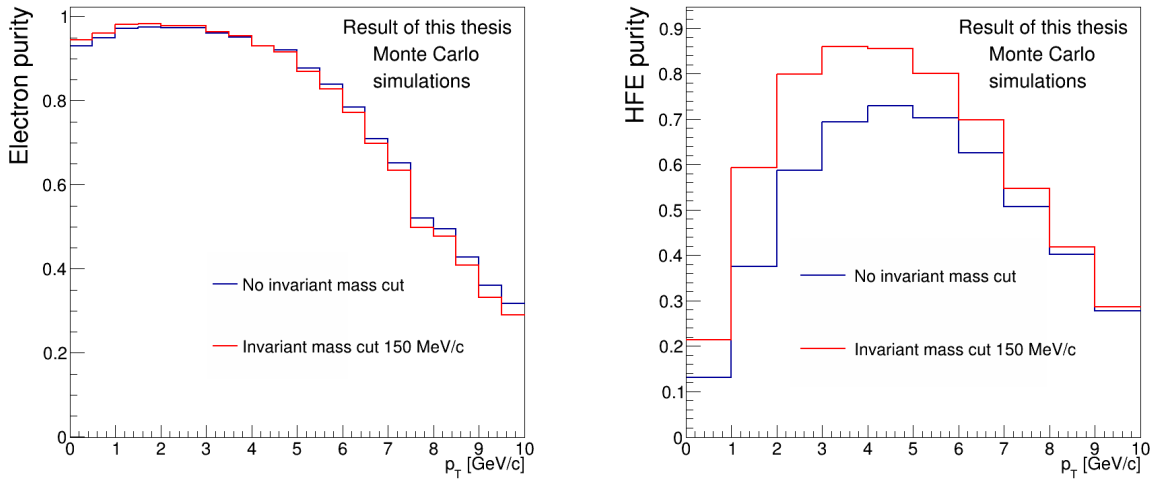

Figure 4.10: Comparison of the electron and HFE purity with and without the cut of 150 MeV/c on the invariant mass of unlike signed electron pairs. It is observed that the HFE purity is increased by applying the invariant mass cut.

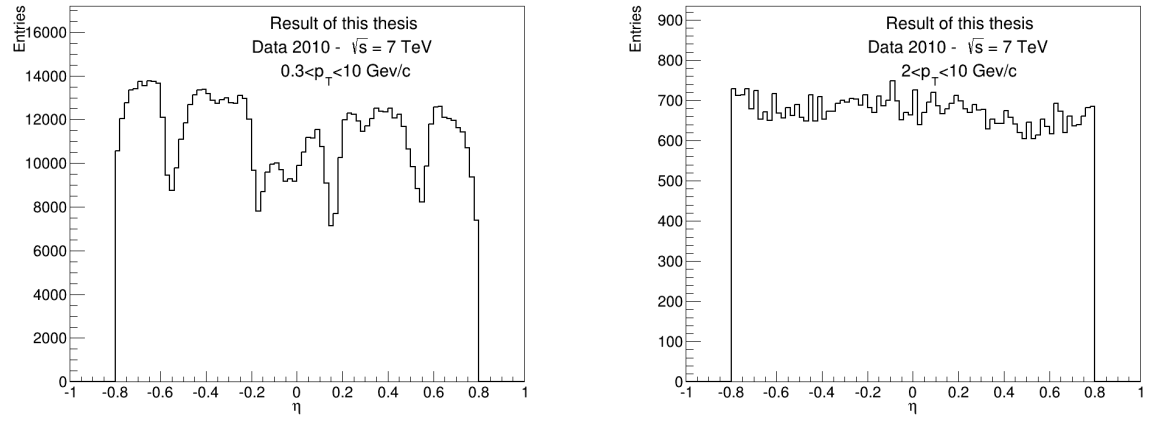

Figure 4.11: Electron pseudorapidity η distributions for two p_T regions, 0.3-10 GeV/c (left) and 2-10 GeV/c (right). A clear structure in the η distribution can be observed for the entire p_T region, which is caused by the TOF detector. When looking at the region where TOF is not required, above 2 GeV/c, the structure is observed to disappear.

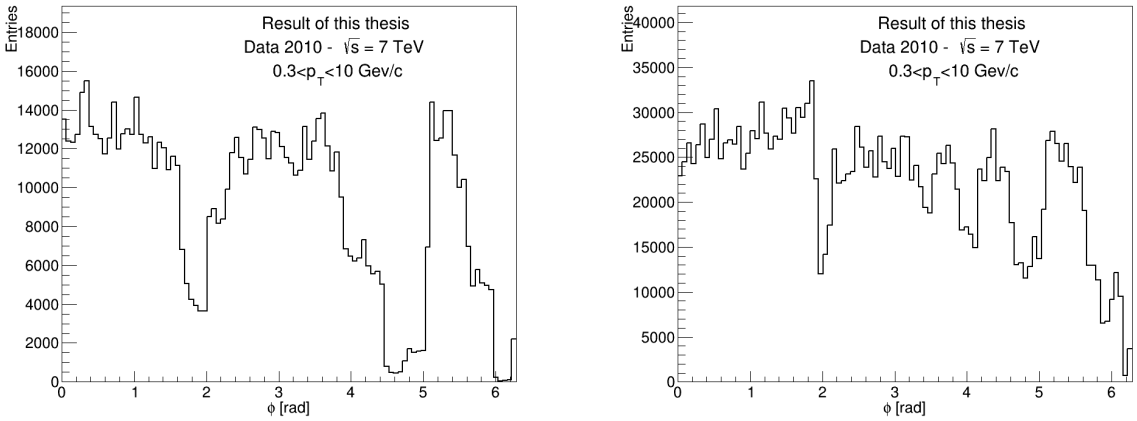

Figure 4.12: Electron ϕ distributions: Left, requiring 4 ITS clusters pr track and a hit in the first layer of the ITS detector (kFirst). Right, requiring 3 ITS clusters pr track and a hit in either of the two first layers of the ITS (kAny). The structures observed in the ϕ distributions are partially dominated by the first layer in the ITS detector, and they are not as prominent when requiring only a hit in any of the two first layers of the ITS detector.

is no requirement that the track has a hit in the TOF detector, the mentioned structure is no longer visible. The ϕ distribution also shows clear geometrical detector effects. Figure 4.12 compares the ϕ distribution when requiring kFirst and kAny. The structure observed is mainly governed by the first layer in the ITS, and thus using the less strict cut kAny, the structure is still there, but not as pronounced as for kFirst.

An efficiency map is created to correct for the inefficiency of the electron selection. A Monte Carlo sample which has been tuned to reproduce minimum bias events is used to evaluate the efficiency. It is computed as a ratio of electrons on the reconstructed level of the Monte Carlo simulation, over electrons on the generated level. The electrons on the generated level have not been transported through the detector, and thus illustrates the undistorted distributions. The work-flow of the selection of electrons on the reconstructed and generated level is illustrated in figure 4.13. For electrons on the generation level, only electrons in the right acceptance region are selected. This includes a cut on pseudorapidity, $|\eta| < 0.8$, together with a lower p_T cut of 0.3 GeV/c. Only particles produced in the collisions, thus excluding electrons from gamma conversion in the detector material, are selected for both the electrons on the generated and reconstructed level.

Especially the requirements in the SPD have been seen to be important while trying to find a compromise between HFE purity and efficiency. Three different

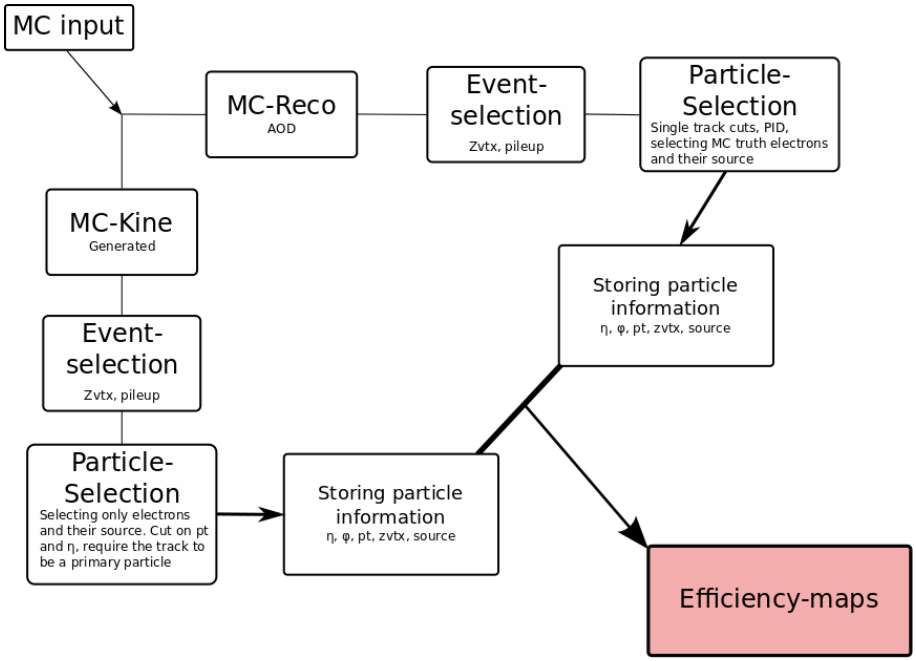

Figure 4.13: Overview of the electron efficiency calculation. The generated and corresponding reconstructed particles are treated separately, and the outputs are used to compute the efficiency.

requirements have been compared, namely the requirements kFirst and kAny. Figure 4.14 shows the efficiency of the electron selection for only the single track cuts, illustrating that the requirement kAny gives the highest efficiency. However, the selected sample with the kAny requirement will contain a high amount of electron pairs from gamma conversion created by the ITS detector, and this is greatly reduced by requiring a hit in the first ITS layer. The figure also compares a track cut of 3 or 4 ITS clusters per track. It is observed that this cut has minimal impact on the efficiency, both for the requirement kFirst and kAny.

Figure 4.15 shows the electron and HFE purity for two different electron selections, one using kFirst and 4 ITS clusters per track and the other kAny with 3 ITS clusters per track. The first gives a higher purity for both electrons and especially HFE. Thus, kFirst will give the highest HFE purity, but has the disadvantage of lower efficiency. Nevertheless, the requirement of kFirst has been chosen as the HFE purity is higher.

The PID strategy that has been employed ensures a 85% PID efficiency, as can be seen in figure 4.16. The PID efficiency is defined as the ratio of the number of true electrons in the sample before and after applying the PID. The PID efficiency is observed to be rather uniform for p_T and η. The comparison of different track

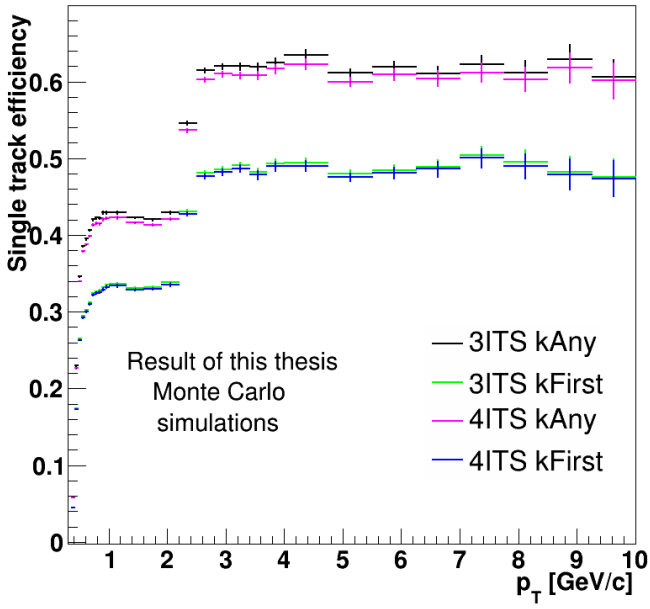

Figure 4.14: The efficiency versus p_T for selected electrons after only including single track cuts, for different configurations of the ITS detector. The most relevant cut is the requirement in the SPD detector, where the requirement of a hit in the first pixel layer of the ITS (kFirst) leads to the lowest electron efficiency. The efficiency will increase when only requiring a hit in either of the two first layers (kAny). The plot also compares 3 and 4 ITS clusters per track, and it is observed that the cut on the number of ITS clusters per track have little impact on the efficiency. The jump for $p_T > 2$ GeV/c is a result of the TOF PID configuration.

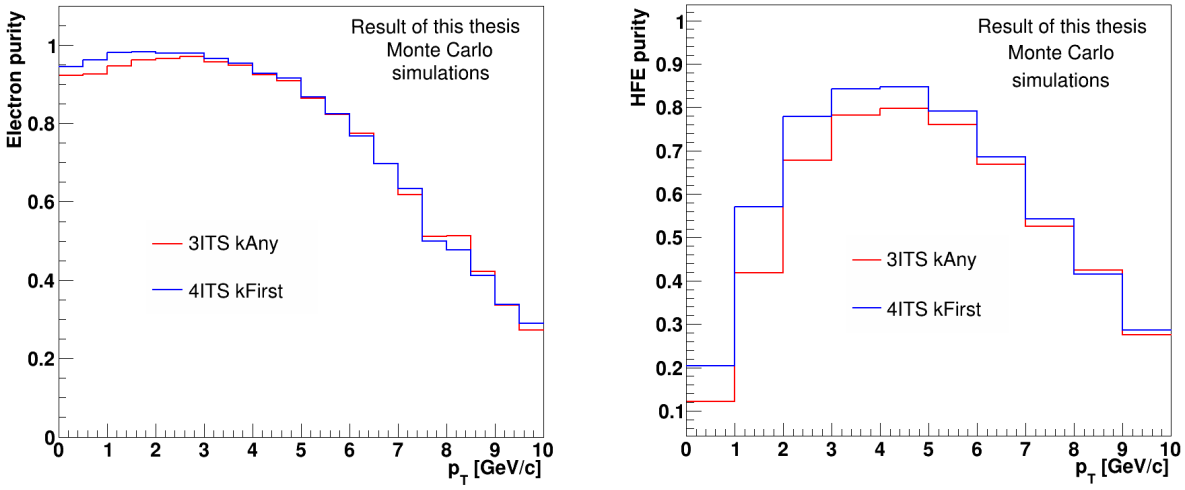

Figure 4.15: Electron (left) and HFE (right) purity for two settings in the track selection, namely the requirement of a hit in the first layer of ITS (kFirst) together with requirement of 4 ITS clusters (blue) compared with the requirement of a hit in one of the two first layers of the ITS (kAny) along with the requirement of 3 ITS clusters per track (red). Loose cuts give a lower electron purity and heavy-flavour electron purity, but higher efficiency.

cuts in the ITS detector is shown, illustrating that the PID is unaffected by the different ITS configurations which have been applied.

The final result is an efficiency map in p_T, Z-vertex and η dimensions. The efficiency as a function of p_T and η (right) is shown in figure 4.17. It can be seen that there are fluctuations at high p_T, but as the hadron contamination is increasing significantly for $p_T >$ 5-6 GeV/c, this region is not used further in the analysis. If so, there should be applied some re-binning of the distribution before applying the efficiency map. The figure also show the efficiency as a function of only p_T (left).

Correction for the efficiency of the invariant mass cut

The invariant mass cut has to be adapted in terms of correcting for the efficiency of the cut. Instead of correcting for the fact that the invariant mass cut will cut away electrons, it should correct for the fact that the cut is not removing all non-HFEs. Such a method has already been implemented for the azimuthal angular correlation measurement of HFEs with hadrons [75], and is described in detail in the analysis note of that analysis [90]. The method relies on estimating the remaining non-HFE component and further subtracting this contribution on a statistical basis. This is performed by constructing the correlation distribution of electrons with hadrons,

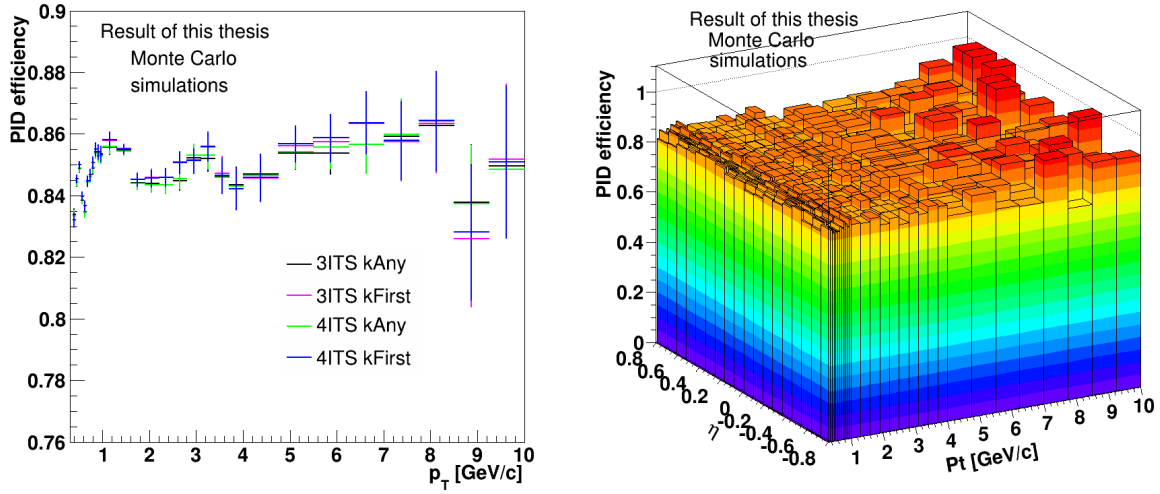

Figure 4.16: The PID efficiency versus p_T (left) is compared for different track cuts in the ITS detector and illustrates that the PID performance is stable almost regardless of the track selection in the ITS. The PID efficiency versus p_T and η (right) shows no significant dependence on either of the variables.

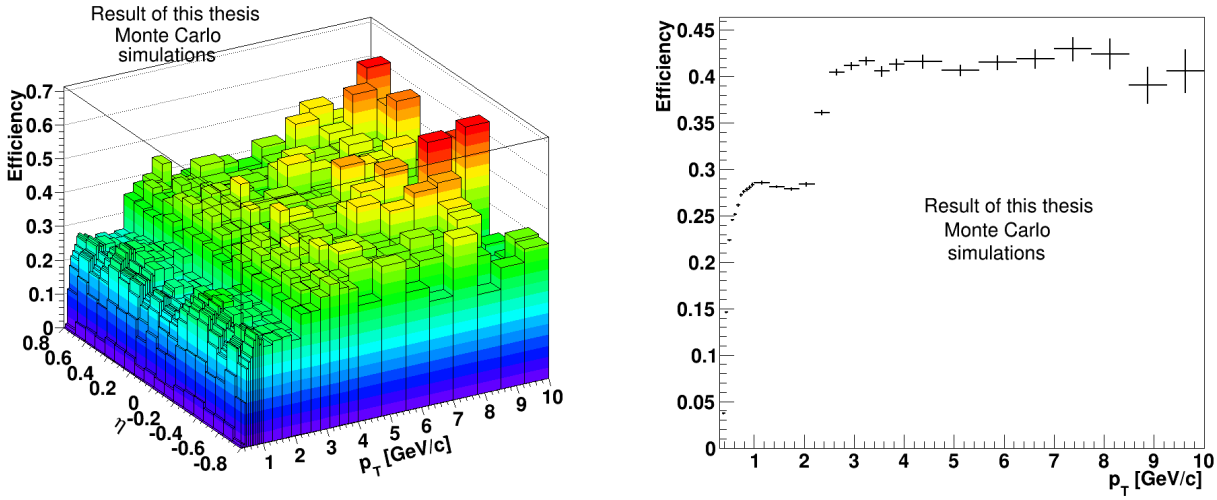

Figure 4.17: Electron efficiencies, including single track cuts and PID, versus p_T and η (left) and versus p_T only (right). The efficiency is seen to have a p_T dependence especially at low p_T. The jump for $p_T > 2$ GeV/c is a result of removing the requirement of the TOF detector.

where the electrons have been removed by the cut on the unlike-signed invariant mass distribution. The correlation distribution is scaled by the efficiency of the non-identified non-HFE, before it is subtracted from the correlation distribution with the semi-inclusive electrons.

This method is currently not feasible to apply for the analysis in this thesis. By investigating figure 4.8, it can be seen that the number of electrons in the ULS distribution below 150 MeV/c is relatively low. As this method relies on constructing the correlation distribution of D^0 mesons with these electrons, the number of pairs will be very low. This will in turn introduce large statistical error with the subtraction.

Chapter 5

Azimuthal correlation of D^0-mesons with heavy-flavour electrons

5.1 Analysis strategy

This chapter will focus on the correlation analysis, more specifically the various steps of the analysis. A substantial part of the work for this thesis has been the construction of the analysis software.

The most time consuming parts of the analysis is performed on the grid. This is a network of computer clusters spread out across the world. After the data has been collected by the Data Acquisition in ALICE, the data is transferred to permanent storage. The ALICE grid interface AliEn both gives access to the recorded data and makes it easy to process large amounts of data. This allows for a fast evaluation of the available data, and has been extensively used for the analysis in this thesis to collect the necessary data. The various steps of the analysis is summarized in the following, and will also be elaborated in the next sections:

- Identify D^0 meson and electron candidates. Store information on both the electrons and D^0 meson candidates, and also information on the correlated pairs.
- Apply corrections for both the D^0 meson and electron candidate efficiency.
- Perform the two steps above for mixed events (ME), where D^0 meson candidates are paired with electron candidates from other events.
- Separate the correlated D^0 meson-electron pairs in $\Delta\phi$ and $\Delta\eta$ based on the calculated invariant mass of the D^0 meson.

- Use the correlation distribution for mixed events in $\Delta\eta$ and $\Delta\phi$ to correct for acceptance effects.
- Project out $\Delta\phi$ from the correlation distribution in ($\Delta\eta$,$\Delta\phi$), and subtract the background contribution from fake D^0 meson candidates.
- Plot the final corrected $\Delta\phi$ distribution.
- Divide by the number of D^0 mesons, also referred to as the number of triggers, to get the yield on a per trigger level.
- Extract information on the near- and away-side of the distribution by applying a fit to the $\Delta\phi$ distribution.

5.2 Raw distributions

The first step of the analysis is to identify D^0 meson and heavy-flavour electron candidates. See chapter 4 for details on the selection strategy for both particles. If a D^0 meson candidate and an electron candidate both are found in the Same Event (SE), the relative angle in ϕ, $\Delta\phi = \phi_1 - \phi_2$, and the difference in pseudorapidity, $\Delta\eta = \eta_1 - \eta_2$, between them is calculated and stored.

The D^0 meson candidates are only selected if they have a calculated invariant mass within $\pm 3\sigma$ of the signal peak μ, which is extracted using a Gaussian fit to the invariant mass distribution as described in the previous chapter. However, there is a certain amount of combinatorial background (fake D^0 mesons) in this sample which has to be removed on a statistical basis, using the correlation distributions. The side-band subtraction method is used for this purpose, and the method will be described in more detail later in this chapter. As a result, the candidate pairs will be divided into several regions which are based on the calculated invariant mass of the D^0 meson, see also figure 5.1:

- Peak region, defined as $\mu \pm 3\sigma$. It is marked as yellow and red and can be divided into two regions:
  - Signal region (S), which is the region between the fit of the peak and the background, marked as the yellow region.
  - Background region (B), which is the region below the fit to the background of the invariant mass peak, marked as the red region.
- Side-band 1 (SB1), defined as the region between -9σ < μ <-4σ, marked with the colour green.

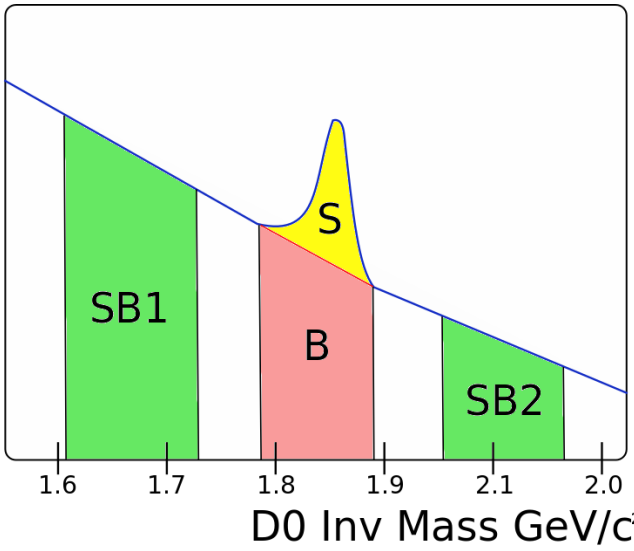

Figure 5.1: Side-bands and peak region in the invariant mass distribution. Peak region is defined as $\mu \pm 3\sigma$, while the side-band regions are defined as $\mu \pm$ 4-9σ.

- Side-band 2 (SB2), defined as the region between $4\sigma < \mu < 9\sigma$, marked with the colour green.

The raw yield versus $\Delta\phi$ for the peak region and the side-band regions are shown in figure 5.2. The selected D^0 meson candidates have a transverse momentum between 2 and 5 GeV/c, while the electron candidates have a p_T between 1 and 4 GeV/c. The choice of electron p_T is based on the HFE purity of the selected electrons. Below 1 GeV/c, most of the selected electrons is non-HFEs, thus only electrons above 1 GeV/c are selected for the azimuthal angular correlation. The hadron contamination starts to increase for p_T above 4-5 GeV/c, thus the upper limit is set to 4 GeV/c. A comparison of the azimuthal angular correlation distribution for different p_T intervals for the electron selection is shown later in this chapter.

5.3 Acceptance corrections

The correlated distribution will experience effects arising from the limited acceptance of the detector and the non-uniform azimuthal distribution of tracks. One way to correct for this, is to use the event mixing technique, where D^0 meson candidates in one event are correlated with electron candidates from another event. It is important to correlate pairs in events with similar event characteristics. This is performed by constructing a pool where the pool is filled and categorized based on

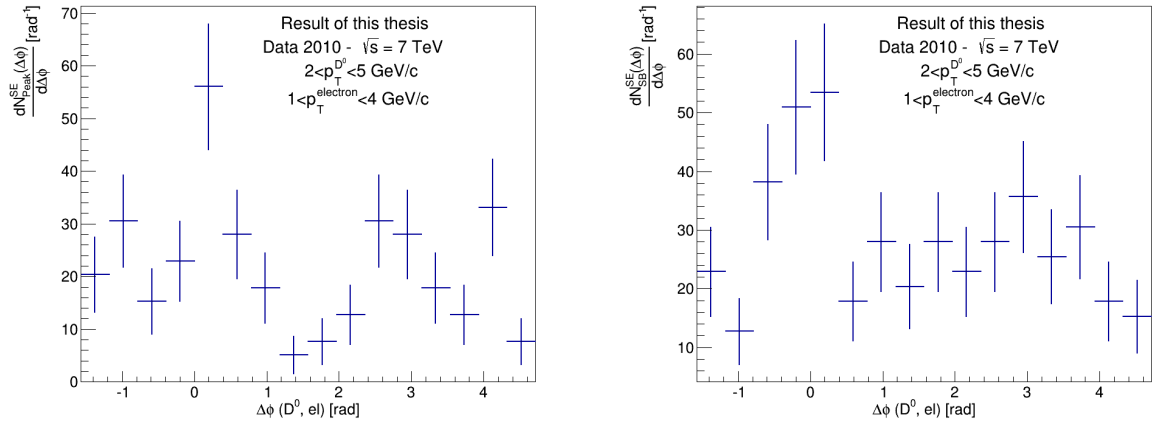

Figure 5.2: The $\Delta\phi$ distributions for the peak region (left) and the combined side-band regions (right). The transverse momentum region is 1-4 GeV/c for electrons, and 2-5 GeV/c the D^0 mesons.

Pool settings	Values
Zvertex bins [cm]	-10,-5,-2.5,2.5,5,10
Multiplicity bins	0,20,40,60,80,500
Min nr of tracks in pool	100
Min nr of events in pool	8

Table 5.1: List of settings for the event pool. Every event is categorized based on the Z-position of the vertex and the multiplicity.

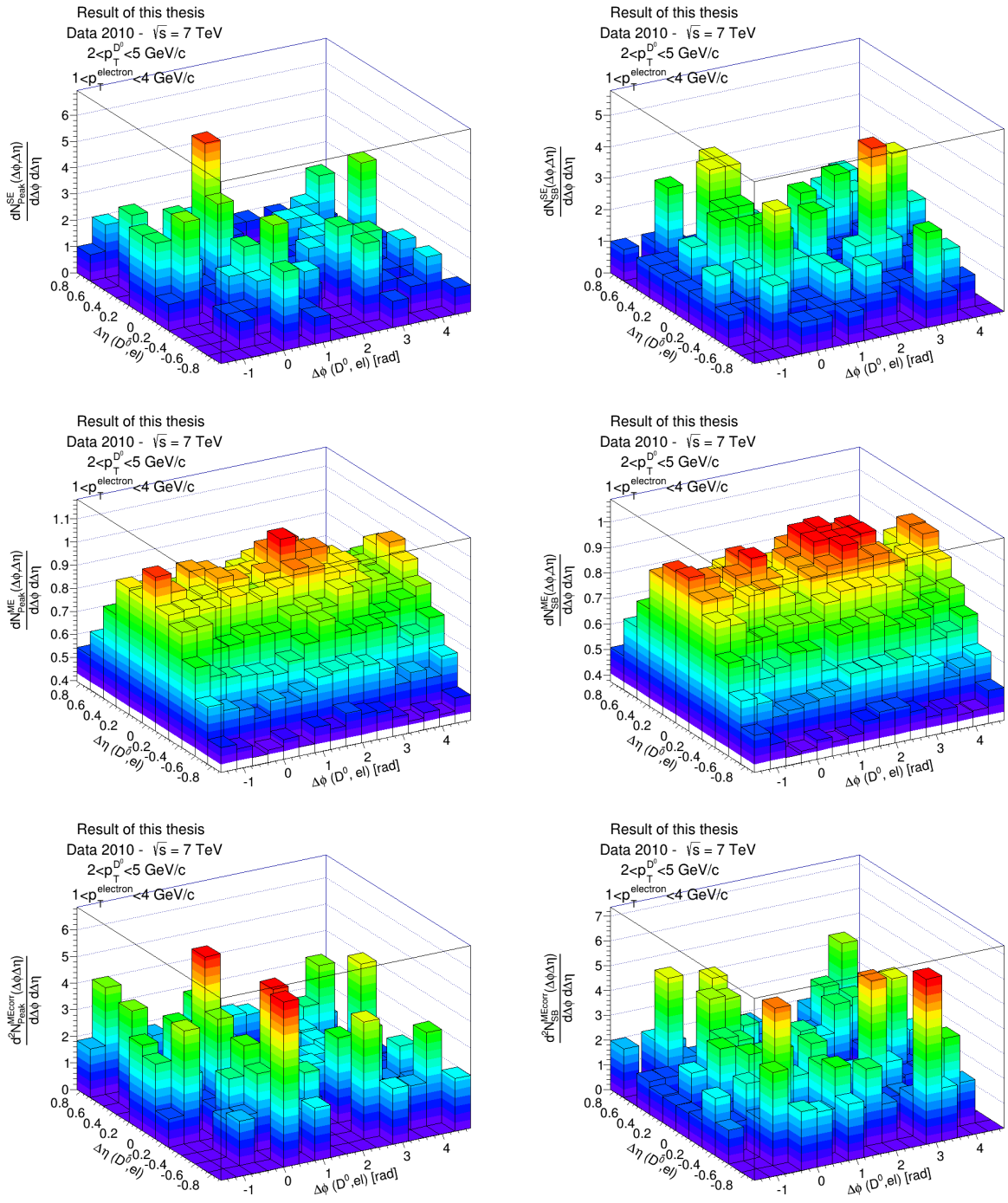

Figure 5.3: ($\Delta\phi$,$\Delta\eta$) for peak (left column) and side-band regions (right column) for single events (top row), mixed events (middle row) and single events corrected for event mixing (bottom row). The plots for mixed events have been normalized to unity in the bin ($\Delta\eta$,$\Delta\phi$) = (0,0). The plots show the p_T interval 2-5 GeV/c for the D^0 mesons candidates, and 1-4 GeV/c for the electron candidates. As one can clearly see in these plots, the statistics is very sparse.

event properties (z coordinate of the reconstructed vertex and the number of tracks per event, or multiplicity). The settings for the event pool is listed in table 5.1. Before the event mixing starts, there has to be enough tracks and events in the respective pool bin. In an ideal setting, where there are no detector effects other than limited acceptance in η of the detector, one expects a flat distribution in $\Delta\phi$ and a triangular shape in $\Delta\eta$.

The event mixing corrections are applied after all events have been collected. The ($\Delta\eta$,$\Delta\phi$) distributions for the correlated candidate pairs for Single Events (SE), and the same distributions for Mixed Events (ME), for both the side-bands and the peak region, are shown in figure 5.3. The distribution for the mixed events is normalized to unity in the bin ($\Delta\phi$,$\Delta\eta$)=(0,0). This is a strategy adopted from hadron-hadron correlations, which relies on the fact that the correlated pair of hadrons is pointing to the same location of the detector and should thus experience the same detector effects. This technique is not necessarily fully applicable for D^0 mesons, as they are reconstructed from two particles. This strategy is adopted as a first approximation, as the region ($\Delta\phi$,$\Delta\eta$)=(0,0) has the maximum efficiency for the pairs.

To get the ME corrected spectra, $\frac{dN^{corr}(\Delta\eta,\Delta\phi)}{d\Delta\eta d\Delta\phi}$, the SE distribution is divided by the normalized ME distribution:

$$\frac{dN^{MEcorr}(\Delta\eta,\Delta\phi)}{d\Delta\eta d\Delta\phi} = \frac{\frac{dN^{SE}(\Delta\eta,\Delta\phi)}{d\Delta\eta d\Delta\phi}}{\frac{dN^{ME}(\Delta\eta,\Delta\phi)}{d\Delta\eta d\Delta\phi}} \frac{dN^{ME}(0,0)}{d\Delta\eta d\Delta\phi} \tag{5.1}$$

The corrected distributions for both the sideband- and peak-region can also be seen in the bottom plots in figure 5.3.

One of the major challenges with this analysis becomes very apparent when investigating the correlation distribution as a function of both $\Delta\phi$ and $\Delta\eta$. The limited available statistics makes it very difficult to see any shape in the ($\Delta\eta$,$\Delta\phi$) distribution. As a result, in the following the correlation distribution are only evaluated in $\Delta\phi$. The projection of the side-bands and peak region after event mixing corrections are shown in figure 5.4 and these plots form the basis for the acceptance corrections. The plots are shown for the transverse momentum range 2-5 GeV/c for the D^0 meson candidates, and 1-4 GeV/c for the electron candidates.

5.4 Side-band subtraction

As mentioned already, a substantial part of the particles passing the selection cuts for D^0 meson particles, are background and have to be removed on a statistical basis. The side-band subtraction method is used to remove the background in the peak region. Candidates which are found in the side-bands of the invariant mass

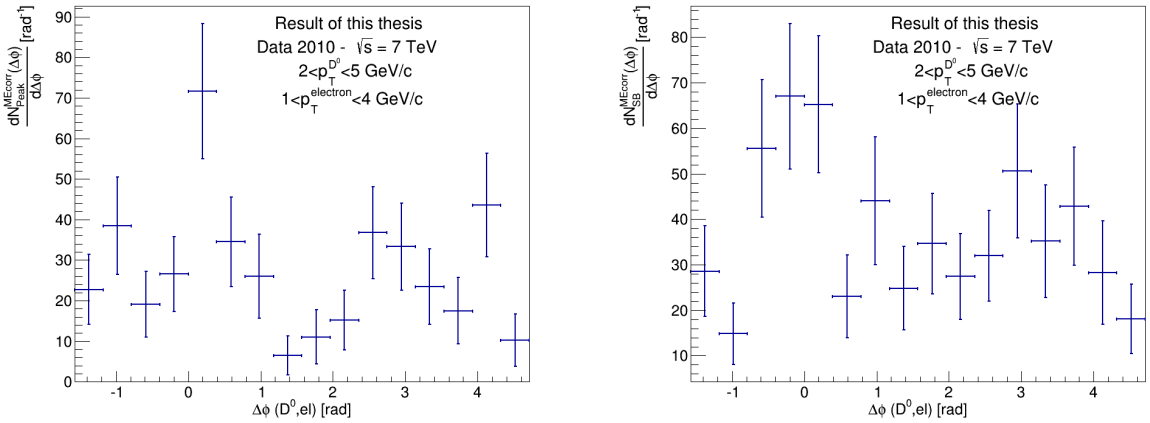

Figure 5.4: The $\Delta\phi$ distributions for the peak region (left) and the combined side-band regions (right) after event mixing corrections. Transverse momentum for electron 1-4 GeV/c, and 2-5 GeV/c for the D^0 meson candidates.

distribution are assumed to be fake D^0 mesons, and they are used to characterize the background in the peak region. The $\Delta\phi$ distribution obtained from the side-band region is normalized with respect to the background distribution in the signal region (region B in figure 5.1). The normalization factor, w, is calculated as the integral of the following regions in the invariant mass distribution:

$$weight\ \mathrm{w} = \frac{B}{(SB1 + SB2)} \tag{5.2}$$

The normalized distribution from the side-bands is subsequently subtracted from the distribution in the peak region, which only leave signal D^0 mesons, or the yellow area of the curve in figure 5.1. The side-band subtracted $\Delta\phi$ distributions are shown in figure 5.5 for various transverse momentum regions for the D^0 meson candidates, namely 2-5 GeV/c, 5-8 GeV/c, 8-16 GeV/c and also the integrated D^0 transverse momentum range 2-16 GeV/c. To reduce the statistical challenges, only the latter will be used in the further evaluation.

5.5 Corrections for D^0 meson and electron efficiency

The corrections for the efficiencies for both the D^0 mesons and the electrons are applied by adding a weight to the correlated pair, before performing the mixed event corrections and the side-band subtraction method. The weight is computed as the product of the efficiencies of the D^0 meson and the electron, see sections 4.1.4

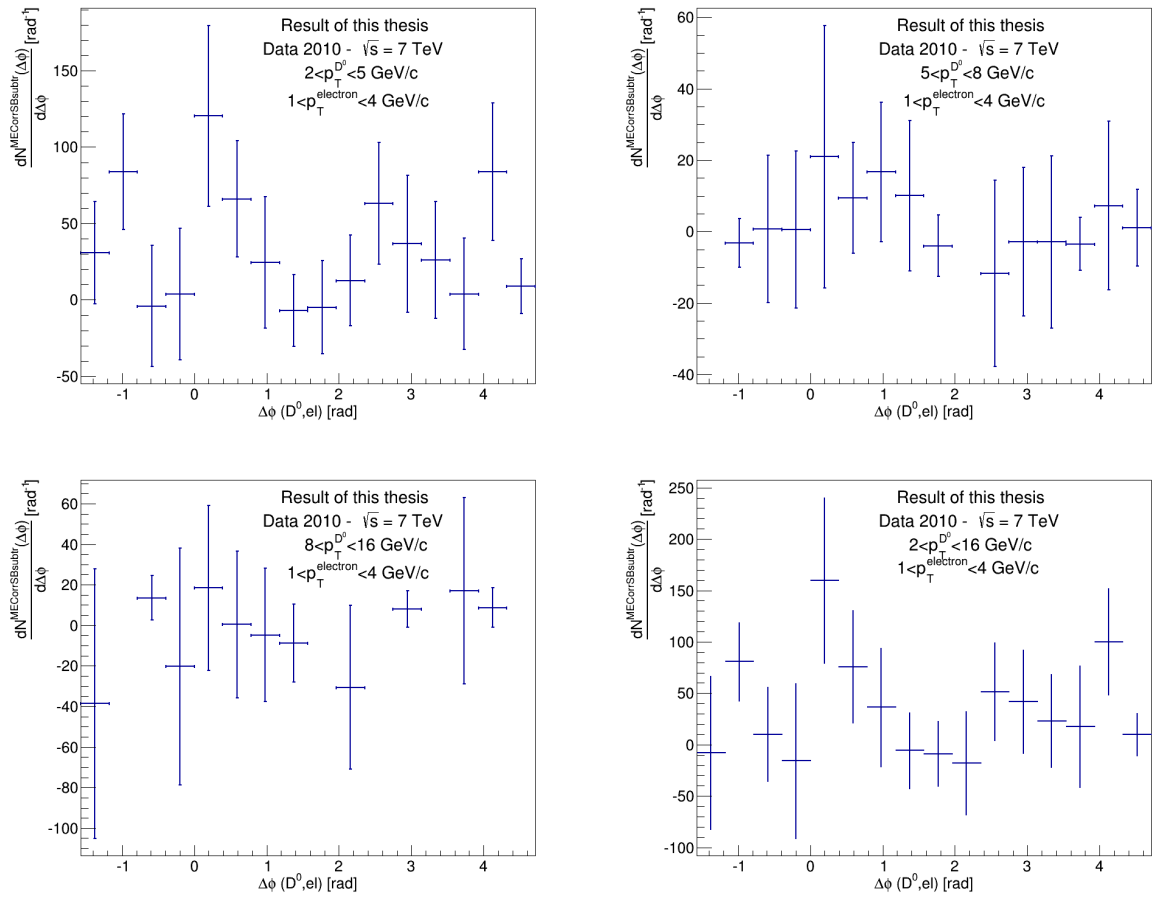

Figure 5.5: The $\Delta\phi$ distributions corrected for event mixing and sideband subtracted for various p_T regions for the D^0 meson. Top left: 2-5 GeV/c, top right: 5-8 GeV/c, bottom left: 8-16 GeV/c, bottom right: integrated region 2-16 GeV/c.

and 4.2.4, where the efficiency of the D^0 meson depends on p_T and multiplicity, and the electron efficiency depends on p_T, Z-vertex and η:

$$weight = \mathrm{Eff}_{D^0}(p_T, mult) * \mathrm{Eff}_{electron}(p_T, \mathrm{Vtx}_Z, \eta) \tag{5.3}$$

Only the electron efficiency has been applied to the $\Delta\phi$ distributions in the work presented in this thesis. The full implementation of the correction of the D^0 meson efficiency is not yet finalized in the analysis. The current strategy for the corrections of the efficiency for the D^0 meson is to apply the efficiency calculated for prompt D^0 mesons on the correlated pairs. The feed-down D^0 mesons are later subtracted based on FONLL predictions. This will only leave the correlation distribution of prompt D^0 mesons. The analysis has been performed while including the corrections for the prompt D^0 meson efficiency, without observing any dramatic effect. The corrections for the efficiency of the prompt D^0 mesons has been observed to be uniform in $\Delta\phi$.

The azimuthal angular correlation distribution after correcting for the electron efficiency can be seen for various p_T ranges of the electron, see figure 5.6. Four different p_T ranges are shown, 0.5-4 GeV/c, 0.5-1 GeV/c, 1-4 GeV/c and 1.5-6 GeV/c. The figure compares the $\Delta\phi$ distribution with and without correcting for the electron efficiency. As already mentioned, although the region below 1 GeV/c has the highest electron purity, this region suffers from a very high contribution of electrons coming from Dalitz decay of neutral mesons and conversion of photons in the material, see section 4.2. It can be seen that this region shows the least prominent near- and away-side, and the $\Delta\phi$ distribution is also observed to be most fluctuating in this region. By increasing the transverse momentum of the electron, and thus also getting a higher HFE purity, the near- and away-side peak is emerging more clearly. The p_T range between 1.5-6 GeV/c is also included, as the HFE purity should exceed 60% for the entire region, but it has to be treated slightly differently as the hadron contamination starts to increase for $p_T >$ 4-5 GeV/c. Also, the statistics is $\sim$ 25% lower with respect to the transverse momentum region 1-4 GeV/c. It is observed that the second to last, or last, $\Delta\phi$ bin, depending on which p_T region for the electron candidates one is investigating, are higher than expected, introducing a third "peak" which seems nonphysical. This peak is already seen in the raw distributions for the peak region, and is hence not an effect of the event mixing corrections, nor the side-band subtraction. It is also observed in the distribution without electron corrections, and it is also observed that it is present in the lowest momentum region for the D^0 meson candidates, namely 2-5 GeV/c, and it is most prominent for electron candidates with $p_T > 1$ GeV/c. In addition, it is also observed in the peak region when the peak region is reduced to $\mu\pm 2\sigma$, but is not shown in this thesis. As such, statistical fluctuations is currently the expected reason for the

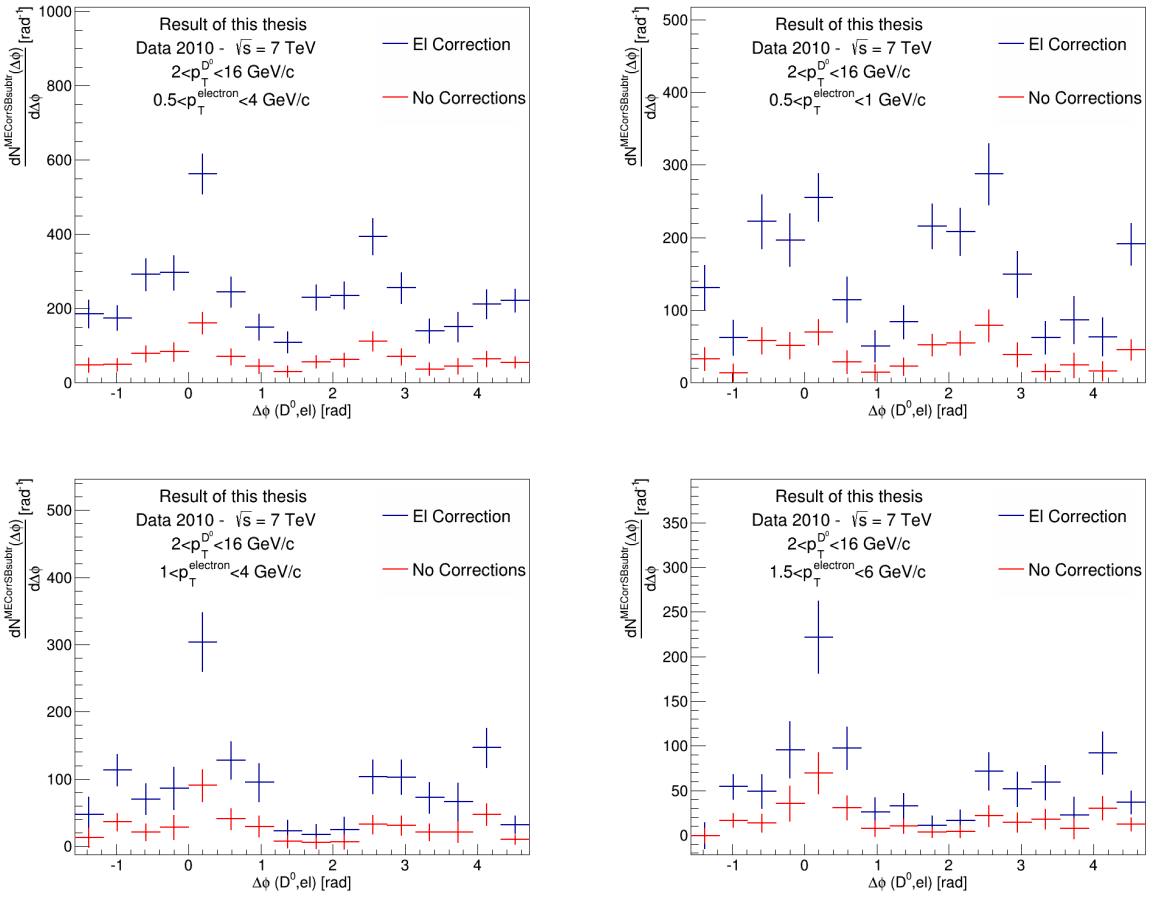

Figure 5.6: Comparison of correlation distributions without and with electron efficiency corrections, for various p_T ranges of the electron candidates. Top left: 0.5-4 GeV/c, top right: 0.5-1 GeV/c, bottom left: 1-4 GeV/c, bottom right: 1.5-6 GeV/c. All plots shows the integrated range 2-16 GeV/c for the D^0 meson candidates.

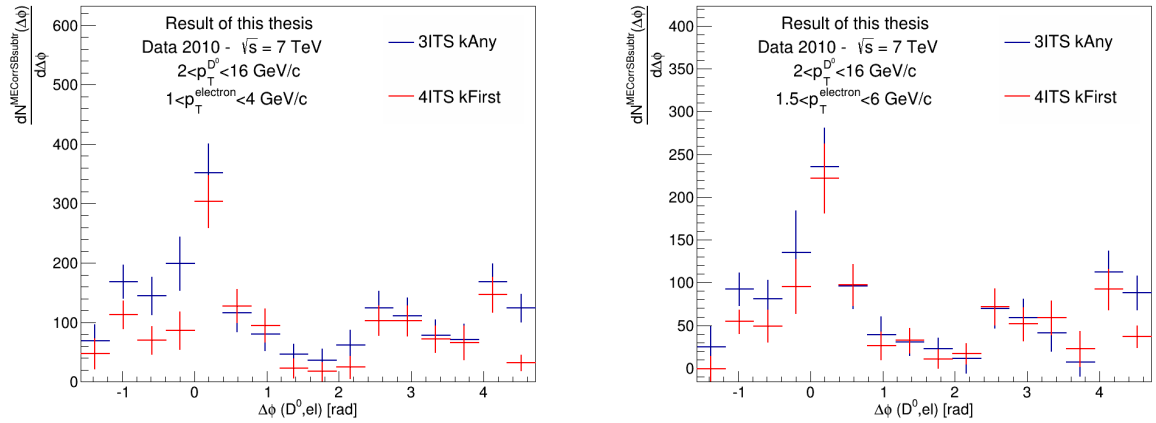

Figure 5.7: Comparison of different settings for the ITS detector, namely 3 ITS clusters per track and kAny, and 4 ITS clusters per track and kFirst, for various p_T ranges of the electron candidates. All distributions have been corrected for the electron efficiency. Left: 1-4 GeV/c, right: 1.5-6 GeV/c. All plots shows the integrated range 2-16 GeV/c for the D^0 meson candidates.

third "peak".

The corrected spectrum for the electron efficiency has also been compared for different selection criteria for the electron candidates. Figure 5.7 shows the comparison of the requirement kAny together with 3 ITS clusters per track, and the requirement kFirst together with 4 ITS clusters per track. The transverse momentum region for the D^0 meson candidates are 2-16 GeV/c, while it is 1-4 GeV/c and 1.5-6 GeV/c for the electron candidate. The trends of the distributions are observed to be similar, but there are some differences between the distributions. One of the explanations for this difference can be understood as a difference in the physics between the two electron selection strategies. This is mainly driven by the contribution of non-HFEs in the two selected electron samples, the requirement kAny will allow for a larger contribution of electrons from gamma conversion and Dalitz decay. Since these are not fully removed with the invariant mass cut on electron pairs, this electron strategy will consequently lead to a larger contribution of non-HFEs in the correlation distribution. However, this should lead to a minor influence on the final correlation distribution, especially in the selected p_T range of the electrons which are shown in these plots. Thus, a more likely explanation is that the difference observed between the distributions illustrates the systematic errors associated with the electron selection itself. As briefly illustrated here, the systematic error can potentially be substantial compared to the statistical errors.

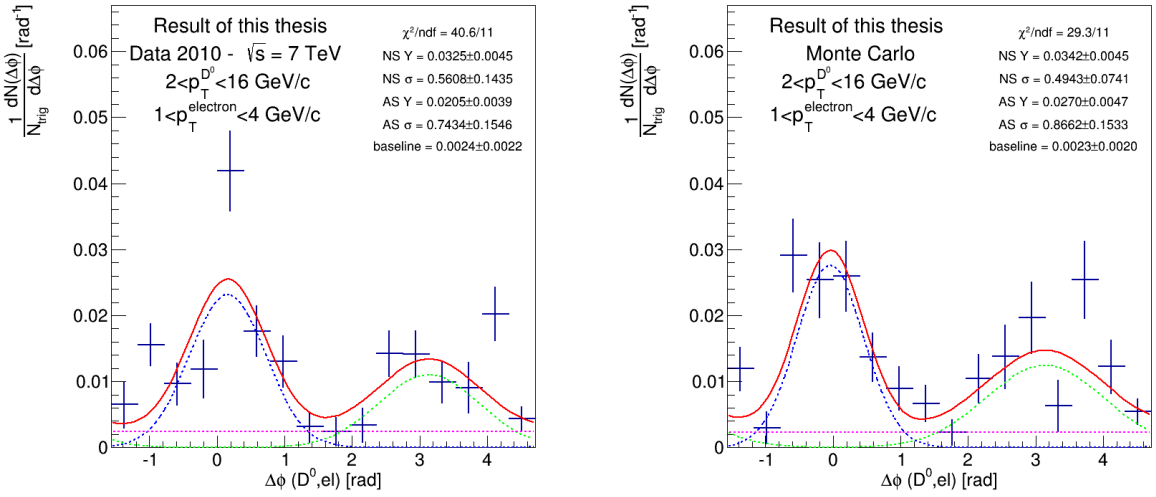

Figure 5.8: Fit of $\Delta\phi$ distributions for the transverse momentum region 2-16 GeV/c for the D^0 meson, and 1-4 GeV/c for the electron candidates. The left plot shows the fit to data, while right plot shows fit to $\Delta\phi$ distribution obtained from a minimum bias MC simulation.

5.6 Fitting the $\Delta\phi$ distribution

The properties of the azimuthal correlation distribution are quantified by fitting the distribution with a function composed of two Gaussian functions, modeling the near- and away-side peaks, and a constant term describing the baseline:

$$f(\Delta\phi) = c + \frac{Y_{NS}}{\sqrt{2\pi}\sigma_{NS}} e^{\frac{(\Delta\phi-\mu_{NS})^2}{2\sigma_{NS}^2}} + \frac{Y_{AS}}{\sqrt{2\pi}\sigma_{AS}} e^{\frac{(\Delta\phi-\mu_{AS})^2}{2\sigma_{AS}^2}} \tag{5.4}$$

Figure 5.8 shows the fit to the final corrected $\Delta\phi$ distribution, for the transverse momentum region 2-16 GeV/c for the D^0 meson and 1-4 GeV/c for the electron candidates. The analysis chain has also been applied identically on a minimum bias Monte Carlo simulation, where the events have been anchored to runs from the data taken in 2010 to take into account the actual data taking conditions. The figure also shows the fit to the distribution obtained by running on the simulation. The yields in the near-side and away-side peaks are further extracted from the obtained fit-function.

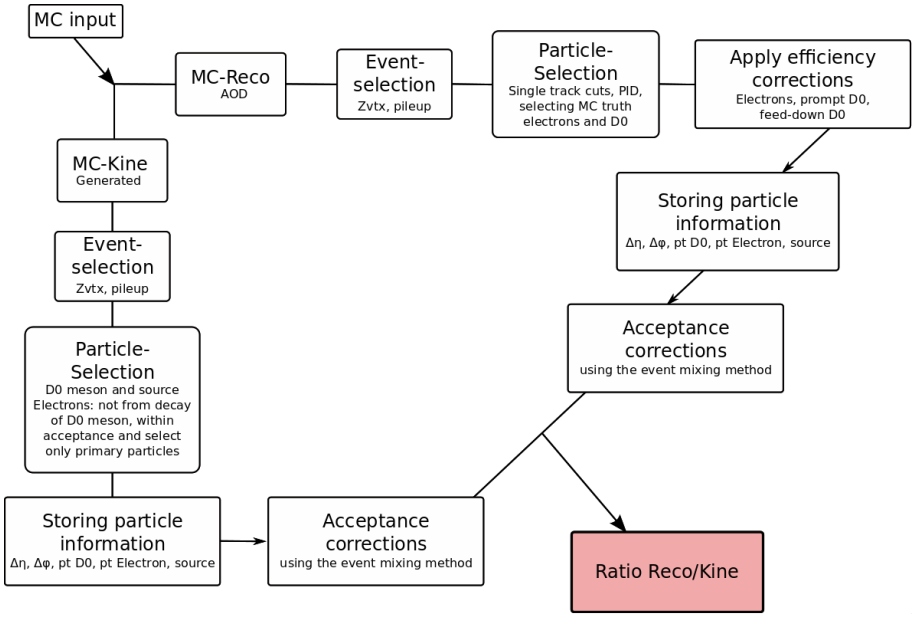

Figure 5.9: Overview of the work flow for the computation of the ratio of distributions of correlated D^0 mesons and electrons on kinematical level (kine) and reconstructed level (reco).

5.7 Studies on Monte Carlo simulations

In Monte Carlo simulations, one is usually investigating the particles on two different levels. The first is the particles generated by the event generator, also referred to as particles on the kinematical (kine) level. The second is the same particles after they have been propagated through the detector and subsequently found with the reconstruction algorithm, referred to as particles on the reconstruction (reco) level. The analysis has been performed on both the kinematical and reconstructed level, using a Monte Carlo simulation which is anchored to data taken in 2010. Each simulated event is enriched with a charm or a bottom quark pair, generated in $|y| < 1.5$. In a subset of the Monte Carlo events, the D^0 mesons are forced to decay in the hadronic channels.

On the kinematical level, information on all produced D^0 mesons and electrons along with $\Delta\phi$ is stored for further evaluation, together with information on whether the particle (D^0 meson or electron) originates from a charm or a bottom quark. All electrons either produced in the collision or decaying from heavy-flavour mesons, are referred to as primary electrons. Only primary electrons are selected, meaning that the electrons from gamma conversion in the detector material are not used in the further evaluation. The correlation distribution of D^0 mesons with electrons decaying from the same D^0 mesons will produce an artificially high and narrow

near-side peak. To avoid this auto-correlation, these electrons are removed. Apart from this, only acceptance cuts were applied to the particles.

In this way one can set up four scenarios:

- D^0 mesons and electrons both originating from charm quarks (cD^0-cEl)
- D^0 mesons and electrons both originating from bottom quarks (bD^0-bEl)
- All D^0 mesons with all electrons (D^0-El)
- All D^0 mesons with non heavy-flavour electrons (D^0-nonHFE)

The same procedure is performed on the reconstructed particles from the same Monte Carlo production. First, the D^0 meson and electron candidates are selected based on track cuts and PID. Out of these candidates, only the particles corresponding to true D^0 mesons and electrons are stored for further evaluation. As for the particles on the kinematical level, the source of the D^0 mesons and electrons are found and stored together with the information in $\Delta\phi$, $\Delta\eta$ and p_T of both the D^0 meson and electron. The event mixing corrections have been applied for both the analysis on the reconstructed level and the kinematical level, where they take into account the effects of the acceptance cuts. In addition, the D^0 meson and electron efficiencies have been applied on the reconstructed level, where the efficiency for the prompt and feed-down D^0 mesons is applied separately. Figure 5.9 shows the work flow schematically.

Figure 5.10 shows the correlation distribution for the four cases for particles on the kinematical level, together with the distribution on the reconstructed level for the cases:

- No corrections for the D^0 meson and electron efficiencies are applied.
- Correction for electron efficiency applied.
- Both corrections for electron and D^0 mesons have been applied.

As a consistency check, it has been tested if the results on the reconstructed level are compatible with the results on the kinematical level. The ratio of the distributions has been computed, referred to as the ratio reco-over-kine. If all corrections have been applied to the azimuthal angular correlation distribution at reconstruction level, this ratio should ideally be close to unity. This would indicate that the distribution on the kinematical level is kept throughout the various steps of the reconstruction. Figure 5.11 shows the ratios of the distributions on reconstructed level over kinematical level, for the three reconstruction scenarios listed above. All distributions on both the kinematical level and reconstructed level are first divided

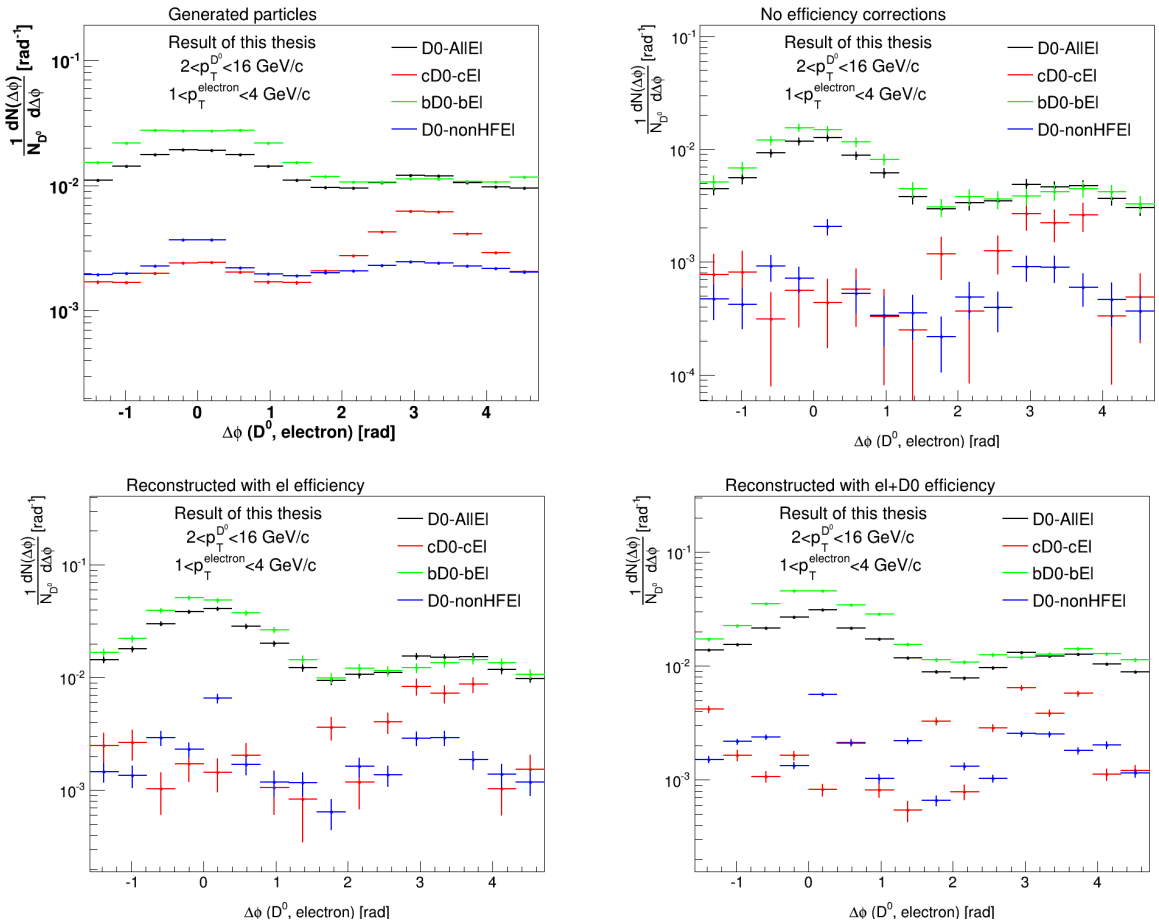

Figure 5.10: Correlation distributions from Monte Carlo simulated events. Top left: $\Delta\phi$ distributions on the kinematical level. Top right: $\Delta\phi$ distributions on the reconstructed level with no corrections for the efficiencies of D^0 mesons and electrons. Bottom left: $\Delta\phi$ distributions corrected for electron efficiency on the reconstructed level. Bottom right: $\Delta\phi$ correlations on the reconstructed level corrected for both D^0 meson and electron efficiencies. The transverse momentum for electrons is 1-4 GeV/c, and 2-16 GeV/c for the D^0 meson.

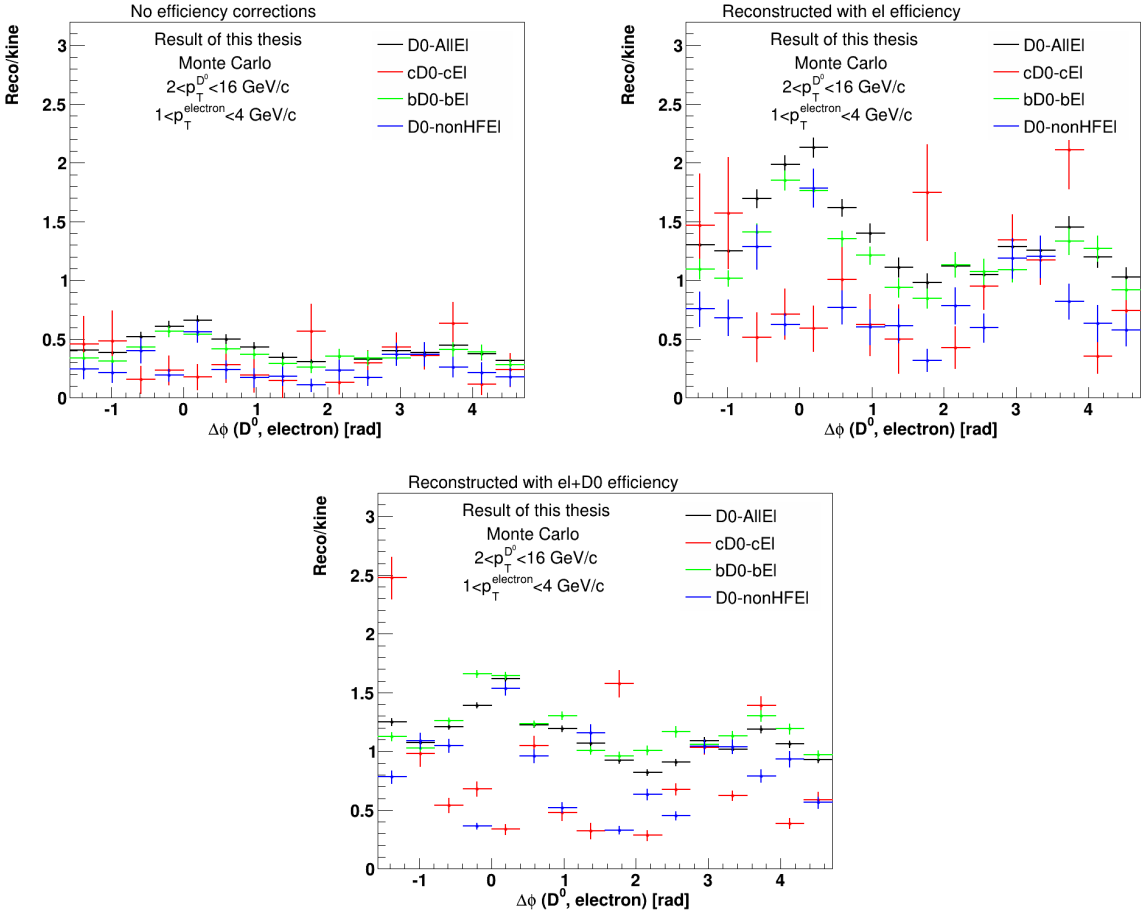

Figure 5.11: The ratio of different distributions on reconstruction level over kinematical particle level. Top left: the distribution without any corrections for efficiency. Top right: the distribution with only corrections for the electron efficiency. Bottom: Distributions with corrections for electron efficiencies and D^0 efficiencies are included. The ratio should ideally be unity, but as can be seen, especially the near- and away-side shows a difference. Transverse momentum for electron $1<p_T<4$ GeV/c, and $2<p_T<16$ GeV/c for the D^0 meson.

by the respective number of triggers, that means that the cD^0-cEl distribution is divided by the number of prompt D^0 mesons in the given p_T range. For the bD^0-bEl distribution, the number of triggers are given by the number of feed-down D^0 mesons in the given p_T range, and so on.

Large fluctuations are observed in the computed ratios. When applying the corrections for the electron efficiency, the ratio for bD^0-bEl, and therefore also D^0-AllEl, are observed to be consequently larger than 1, indicating that the distribution on the reconstructed level seems to find more electrons per D^0 meson than on the kinematical level, especially in the near-side region. The trend for cD^0-cEl seems to be opposite, the ratio seems to be consequently below 1, though with large fluctuations. When comparing the three scenarios, namely no corrections for efficiency, only corrections for electron efficiency, and applying both corrections, the best ratio seems to be the scenario when applying both corrections for electrons and D^0 mesons, which is also to be expected. The ratio for the b-pairs deviates the most, which can also be observed while investigating the raw distributions on the kinematical and reconstructed level. The distribution for the b-pairs seems to have a more narrow and higher near-side peak on the reconstructed level than on the kinematical level, which also leads to the higher ratio in the near-side region. Also, as a general remark on all the different sources, it is observed that the away-side region seems to be less fluctuating than the near-side region.

The large fluctuations are likely to partially originate from limited statistics on the reconstructed level. These studies are ongoing.

5.8 Results on near-side and away-side yields

The final correlation plots after the inclusion of all corrections are shown in figure 5.12. The plots are produced for the D^0 meson integrated transverse momentum range, for different p_T regions for the electron candidates. All distributions are compared to $\Delta\phi$ distributions obtained from a minimum bias Monte Carlo simulation, where the analysis steps are identical to the one utilized on data. The Monte Carlo simulation is produced with the PYTHIA 6.4.21 event generator with the Perugia 0-parameter tuning.

By eye it can be seen that the distributions from data and Monte Carlo simulations in figure 5.12 exhibit similar shapes. In order to quantify the comparison, the near-side and away-side yields and sigma are extracted from the $\Delta\phi$ distribution, as explained in section 5.6. The comparison of the extracted values for data and Monte Carlo for the D^0 meson integrated p_T range and for the p_T region 1-4 GeV/c for the electron candidates, is shown in figure 5.13. It is observed that the extracted

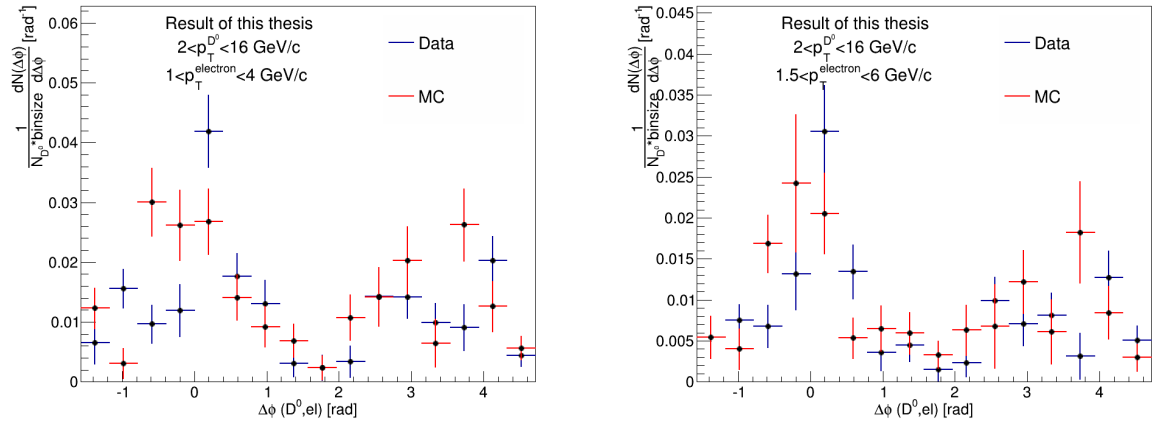

Figure 5.12: Comparison of different correlation distribution for various p_T ranges of the electron candidates, retrieved from data and Monte Carlo simulations. Left: 1-4 GeV/c, Right: 1.5-6 GeV/c. The plots show the integrated transverse momentum range for the D^0 meson candidates.

values from data and the Monte Carlo simulation is consistent within the statistical uncertainty.

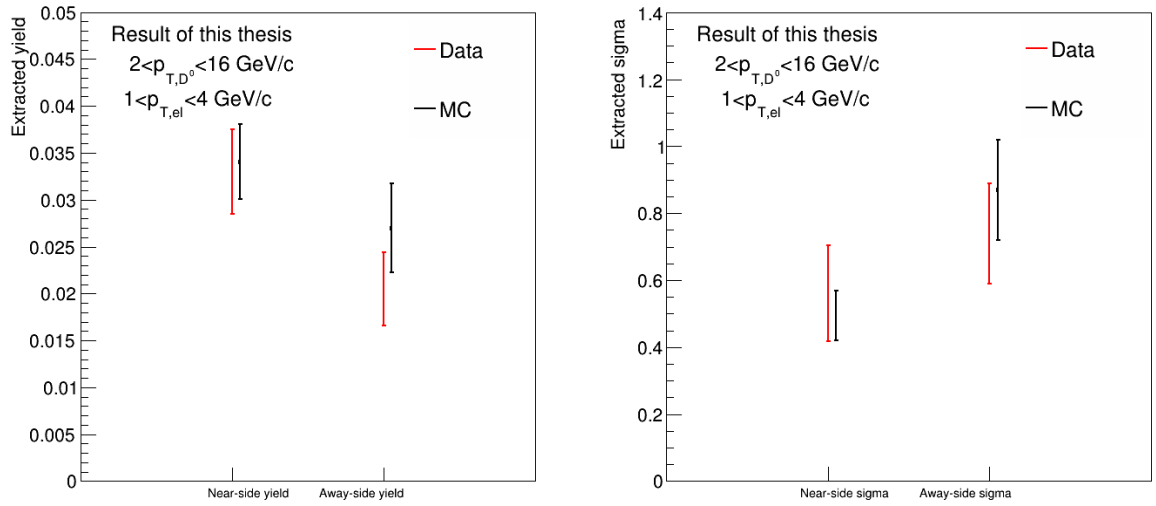

Figure 5.13: Comparison of extracted near-side and away-side yield (left) and sigma (right) for data and Monte Carlo. The transverse momentum region for the D^0 meson candidates is 2-16 GeV/c, while it is 1-4 GeV/c for the electron candidates. The extracted values are consistent within statistical uncertainties.

Chapter 6

Conclusion and outlook

This thesis has focused on the azimuthal angular correlation of D^0 mesons with heavy-flavour electrons. A lot of the effort involved the setup of the analysis software and selection of heavy-flavour electrons. A compromise between electron efficiency and a high purity heavy-flavour electron sample has been worked out, where the main focus has been to obtain a high purity HFE sample.

The result of this thesis shows that the statistics available prevents currently any quantitative conclusion of the analysis. There are currently no theoretical prediction for the analysis, thus the results have been compared to Monte Carlo simulations based on PYTHIA. The general trend seems to be that PYTHIA is in agreement with what is observed in data, however the statistical limitations prevent a solid conclusion.

There are still potential improvements to be done for the analysis presented in this thesis. For the electron selection, one has the possibility of adding more detectors to be used for particle identification. For the work presented in this thesis, the most relevant one is the TRD detector after it has been fully installed. This has the potential of extending the p_T coverage for the electron candidates up to 10 GeV/c. This is an important improvement as the hadron contamination starts to increase above 4-5 GeV/c. The other interesting detector to use for PID, is the electromagnetic calorimeter EMCAL. There exists a high p_T (electron) trigger in ALICE utilizing the EMCAL detector, which will increase the statistics and will give a higher signal-over-background ratio for the D^0 mesons [76]. It is also important to mention that if the EMCAL trigger is to be used, the electron has to be the trigger of the analysis, not the D^0 meson, due to the limited acceptance of the EMCAL detector. The EMCAL trigger has already been employed during data taking, both for p-p collisions, Pb-Pb and p-Pb collisions, and the initial analysis on these data sets shows promising results.

The event mixing technique, or rather the implementation of it, is another aspect

that can be improved. The drawback of the current implementation is that the mixing of the events is performed while running on grid. The data set is divided into several parts, or jobs, when running on grid, and the analysis chain will be run independently on the different jobs. This will make the statistics for the mixed event corrections highly dependent on the number of events per analysis job on grid. The suggestion is to instead store all D^0 meson and electron candidates while running on grid, and later do the event mixing locally. This approach will make sure that all D^0 mesons will be mixed with all electron candidates, and will greatly increase the statistics for the mixed event analysis, and thus improve systematical errors, of the event mixing corrections.

Our analysis group has also started to investigate other collision systems, along with investigations of different p-p collision data sets. The p-p data taken in 2012 is of special interest, as the center-of-mass energy of the p-p collisions was increased to 8 TeV. This will increase the production cross section for both charm and bottom quarks, and consequently also the statistics. The investigations of p-Pb collisions has started, and as briefly mentioned, the initial analysis of EMCAL triggered data shows promising results. Studies of the Pb-Pb collisions recorded in 2011 have also been performed, but this analysis needs additional treatment, both when addressing the D^0 meson and the electron candidate selection.

This thesis shows the feasibility of the constructed analysis chain. The important next step is to reduce the systematical and statistical errors of the analysis. More statistics is needed to achieve this goal, and perspectives for the analysis are discussed in the following.

6.1 Expectations for Run 2

The LHC is at the moment being upgraded to allow for a higher luminosity and collision energy. It will start its operation again in 2015, referred to as Run 2, and will continue to record data till 2018. Parts of the ALICE detector is at the same time being upgraded. This includes increasing the read out rate of the TPC detector for Pb-Pb collisions by a factor of 2, which will make it possible to record Pb-Pb collisions at 500 Hz. The TRD detector will also be fully installed during this period, which makes the inclusion of the TRD detector for particle identification of the electron selection feasible.

For Pb-Pb collisions it is expected that ALICE will record 1 nb^{-1} in Run 2, which is around 10 times higher for Pb-Pb collisions than what has already been recorded (100 μb^{-1}). For p-p collisions, the read-out rate in ALICE is expected to be 10-100 kHz, and it is expected to record 1x10^{10} minimum bias events. This is an

increase of a factor 30 compared to the statistics used for the analysis in this thesis. Together with expanding the p_T region for the electron selection using the TRD detector, this will reduce the statistical uncertainties of the analysis substantially.

6.2 Statistics estimate for the upgrade for Run 3

As has been demonstrated in this thesis, the available statistics from 2010 prevents quantitative conclusion on the result of the analysis. The LHC will have a long shut-down period, starting in 2018, where the ALICE detector is planned to be upgraded. As a part of this, it is of great interest to get a statistics estimate necessary for the analysis described in this thesis. The planned upgrades will allow for a higher collision rate in the ALICE detector, and also to improve the position resolution of tracks close to the interaction vertex. This is of vital importance for the D meson reconstruction. The plans include currently [91]:

- **New beam-pipe** at 19.8 mm, which is closer to the interaction vertex compared to the current one with outer radius 29.8 mm.
- **New ITS.** The new ITS detector will have seven layers spanning radii 22-430 mm. This is an improvement from the current ITS detector, which has six layers with radius 39-430 mm. Depending on the final chosen detector scheme, the material budget per layer will be reduced from 1.14% X_0 to better than 0.5% X_0. The combination of the two will make it possible to improve the resolution of the charged track impact parameter by a factor of three. The relative momentum resolution of the silicon tracker standalone would be about 2% up to 2 GeV/c, and remain below 3% up to 20 GeV/c. The current ITS detector has a read-out rate of 1 kHz, which is restricting ALICE to use only a small fraction of the full 8 kHz collision rate currently provided by the LHC. The upgraded ITS detector will allow for a higher read out rate, namely 100 kHz.
- **Upgrade of the TPC detector**, replacement of the read-out multi-wire proportional chambers with GEM (Gas Electron Multiplier) detectors and new continuous read-out electronics. The upgraded TPC detector will allow for a read out rate of 50 kHz in Pb-Pb collisions. ALICE will then be capable of accumulating 10 nb^{-1} of Pb-Pb collisions, recording about 10^{11} interactions.
- **Upgrade of read-out electronics** for the TRD, TOF, PHOS and Muon spectrometer for high rate operation.
- **Upgrade of forward trigger detectors**.

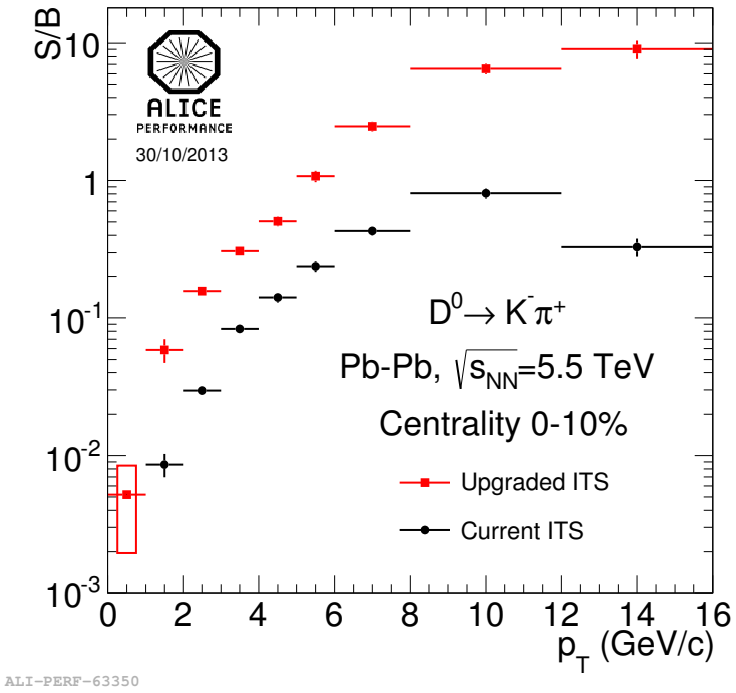

Figure 6.1: Comparison of the D^0 meson signal/background (S/B) with the current and upgraded detector as expected for 0-10% centrality Pb-Pb collisions at $\sqrt{s_{NN}}$=5.5 TeV.

6.2.1 Upgrade studies for Pb-Pb collisions

The new ITS detector will provide the most significant improvements for the analysis. The reduction of the material budget for the entire detector, together with having more layers closer to the beam-pipe, will allow for a better efficiency while reconstructing D^0 mesons. In addition, the new ITS detector will minimize conversion electrons, and the expectation is to be able to get a higher purity HFE sample. The electron efficiency is improved with the new detector, and will be shown later. This will, together with higher collision energy and higher collision rate, have the potential of improving the statistics for the analysis significantly.

The statistics estimate for the analysis in this thesis is extracted using two Monte Carlo simulations. The first is a simulation of Pb-Pb events with the upgraded ITS detectors, at $\sqrt{s_{NN}} = 5.5$ TeV using the HIJING generator [92]. The collisions have centrality 0-10%, and have an average charged-particle pseudo-rapidity density of $\mathrm{d}N_{ch}/\mathrm{d}\eta = 2000$. In the simulation, the heavy-flavour signal is added to the HIJING event using a cocktail of parametric generators and heavy-quark pairs generated with PYTHIA [48]. This simulation is used to extract the expected D^0 meson signal (and

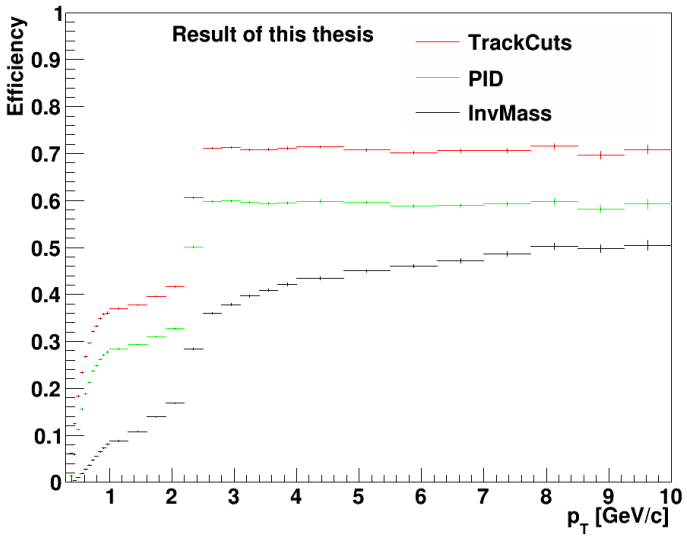

Figure 6.2: Efficiency of selecting heavy-flavour electrons with the upgraded ITS detector for central Pb-Pb collisions.

background) with the upgraded detector, and is also used to estimate the efficiency of various electron sources. Figure 6.1 shows the expected S/B for the D^0 meson signal with the ITS detector after upgrades compared to the current ITS, estimated for central Pb-Pb events. Figure 6.2 shows the efficiency of selecting heavy-flavour electrons with the upgraded ITS, using the same track cuts as for the p-p analysis, with the exception of lowering the invariant mass cut to 50 MeV/c. It is observed that the efficiency, compared to the one obtained for p-p collisions, has increased significantly looking only at the efficiency after single track cuts.

The simulation has also been used to estimate the baseline of the $\Delta\phi$ distribution of D^0 mesons with all electrons. The baseline represents the underlying event and has been extracted by a fit to the distribution, as described in section 5.6. The baseline has been obtained for the various electron p_T ranges 0.5-10 GeV/c, 1.0-10 GeV/c and 1.5-10 GeV/c:

- 0.5-10 GeV/c: 0.18 [rad^{-1}]
- 1.0-10 GeV/c: 0.14 [rad^{-1}]
- 1.5-10 GeV/c: 0.11 [rad^{-1}]

The baseline has been found to be similar for the different p_T regions for the D^0 mesons, thus it is mainly governed by the p_T region of the selected electrons. In the following, a constant efficiency of 0.3 is assumed for the electron selection. This

is currently overestimating the selection efficiency (including the invariant mass cut on electron pairs) at low p_T, and underestimated at higher p_T, but is justified as a first approximation.

The second Monte Carlo simulation is a PYTHIA simulation with the requirement of having at least one D^0 meson in each event. This Monte Carlo production has 9x10^6 events, and the purpose of this MC production is to provide $\Delta\phi$ distributions for D^0 mesons with different electron sources. For the studies performed for this thesis, it is as a first approximation assumed that a perfect heavy-flavour electron sample is obtained, thus only $\Delta\phi$ distributions of electrons from charm and bottom quarks are utilized. The steps of the analysis for the statistics estimate is explained in the following:

- Obtain the per-trigger-yield $\Delta\phi$ distribution from the PYTHIA simulations for the required D^0 mesons and heavy-flavour electrons. Studies are performed for the cases prompt only, feed-down only and both of them combined. This $\Delta\phi$ distribution is referred to as the input histogram.

- For the case of combining the prompt and the feed-down contribution, weights are applied to the individual distributions which roughly correspond to the fraction of prompt and feed-down as estimated on the basis of FONLL predictions and D^0 meson efficiency:

  - $0.93 \cdot$ prompt$+0.07 \cdot$ feed-down in $3< p_{T,D0} <5$ GeV/c
  - $0.9 \cdot$ prompt$+0.1 \cdot$ feed-down in $5< p_{T,D0} <8$ GeV/c
  - $0.86 \cdot$ prompt$+0.14 \cdot$ feed-down in $8< p_{T,D0} <16$ GeV/c.

- The $\Delta\phi$ distribution of D^0 mesons with electrons is corrected for the HFE efficiency,

- Based on a fit to the input histogram, the yields of the near-side and away-side peaks together with the sigma of the away-side peak are extracted and stored as reference values.

- The $\Delta\phi$ distributions for background D^0 mesons are assumed to exhibit a similar shape as the signal. After normalizing the distribution according to the S/B in figure 6.1, the distribution for the background is added to the signal.

- If asked for, v_2 (=0.05) is also added as a modulation of the background before adding the background to the signal.

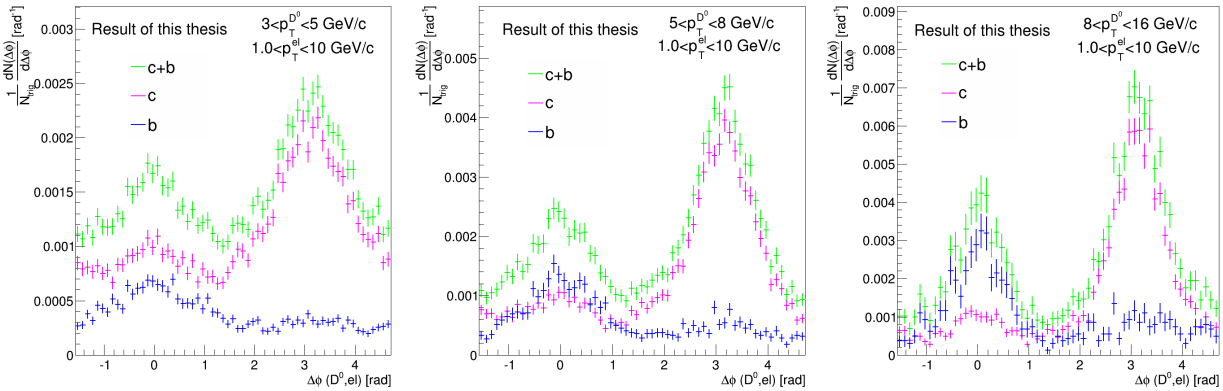

Figure 6.3: Comparison of input distributions obtained from PYTHIA simulations for prompt, feed-down and the combined contribution for the different p_T ranges for the D^0 meson. The p_T distribution for the electrons is 1.0-10 GeV/c.

- It is assumed that the v_2 contribution can be subtracted from the near-side correlations at large $\Delta\eta$. Thus, $\Delta\phi$ distributions are created for large $\Delta\eta$ values for both the signal and background.
- Using the expected number of estimated D^0 meson triggers, the distributions for the signal, background and large $\Delta\eta$ values are scaled to more realistic distributions. The number of triggers are calculated as:

  $$\text{nrTriggers=nrEvents} \cdot (\text{significance per event})^2 \cdot (1+\tfrac{1}{\text{S/B}})$$

- The same distributions are independently smeared according to Poisson statistics.
- The $\Delta\phi$ distributions for large $\Delta\eta$ values and the background are further subtracted from the signal distribution and fitted to extract the yield and sigma of the near-side and away-side peak. The difference of the yield and sigma (residuals) of the input and output distribution are computed:

  (inputValue-outputValue)/inputValue

- The last two points are performed 100 times to get realistic fluctuations. This will produce a histogram referred to as the residual histogram, and the relative uncertainty is extracted from this histogram by a fit using a Gaussian function to the histogram.

Figure 6.3 shows the input histograms for the three p_T regions for the D^0 mesons, 3-5 GeV/c, 5-8 GeV/c and 8-16 GeV/c, for the contribution from only prompt, from

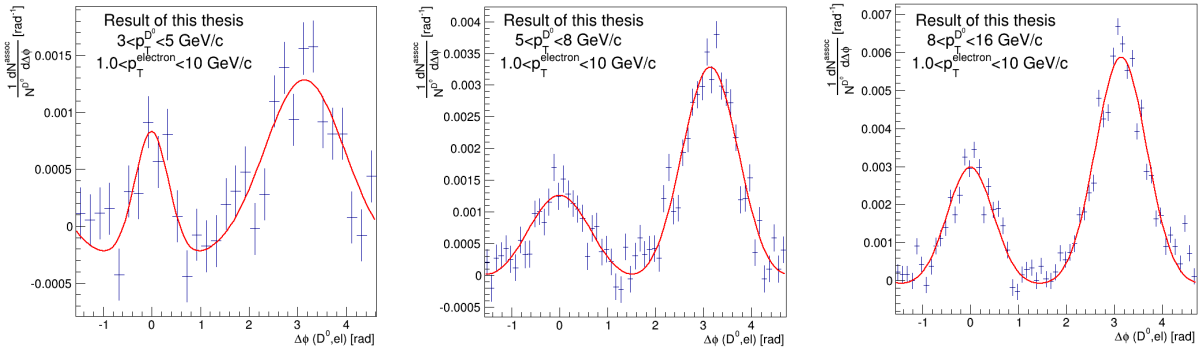

Figure 6.4: Output histograms for both contributions after smearing and subtraction of background. The histograms show the p_T 3-5 GeV/c (left), 5-8 GeV/c (middle) and 8-16 GeV/c (right) for the D^0 meson, and 1.0-10 GeV/c for the electrons.

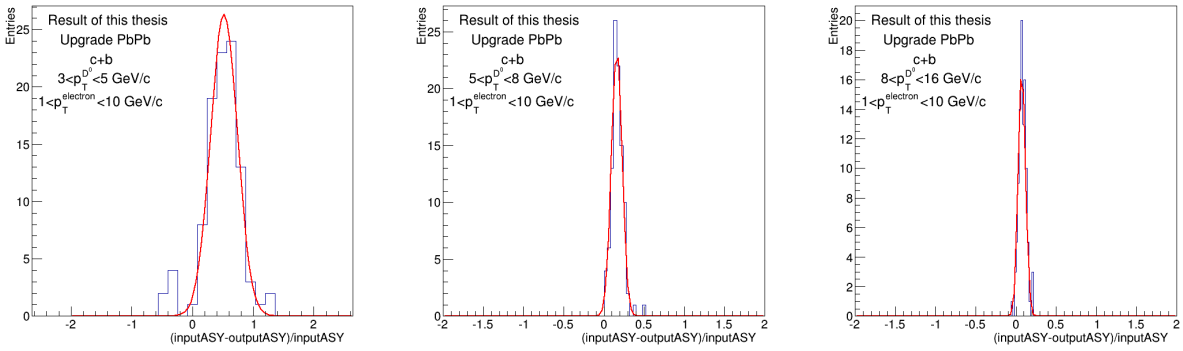

Figure 6.5: Residual histograms showing the difference of the input and output value of the extracted away-side yield. The histograms show the p_T regions 3-5 GeV/c, 5-8 GeV/c and 8-16 GeV/c for the D^0 meson, and 1.0-10 GeV/c for the electrons. It is observed that the distribution has a mean value closer to 0, and a more narrow peak, for increasing D^0 meson p_T.

only feed-down and for the combination of the two contributions. It is observed that the charm contribution is dominating the away-side peak for all transverse momenta, while the bottom contribution is dominating in the near-side peak for high p_T.

As the statistics studies for the upgrade plans presented in this thesis expect a pure heavy-flavour electron sample, the yield and the sigma of the near-side peak will be limited by the physics. The near-side peak is artificially low compared to what is measured experimentally. The expectation is that electrons decaying from D^0 mesons in gluon splitting events, where one can have both charm quarks in the near-side, and electrons from Dalitz decay originating from the charm jet, both will contribute to a $\Delta\phi$ distribution with a near-side peak. This will increase the yield in the near-side. Due to this reason, only the relative uncertainty for the yield and sigma for the away-side peak is shown.

The flow contribution can be subtracted in the near-side peak relying on η-gaps to get the associated yields. In the away-side peak, the signal is in addition also spread along $\Delta\eta$, which makes the subtraction of flow non-trivial. In central events, the flow is supposed to be small. However, higher harmonics, especially v_3, might be relevant and these cannot be subtracted with the eta-gap method, even in the near-side. Thus, the most likely method to deal with this problem is to do a fit to the correlation plots with a v_2 and v_3 component using the measured values of v_2 and v_3 for D mesons, HFEs and background electrons. This will reduce the statistical uncertainty but will introduce systematical uncertainty due to the assumption above. As a results, and also since these studies only look at the away-side peak, the flow component has been left out in the creation of the relative uncertainty of the away-side yield and sigma shown in this thesis.

Figure 6.4 illustrates the output histograms after smearing of the various histograms, followed by the subtraction of background. The output histograms are shown for the D^0 meson p_T regions 3-5 GeV/c, 5-8 GeV/c and 8-16 GeV/c. Examples of the residual histograms for the away-side yields, for the same p_T regions as for the output histograms, are shown in figure 6.5. For all histograms, the p_T interval for the electrons is 1-10 GeV/c. It is observed that the residual histograms exhibit a shift towards a positive mean value. The shift in the residual histograms is still under investigation. The trend of the residual histograms is a more narrow peak with smaller mean value for increasing p_T of the D^0 meson.

The relative uncertainty as a function of the D^0 meson p_T is shown for both contributions (figure 6.6), for only charm (figure 6.7) and for only bottom contribution (figure 6.8). All of them are shown for the electron p_T range 0.5-10 GeV/c, 1.0-10 GeV/c and 1.5-10 GeV/c. Due to the assumption of a pure HFE sample, the more realistic representation of the electron sample will be for electrons with $p_T >$

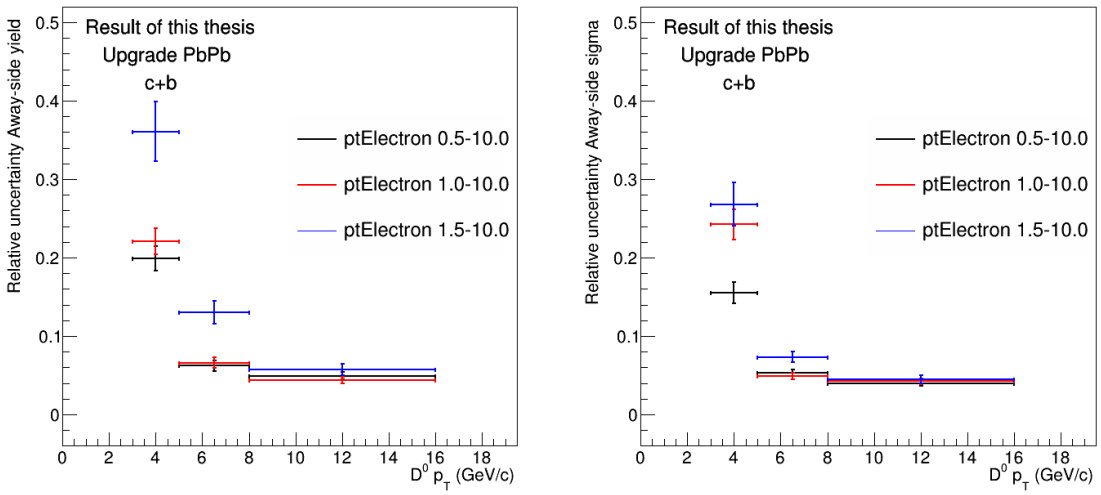

Figure 6.6: The relative uncertainty for the analysis with the combined contribution of prompt and feed-down, using the upgraded ITS detector for central Pb-Pb collisions. The away-side yield (left) and sigma (right) is shown versus D^0 transverse momentum. The relative uncertainty is obtained for the p_T regions 0.5-10 GeV/c, 1.0-10 GeV/c and 1.5-10 GeV/c for the electron.

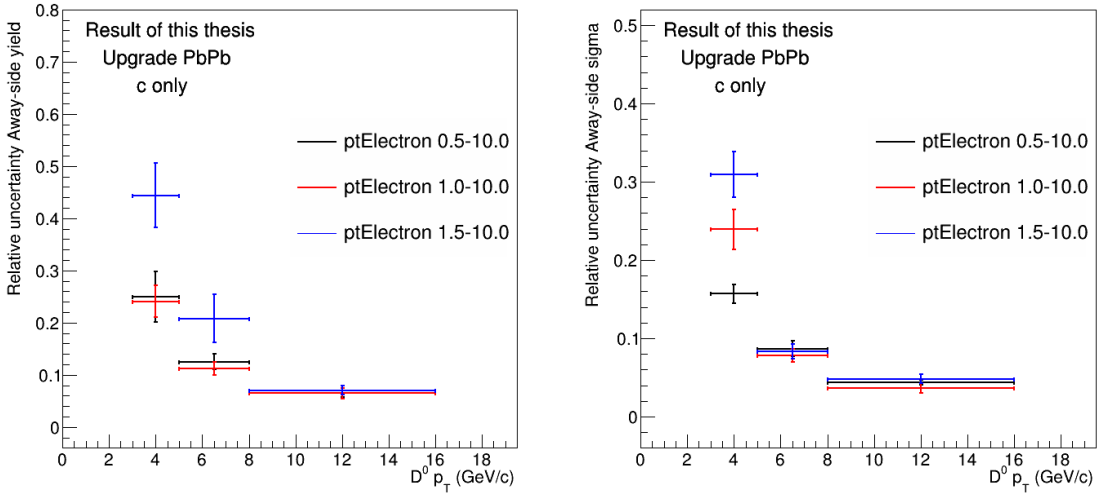

Figure 6.7: Relative uncertainty for D^0 mesons and electrons from charm quarks, using the upgraded ITS detector for central Pb-Pb collisions. The away-side yield (left) and sigma (right) is shown versus D^0 transverse momentum. The relative uncertainty is obtained for the p_T regions 0.5-10 GeV/c, 1.0-10 GeV/c and 1.5-10 GeV/c for the electron.

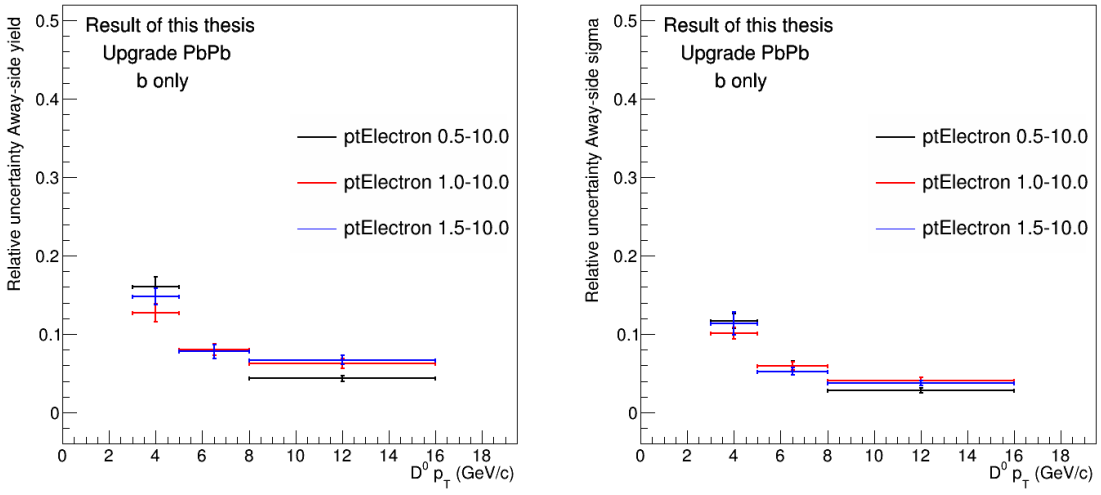

Figure 6.8: Relative uncertainty for D^0 mesons and electrons from bottom quarks, using the upgraded ITS detector for central Pb-Pb collisions. The away-side yield (left) and sigma (right) is shown versus D^0 transverse momentum. The relative uncertainty is obtained for the p_T region 0.5-10 GeV/c, 1.0-10 GeV/c and 1.5-10 GeV/c for the electron.

1 GeV/c. This is because the selected electrons in the current analysis in the p_T region 0.5-1 GeV/c have a high contamination of background electrons. The upper limit is currently set to 10 GeV/c, with the assumption that the p_T coverage for the electron selection is expanded in the analysis.

6.2.2 Upgrade studies for p-p collisions

There are not yet any available Monte Carlo simulations dedicated to p-p collisions for the upgraded ALICE detector. Thus, as a first approximation for the expected relative uncertainty in p-p collisions with the upgraded detector, the S/B and significance/event obtained for minimum bias Monte Carlo simulations for p-p collisions in 2010 is used, keeping in mind that this is a very conservative approximation. An integrated luminosity of 6 pb^{-1} for p-p collisions is required to get a sample of p-p reference data which will have a statistical significance comparable to that of the Pb-Pb data. This would correspond to $4x10^{11}$ interactions, which is significantly higher than the recorded data used in this thesis ($3.2x10^8$). With an event read-out rate of 200 kHz, this will result in a data taking period of a few months.

The same procedure as for Pb-Pb collisions has been used to compute the relative uncertainty for p-p collisions, with the exception of the flow component. The setup

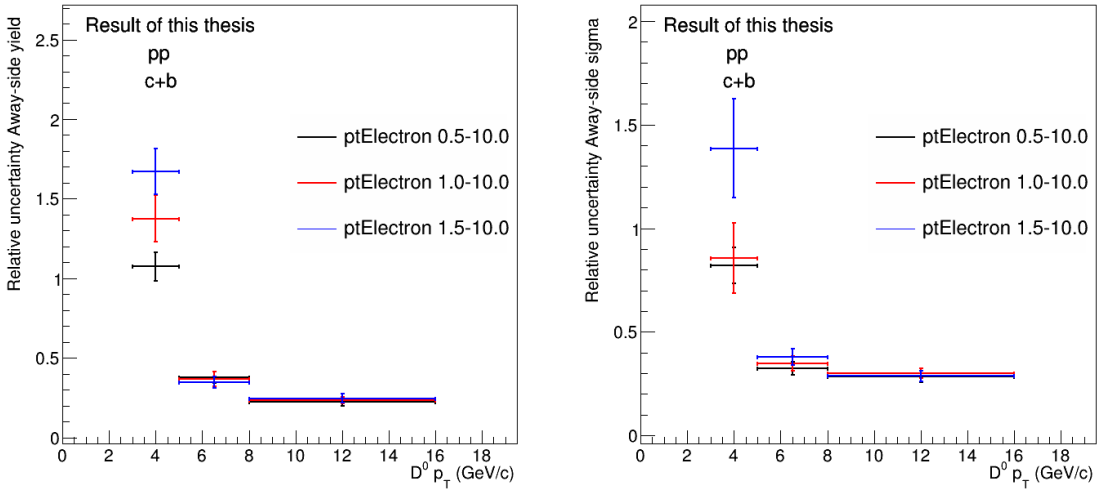

Figure 6.9: The relative uncertainty for the analysis with the combined contribution of prompt and feed-down, using the current ITS detector for p-p collisions. The away-side yield (left) and sigma (right) is shown versus D^0 transverse momentum. The relative uncertainty is obtained for the p_T regions 0.5-10 GeV/c, 1.0-10 GeV/c and 1.5-10 GeV/c for the electron.

has been run with both the statistics extracted from the Monte Carlo minimum bias sample for 2010 p-p data, and the statistics estimated for the upgrade scenario. The former will thus allow for a test of the setup, to see if the relative uncertainty that has been obtained for the various scenarios is realistic. The relative uncertainty using the numbers from p-p 2010 is shown in figure 6.9, illustrating that the setup yields high errors with these numbers. The relative uncertainty using the same significance per event and S/B, but with the expected statistics for p-p collisions with the upgraded detectors, is shown in figure 6.10. Even with the conservative estimate for S/B and significance per event, it is seen that the expected relative uncertainty is much lower, and shows great promise.

6.2.3 Conclusion

There are still some open points for the studies, mainly connected to the treatment of the background. It is not a realistic assumption to get a pure HFE sample, and the background from the underlying event can drive large statistical uncertainties. Even so, the expectation is that the away-side peak is more dominated by HFE pairs than in the near-side peak, which makes the analysis very intriguing to continue, especially after 2019. Another important, and intriguing, part of the analysis in

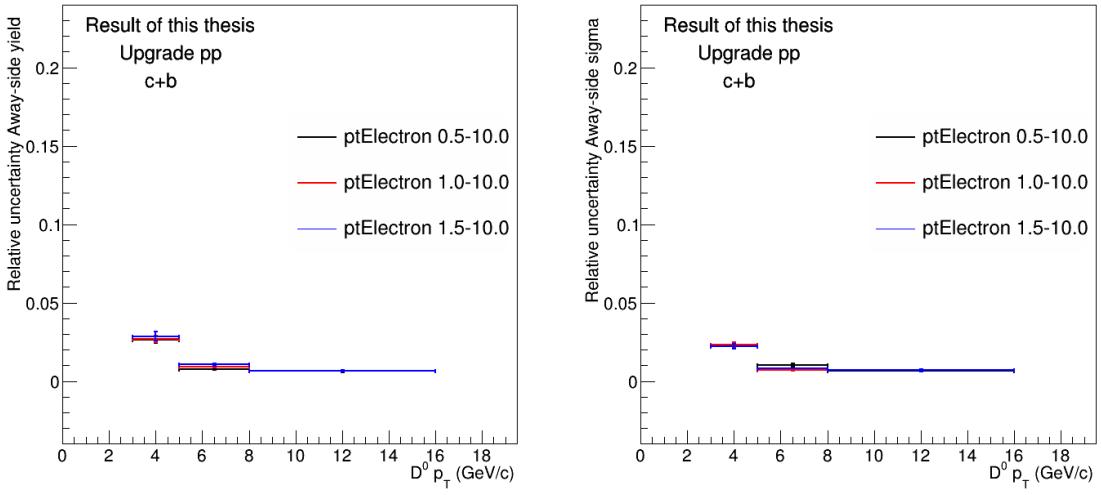

Figure 6.10: The relative uncertainty for the analysis with the combined contribution of prompt and feed-down, expected for the upgraded ITS detector in p-p collisions. The away-side yield (left) and sigma (right) is shown versus D^0 transverse momentum. The relative uncertainty is obtained for the p_T regions 0.5-10 GeV/c, 1.0-10 GeV/c and 1.5-10 GeV/c for the electron.

Pb-Pb collisions, is the separation of the charm and the beauty contribution. This will require dedicated simulations using different Monte Carlo event generators to study the effect of various template shapes.

The result of the studies on both Pb-Pb and p-p collisions with the upgraded ALICE detector is promising for the azimuthal angular correlation analysis of D^0 mesons with heavy-flavour electrons. For the combination of the contribution from charm and beauty pairs, the statistical uncertainty on the away-side yield and Gaussian σ is below 40% for Pb-Pb collisions and below 30% if the electron p_T range is 1.0-10 GeV/c or 0.5-10 GeV/c. The statistical uncertainty is decreasing for increasing D^0 meson p_T. For p-p collisions the estimated statistical uncertainty is below 5%, even using a conservative S/B and significance per event. This is a very significant improvement compared to the same studies performed using the statistics extracted from Monte Carlo simulations based on 2010 data.

Bibliography

[1] M. Wilde, "Measurement of direct photons in p-p and Pb-Pb collisions with ALICE," *Nuclear Physics A*, vol. 904-905, no. 0, pp. 573c–576c, 2013. The Quark Matter 2012,Proceedings of the XXIII International Conference on Ultrarelativistic Nucleus - Nucleus Collisions.

[2] N. Cabibbo and G. Parisi, "Exponential hadronic spectrum and quark liberation," *Physics Letters B*, vol. 59, no. 1, pp. 67 – 69, 1975.

[3] B.-J. Schaefer and M. Wagner, "On the QCD phase structure from effective models," *Prog.Part.Nucl.Phys.*, vol. 62, p. 381, 2009.

[4] B. Back *et al.*, "The PHOBOS perspective on discoveries at RHIC," *Nuclear Physics A*, vol. 757, no. 1-2, pp. 28 – 101, 2005. First Three Years of Operation of RHIC.

[5] I. Arsene *et al.*, "Quark-gluon plasma and color glass condensate at RHIC? The perspective from the BRAHMS experiment," *Nuclear Physics A*, vol. 757, no. 1-2, pp. 1 – 27, 2005. First Three Years of Operation of RHIC.

[6] J. Adams *et al.*, "Experimental and theoretical challenges in the search for the quark-gluon plasma: The STAR collaboration's critical assessment of the evidence from RHIC collisions," *Nuclear Physics A*, vol. 757, no. 1-2, pp. 102 – 183, 2005. First Three Years of Operation of RHIC.

[7] K. Adcox *et al.*, "Formation of dense partonic matter in relativistic nucleus-nucleus collisions at RHIC: Experimental evaluation by the PHENIX collaboration," *Nuclear Physics A*, vol. 757, no. 1-2, pp. 184 – 283, 2005. First Three Years of Operation of RHIC.

[8] `http://www.star.bnl.gov/~gorbunov/main/node5.html`. Accessed 09.12.2013.

[9] J. D. Bjorken, "Highly relativistic nucleus-nucleus collisions: The central rapidity region," *Phys. Rev. D*, vol. 27, pp. 140–151, Jan 1983.

[10] J. Bartke, *Introduction to Relativistic Heavy Ion Physics*. World Scientific Publishing Company Incorporated, 2009.

[11] D. J. Gross and F. Wilczek, "Ultraviolet behavior of non-abelian gauge theories," *Phys. Rev. Lett.*, vol. 30, pp. 1343–1346, June 1973.

[12] C. Amsler *et al.*, "Review of Particle Physics," *Phys.Lett.*, vol. B667, pp. 1–1340, 2008.

[13] F. Karsch, E. Laermann, and A. Peikert, "The pressure in two flavor, (2+1)-flavor and three flavor QCD," *Phys.Lett.*, vol. B478, pp. 447–455, 2000.

[14] H. D. Politzer, "Reliable perturbative results for strong interactions?," *Phys. Rev. Lett.*, vol. 30, pp. 1346–1349, June 1973.

[15] `http://www.quantumdiaries.org/2011/11/07/flow`. Accessed 10.03.2014.

[16] K. Aamodt *et al.*, "Elliptic flow of charged particles in Pb-Pb collisions at 2.76 TeV," *Phys.Rev.Lett.*, vol. 105, p. 252302, 2010.

[17] S. A. Voloshin, A. M. Poskanzer, and R. Snellings, "Collective phenomena in non-central nuclear collisions," 2008.

[18] X.-N. Wang, "Jet quenching and azimuthal anisotropy of large p_T spectra in noncentral high-energy heavy ion collisions," *Phys.Rev.*, vol. C63, p. 054902, 2001.

[19] K. Aamodt *et al.*, "Suppression of charged particle production at large transverse momentum in central Pb-Pb collisions at 2.76 TeV," *Physics Letters B*, vol. 696, no. 1-2, pp. 30–39, 2011.

[20] M. L. Miller, K. Reygers, S. J. Sanders, and P. Steinberg, "Glauber modeling in high energy nuclear collisions," *Ann.Rev.Nucl.Part.Sci.*, vol. 57, pp. 205–243, 2007.

[21] T. Aaltonen *et al.*, "Measurement of Particle Production and Inclusive Differential Cross Sections in p-$\bar{p}$ Collisions at $\sqrt{s} = 1.96$ TeV," *Phys.Rev.*, vol. D79, p. 112005, 2009.

[22] S. Chatrchyan and the CMS collaboration, "Measurement of isolated photon production in pp and PbPb collisions at $\sqrt{s_{NN}} = 2.76$ TeV," *Physics Letters B*, vol. 710, no. 2, pp. 256 – 277, 2012.

[23] S. Chatrchyan *et al.*, "Study of W boson production in PbPb and pp collisions at $\sqrt{s_{NN}} = 2.76$ TeV," *Phys.Lett.*, vol. B715, pp. 66–87, 2012.

[24] S. Chatrchyan *et al.*, "Study of Z boson production in PbPb collisions at nucleon-nucleon centre of mass energy = 2.76 TeV," *Phys.Rev.Lett.*, vol. 106, p. 212301, 2011.

[25] `https://twiki.cern.ch/twiki/bin/view/CMSPublic/HIRaaCompilation`. Accessed: 10.03.2014.

[26] `http://www.lbl.gov/Science-Articles/Archive/sabl/2008/Feb/jets.html`. Accessed: 09.12.2013.

[27] S. Chatrchyan *et al.*, "Observation and studies of jet quenching in PbPb collisions at nucleon-nucleon center-of-mass energy = 2.76 TeV," *Phys.Rev.*, vol. C84, p. 024906, 2011.

[28] G. Aad *et al.*, "Observation of a centrality-dependent dijet asymmetry in lead-lead collisions at $\sqrt{s_{NN}} = 2.76$ TeV with the ATLAS Detector at the LHC," *Phys.Rev.Lett.*, vol. 105, p. 252303, 2010.

[29] K. Aamodt *et al.*, "Particle-yield modification in jet-like azimuthal di-hadron correlations in Pb-Pb collisions at $\sqrt{s_{NN}} = 2.76$ TeV," *Phys.Rev.Lett.*, vol. 108, p. 092301, 2012.

[30] J. Adams *et al.*, "Evidence from d+Au measurements for final-state suppression of high-p_T hadrons in Au + Au collisions at RHIC," *Phys. Rev. Lett.*, vol. 91, p. 072304, Aug 2003.

[31] M. Mangano, P. Nason, and G. Ridolfi, "Heavy-quark correlations in hadron collisions at next-to-leading order," *Nuclear Physics B*, vol. 373, p. 295, 1992.

[32] A. B. Migdal, "Bremsstrahlung and pair production in condensed media at high energies," *Phys. Rev.*, vol. 103, pp. 1811–1820, Sep 1956.

[33] R. Baier, Y. L. Dokshitzer, A. H. Mueller, S. Peigne, and D. Schiff, "Radiative energy loss and p_T broadening of high-energy partons in nuclei," *Nucl.Phys.*, vol. B484, pp. 265–282, 1997.

[34] S. Peigne and A. Smilga, "Energy losses in a hot plasma revisited," *Phys.Usp.*, vol. 52, pp. 659–685, 2009.

[35] Y. L. Dokshitzer and D. Kharzeev, "Heavy quark colorimetry of QCD matter," *Phys.Lett.*, vol. B519, pp. 199–206, 2001.

[36] M. Djordjevic, M. Gyulassy, and S. Wicks, "The charm and beauty of RHIC and LHC," *Phys.Rev.Lett.*, vol. 94, p. 112301, 2005.

[37] S. Peigne and A. Peshier, "Collisional energy loss of a fast heavy quark in a quark-gluon plasma," *Phys.Rev.*, vol. D77, p. 114017, 2008.

[38] S. Sarkar, H. Satz, and B. Sinha, *The Physics of the Quark-gluon Plasma: Introductory Lectures*. Lecture notes in physics, Springer, 2010.

[39] T. Renk, "The Phenomenology of Elastic Energy Loss," *Phys.Rev.*, vol. C76, p. 064905, 2007.

[40] T. Renk, "Using Hard Dihadron Correlations to constrain Elastic Energy Loss," *Phys.Rev.*, vol. C84, p. 067902, 2011.

[41] M. Cacciari, M. Greco, and P. Nason, "The p_T spectrum in heavy flavor hadroproduction," *JHEP*, vol. 9805, p. 007, 1998.

[42] M. Cacciari, S. Frixione, and P. Nason, "The p_T spectrum in heavy flavor photoproduction," *JHEP*, vol. 0103, p. 006, 2001.

[43] B. Kniehl, G. Kramer, I. Schienbein, and H. Spiesberger, "Reconciling open charm production at the Fermilab Tevatron with QCD," *Phys.Rev.Lett.*, vol. 96, p. 012001, 2006.

[44] B. Kniehl, G. Kramer, I. Schienbein, and H. Spiesberger, "Inclusive charmed-meson production at the CERN LHC," *Eur.Phys.J.*, vol. C72, p. 2082, 2012.

[45] B. Abelev *et al.*, "Measurement of charm production at central rapidity in proton-proton collisions at $\sqrt{s} = 7$ TeV," *JHEP*, vol. 1201, p. 128, 2012.

[46] B. Abelev *et al.*, "Measurement of electrons from semileptonic heavy-flavour hadron decays in pp collisions at $\sqrt{s} = 7$ TeV," *Phys.Rev.*, vol. D86, p. 112007, 2012.

[47] G. Aad *et al.*, "Measurements of the electron and muon inclusive cross-sections in proton-proton collisions at $\sqrt{s} = 7$ TeV with the ATLAS detector," *Phys.Lett.*, vol. B707, pp. 438–458, 2012.

[48] T. Sjostrand, S. Mrenna, and P. Z. Skands, "PYTHIA 6.4 Physics and Manual," *JHEP*, vol. 0605, p. 026, 2006.

[49] R. Brun *et al.* vol. W5013, 1994. CERN program library long write-up.

[50] B. Abelev *et al.*, "Measurement of electrons from beauty hadron decays in p-p collisions at $\sqrt{s} = 7$ TeV," *Phys.Lett.*, vol. B721, pp. 13–23, 2013.

[51] E. Norrbin and T. Sjostrand, "Production and hadronization of heavy quarks," *Eur.Phys.J.*, vol. C17, pp. 137–161, 2000.

[52] P. Z. Skands, "The Perugia Tunes," 2009. arXiv:0905.3418.

[53] S. Adler *et al.*, "Nuclear modification of electron spectra and implications for heavy quark energy loss in Au+Au collisions at $\sqrt{s}_{NN} = 200$ GeV," *Phys.Rev.Lett.*, vol. 96, p. 032301, 2006.

[54] B. Abelev *et al.*, "Erratum: Transverse momentum and centrality dependence of high-p_T non-photonic electron suppression in Au+Au collisions at $\sqrt{s_{NN}} = 200\,\mathrm{GeV}$," *Phys.Rev.Lett.*, vol. 98, p. 192301, 2007.

[55] B. Abelev *et al.*, "Suppression of high transverse momentum D mesons in central Pb-Pb collisions at $\sqrt{s_{NN}}$=2.76 TeV," *JHEP*, vol. 1209, p. 112, 2012.

[56] S. Chatrchyan *et al.*, "Suppression of non-prompt J/ψ, prompt J/ψ, and Y(1S) in PbPb collisions at $\sqrt{s_{NN}} = 2.76$ TeV," *JHEP*, vol. 1205, p. 063, 2012.

[57] R. Sharma, I. Vitev, and B.-W. Zhang, "Light-cone wave function approach to open heavy flavor dynamics in QCD matter," *Phys.Rev.*, vol. C80, p. 054902, 2009.

[58] Y. He, I. Vitev, and B.-W. Zhang, "$\mathcal{O}(\alpha_s^3)$ Analysis of Inclusive Jet and di-Jet Production in Heavy Ion Reactions at the Large Hadron Collider," *Phys.Lett.*, vol. B713, pp. 224–232, 2012.

[59] W. Horowitz and M. Gyulassy, "Quenching and Tomography from RHIC to LHC," *J.Phys.*, vol. G38, p. 124114, 2011.

[60] A. Buzzatti and M. Gyulassy, "Jet Flavor Tomography of Quark Gluon Plasmas at RHIC and LHC," *Phys.Rev.Lett.*, vol. 108, p. 022301, 2012.

[61] S. Chatrchyan *et al.*, "Evidence of b-jet quenching in PbPb collisions at $\sqrt{s_{NN}}$ = 2.76 TeV," 2013. arXiv:1312.4198.

[62] B. Abelev *et al.*, "D meson elliptic flow in non-central Pb-Pb collisions at $\sqrt{s_{NN}} = 2.76$TeV," *Phys.Rev.Lett.*, vol. 111, p. 102301, 2013.

[63] D. Caffarri, "Measurement of the D meson elliptic flow in Pb-Pb collisions at $\sqrt{s_{NN}} = 2.76$ TeV with ALICE," *Nuclear Physics A*, vol. 904-905, no. 0, pp. 643c – 646c, 2013. The Quark Matter 2012 - Proceedings of the XXIII International Conference on Ultrarelativistic Nucleus-Nucleus Collisions.

[64] W. Alberico, A. Beraudo, A. De Pace, A. Molinari, M. Monteno, *et al.*, "Heavy-flavour spectra in high energy nucleus-nucleus collisions," *Eur.Phys.J.*, vol. C71, p. 1666, 2011.

[65] J. Uphoff, O. Fochler, Z. Xu, and C. Greiner, "Open Heavy Flavor at RHIC and LHC in a Partonic Transport Model," *Acta Phys.Polon.Supp.*, vol. 5, pp. 555–560, 2012.

[66] M. He, R. J. Fries, and R. Rapp, "D_s-Meson as Quantitative Probe of Diffusion and Hadronization in Nuclear Collisions," *Phys.Rev.Lett.*, vol. 110, no. 11, p. 112301, 2013.

[67] ALICE Collaboration, "ALICE: Physics performance report, volume II," *Journal of Physics G: Nuclear and Particle Physics*, vol. 32, no. 10, p. 1295, 2006.

[68] S. Frixione and B. R. Webber, "Matching NLO QCD computations and parton shower simulations," *JHEP*, vol. 0206, p. 029, 2002.

[69] G. Corcella, I. Knowles, G. Marchesini, S. Moretti, K. Odagiri, *et al.*, "HERWIG 6: An Event generator for hadron emission reactions with interfering gluons (including supersymmetric processes)," *JHEP*, vol. 0101, p. 010, 2001.

[70] M. Nahrgang, J. Aichelin, P. B. Gossiaux, and K. Werner, "Heavy-flavor azimuthal correlations of D mesons," 2013. arXiv:1310.2218.

[71] T. Renk, "Charm energy loss and D-D correlations from a shower picture," 2013. arXiv:1310.5458.

[72] A. Mischke, "A new correlation method to identify and separate charm and bottom production processes at RHIC," *Physics Letters B*, vol. 671, pp. 361–365, Jan. 2009.

[73] X. Lin, "Charm fragmentation function and electron spectra for D and B meson semi-leptonic decays using PYTHIA calculations of p+p collisions," 2006. arXiv:0602067.

[74] M. Aggarwal and the STAR collaboration., "Measurement of the bottom quark contribution to nonphotonic electron production in $p+p$ collisions at $\sqrt{s} = 200$ GeV," *Phys. Rev. Lett.*, vol. 105, p. 202301, Nov 2010.

[75] D. Thomas, "Azimuthal angular correlations between heavy-flavour decay electrons and charged hadrons in pp collisions at $\sqrt{s} = 2.76$ TeV in ALICE," 2012. arXiv:1208.1181.

[76] Mischke, A. for the STAR Collaboration, "Heavy-flavor correlation measurements via electron azimuthal correlations with open charm mesons," *Journal of Physics G: Nuclear and Particle Physics*, vol. 35, no. 4, p. 044022, 2008.

[77] A. Mischke and the STAR Collaboration, "Heavy-flavor particle correlations in STAR via electron azimuthal correlations with D^0 mesons," *Journal of Physics G: Nuclear and Particle Physics*, vol. 35, no. 10, p. 104117, 2008.

[78] W. Borowski and the STAR collaboration, "Charm and beauty searches using electron-D^0 azimuthal correlations and microvertexing techniques in STAR experiment at RHIC," *Journal of Physics: Conference Series*, vol. 270, no. 1, p. 012030, 2011.

[79] `http://www.atlas.ch/photos/lhc.html`. Accessed: 09.12.2013.

[80] K. Aamodt *et al.*, "The ALICE experiment at the CERN LHC," *Journal of Instrumentation*, vol. 3, no. 08, p. S08002, 2008.

[81] ALICE Collaboration, "ALICE: Physics performance report, volume I," *Journal of Physics G: Nuclear and Particle Physics*, vol. 30, no. 11, p. 1517, 2004.

[82] A. Akindinov *et al.*, "Performance of the ALICE time-of-flight detector at the LHC," *The European Physical Journal Plus*, vol. 128, no. 4, pp. 1–9, 2013.

[83] M. Richter *et al.*, "Event reconstruction performance of the ALICE High Level Trigger for p+p collisions," *IEEE Trans. Nucl. Sci.*, vol. 58, no. 4, pp. 1706–1713, 2010.

[84] M. Richter, "Data compression in ALICE by on-line track reconstruction and space point analysis," *Journal of Physics: Conference Series*, vol. 396, no. 1, p. 012043, 2012.

[85] H. A. Erdal, M. Richter, A. Szostak, and A. Toia, "Monitoring the data quality of the real-time event reconstruction in the ALICE High Level Trigger," *Journal of Physics: Conference Series*, vol. 396, no. 1, p. 012019, 2012.

[86] B. von Haller *et al.*, "The ALICE data quality monitoring," *Journal of Physics: Conference Series*, vol. 219, no. 2, p. 022023, 2010.

[87] B. von Haller *et al.*, "The ALICE data quality monitoring system," *Journal of Physics: Conference Series*, vol. 331, no. 2, p. 022030, 2011.

[88] B. Abelev *et al.*, "Measurement of inelastic, single- and double-diffraction cross sections in proton–proton collisions at the LHC with ALICE," *Eur.Phys.J.*, vol. C73, p. 2456, 2013.

[89] A. Dainese, "Charm production and in-medium QCD energy loss in nucleus nucleus collisions with ALICE: A Performance study," 2003. arXiv:nucl-ex/0311004.

[90] D. Thomas, E. Pereira De Oliveira Filho, *et al.*, "Azimuthal angular correlations between heavy-flavour decay electrons and charged hadrons in proton-proton collisions at $\sqrt{s} = 2.76$ TeV using the ALICE detector," 2012. ALICE Internal Analysis Note.

[91] L. Musa and K. Safarik, "Letter of Intent for the Upgrade of the ALICE Experiment," Tech. Rep. CERN-LHCC-2012-012. LHCC-I-022, CERN, Geneva, Aug 2012.

[92] X.-N. Wang and M. Gyulassy, "HIJING: A Monte Carlo model for multiple jet production in p p, p A and A A collisions," *Phys.Rev.*, vol. D44, pp. 3501–3516, 1991.